SURFACE ENGINEERING OF TRANSITION METAL DICHALCOGENIDES FOR TWO-DIMENSIONAL ELECTRONIC DEVICE APPLICATIONS

by

Angelica Azcatl Zacatzi

APPROVED BY SUPERVISORY COMMITTEE:

_____

Dr. Robert M. Wallace, Chair

_____

Dr. Orlando H. Auciello

_____

Dr. Kyeongjae Cho

_____

Dr. Manuel A. Quevedo-Lopez

To my beautiful, brave, and inspiring mother,

Juanita Zacatzi Cuatzo

SURFACE ENGINEERING OF TRANSITION METAL DICHALCOGENIDES FOR TWO-DIMENSIONAL ELECTRONIC DEVICE APPLICATIONS

by

ANGELICA AZCATL ZACATZI, BS

DISSERTATION

Presented to the Faculty of

The University of Texas at Dallas

in Partial Fulfillment

of the Requirements

for the Degree of

DOCTOR OF PHILOSOPHY IN

MATERIALS SCIENCE AND ENGINEERING

THE UNIVERSITY OF TEXAS AT DALLAS

December 2016

ACKNOWLEDGMENTS

First of all, I would like to thank Professor Robert M. Wallace for his guidance during the doctorate program. He is a great scientist, and it has been a pleasure and honor to be part of his research group. He inspires and encourages students to give their best to achieve exceptional goals, and I will always be grateful for the knowledgeable and in-depth inputs that he provided to my work. My appreciation to him will surely continue over the years. I would also like to thank the members of my committee Professor Manuel A. Quevedo-Lopez, Professor Kyeongjae Cho and Professor Orlando Auciello for their time and help in the process of my Ph.D. defense.

My acknowledgment to Dr. Stephen McDonnell, currently an assistant professor at the University of Virginia, who introduced me for the first time to X-ray photoelectron spectroscopy and to vacuum systems. He is a passionate and knowledgeable scientist, and working with him was really an every-day learning experience. My gratitude goes also to Dr. Luigi Colombo, whose advice and constant feedback gave me a special training and provided me with a broad view of the impact of my research in the academy as well as in the industry. I would also like to thank Professor Kyeongjae Cho, Professor Moon J. Kim, Professor Jiyoung Kim, Professor Hinkle, and Professor Chadwin Young and to the students in their respective groups; the work presented in this dissertation could not have been accomplished without your valuable contribution.

My sincere gratitude goes also to Professor Ali Javey from UC Berkeley, Professor Alan Seabaugh from the University of Notre Dame, Professor Joshua Robinson from Pennsylvania

State University, and Professor Joerg Appenzeller from Purdue University, faculty members that I had the great opportunity to collaborate with through the SRC-sponsored LEAST project.

I would like to thank the group members in Professor Wallace's group, Dr. Xiaoye Qin, Mrs. Hui Zhu, Mr. Christopher Smyth, and Dr. Rafik Addou, to the former members Dr. Hong Dong, Mr. David Hinojos, and Dr. Barry Brennan, and to our colleagues Dr. Antonio Lucero and Dr. Lanxia Cheng. They all are brilliant and kind people that were willing to help and support me anytime. My acknowledgment to our technical staff, Mr. Tommy Bennett, Mr. Billy Raulston (retired), and Mr. Dave Stimson for their hard work and patience in solving issues at the lab; your help is invaluable for our research. Also, I want to thank my friends Dr. Maribel Maldonado-Garcia, Dr. Xavier Lepro-Chavez, Dr. Alex B. Cook, Dr. Jonathan Yuen, Mr. Gautam Gaddemane, Ms. Isabel Pintor Monroy, Ms. Martha I. Serna, Mr. Yasiel Cabrera, Dr. Lindsey Smith, Dr. Srikar Jandhaya, and Mr. Juan Pablo Oviedo for the great memories and for being my family in USA.

Last but not least, I want to thank my beloved parents Juanita Zacatzi Cuatzo and Marino Azcatl, and to my amazing siblings and best friends Miguel, Raul, Isabel, and Antonio for their love and support throughout this adventure. You all are my inspiration.

October 2016

SURFACE ENGINEERING OF TRANSITION METAL DICHALCOGENIDES FOR TWO-DIMENSIONAL ELECTRONIC DEVICE APPLICATIONS

Publication No. _____

Angelica Azcatl Zacatzi, PhD
The University of Texas at Dallas, 2016

Supervising Professor: Robert M. Wallace

Two-dimensional transition metal dichalcogenides (TMDs) are considered potential channel materials for emerging electronic devices in the roadmap beyond Si-CMOS technology. Layered TMDs offer intrinsically an ultrathin body without compromising the semiconducting properties. For the implementation of TMDs in electronic device structures, the understanding of their surface properties is essential. This work combines a variety of materials characterization techniques such as in-situ X-ray photoelectron spectroscopy, atomic force microscopy, transmission electron microscopy, and Raman spectroscopy to investigate the chemistry and structure of TMDs upon different surface treatments. In addition, first-principle calculations are presented to give insights on the mechanism involved in the surface modification of TMD. The impact of the TMDs surface modification on processes for gate-oxide integration by atomic layer deposition and covalent doping are investigated here. This work provides a comprehensive understanding of the surface chemistry of TMDs for two-dimensional electronic device applications.

TABLE OF CONTENTS

LIST OF FIGURES

LIST OF TABLES

CHAPTER 1

INTRODUCTION

1.1 Transition Metal Dichalcogenides: An Overview

The study of two-dimensional (2D) materials has been sparked ever since the report on the isolation of graphene, a material that consists of only a single of carbon atoms, in 2004 by the Nobel laureate, K. S. Novoselov.[1] Among the exceptional electrical properties that graphene exhibits, the high carrier mobility became a representative and unique feature of this material, with record values up to 100,000 $cm^2/V \cdot s$ at room temperature.[2] However, the intrinsic semimetallic nature along with the characteristic zero-bandgap has limited the application of graphene in logic devices. In the search for alternative two-dimensional materials with semiconducting properties, the attention towards layered transition metal dichalcogenides (TMDs) has increased in recent years. Furthermore, the high-performance of field-effect transistors based on single-layer MoS_2 gave an initial demonstration of the potential that these materials have in the area of 2D nanoelectronics.[3] Semiconducting TMDs, such as MoS_2, are materials that offer a sub-nanometer thickness and tunable band gap values that are dictated by their composition and layer thickness.[4] Such versatility encountered in a 2D semiconducting TMD is ideal for their application in emerging electronic devices beyond Si-CMOS technology.

TMDs are composed by transition metal (M) and chalcogen (X) atoms in an MX_2 stoichiometry. Figure 1.1 shows the transition metal and chalcogen elements which combined exhibit a layered

structure. In specific cases, TMDs based on Co, Rh, Ir, Ni, Pd, Pt can also form a layered structure.[5]

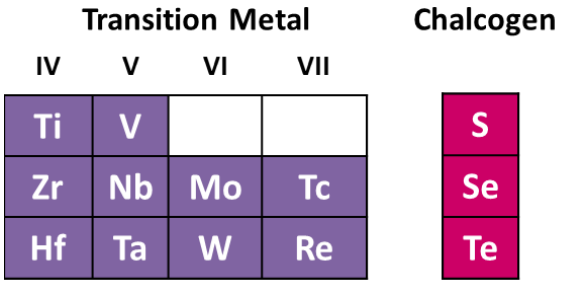

Figure 1.1. Transition metals and chalcogen elements that exhibit a layered structure in a MX_2 stoichiometry.

A monolayer of a TMD is constituted by a three atoms-stack (X-M-X) bonded covalently, whereas, in multilayer TMDs, the monolayers are bonded to each other by van der Waals forces. Generally, the thickness of a single layer is ~6-7 Å, and the length for M-X bonds ranges between 3.15 Å and 4.03 Å, depending on the size of the individual ions.[6] The metal atom in a layered TMD is bonded to six chalcogen atoms in either trigonal prismatic or octahedral coordination, as shown in Figure 1.2. Depending on the stacking sequence of the layers, TMDs can exhibit different polytypes, referred as 1T (one layer in tetragonal symmetry in octahedral coordination), 2H (two layers in hexagonal symmetry in trigonal prismatic coordination), and 3R (rhombohedral symmetry, three layers per repeat unit, trigonal prismatic coordination).

For example, geological MoS_2 exhibits only a 2H phase, whereas TiS_2 is commonly found in the 1T phase. Interestingly, the electronic properties of TMDs can be associated with the specific polytypes. For example, 2H-MoS_2 and 2H-WS_2 exhibit a semiconducting character, whereas 1T-MoS_2 and 1T WS_2 are metallic.[5] The composition in TMDs will also determine their insulating, semiconducting or metallic properties.[7]

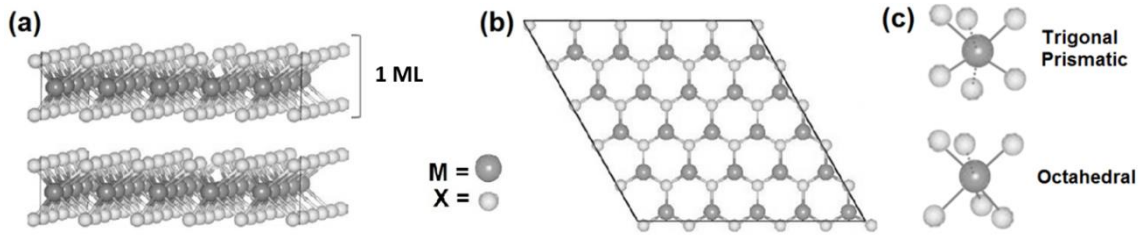

Figure 1.2. (a) Schematic of the TMD layered structure. (b) Top view of characteristic 2-H hexagonal lattice. (c) Representative structures of the transition metal coordination in a TMD: trigonal prismatic (top) and octahedral (bottom). Adapted with permission from ref [8] Copyright (2015) AIP Publishing LLC.

TMDs of the form M=Mo, W and X=S, Se, Te are semiconductor materials with thickness dependent bandgap energies in the range of ~1.0 – 2.0 eV.[9] Furthermore, in the monolayer form, semiconducting TMDs are characterized by a direct bandgap, whereas in the bulk form, an indirect bandgap is exhibited.[7] Table 1.1 lists the experimental monolayer and bulk band gap value for selected TMDs.

Table 1.1. Experimental bandgap values for common layered transition metal dichalcogenides. References: a:[10], b:[11], c:[12], d:[9], e:[13], f:[14], g:[15], h;[16].

	Bandgap Energy (eV)	
MX_2	1 ML	Bulk
MoS_2	1.89[a]	1.23[b]
$MoSe_2$	1.55[c]	1.09[d]
$MoTe_2$	1.15[e]	1.00[f]
WS_2	2.05[g]	1.35[d]
WSe_2	1.49[h]	1.20[d]

Bulk layered TMDs can be found in nature from geological sources. However, for electronic device applications, current efforts have been carried out for the growth and synthesis of large

area films. TMDs flakes of various thicknesses can be isolated by mechanical exfoliation of the bulk layered materials, e.g., by the Scotch® tape method, in analogy to the process employed to obtain exfoliated graphene.[1] Commonly, the flakes are exfoliated onto a SiO_2/Si substrate for its identification by optical microscopy, where the layer thickness can be identified from their characteristic color contrast. By this method, TMDs flakes with an area of only a few tens of micrometers can be obtained, and therefore the mechanical exfoliation method is not scalable to large areas. Alternatively, the synthesis of mono and few-layer TMDs through chemical and physical have been developing, with the aim to obtain large area films. The approaches for the synthesis of TMDs include: (a) liquid exfoliation of the bulk material,[17] (b) chemical vapor deposition (CVD) using a chalcogen (HS_2) and transition metal precursor gases ($MoCl_5$, $M(CO)_6$, $WOCl_4$),[6,18] (c) molecular beam epitaxy by e-beam evaporation of the elemental sources (M: W, Hf, Nb, X:Te, Se),[19,20] (d) sulfurization of MoO_3 by vapor transport methods,[21] (e) thermal decomposition of $(NH_4)_2MoS_4$,[22] (f) pulse layer deposition from MX_2 targets,[23] and more recently by (g) atomic layer deposition using similar precursors as those employed in CVD processes.[24] Significant progress has been attained in the synthesis and understanding of the growth process, especially for MoS_2. However, the synthesis of high-quality and large area transition metal dichalcogenides other than MoS_2 is still under development. In addition, reduction of defects and impurities is another aspect to be addressed in the area of synthesis of two-dimensional TMDs.

1.2 Two-Dimensional TMDs for Tunnel Field-Effect Transistor Applications

Scaling down the channel dimensions of metal-oxide semiconductor field-effect transistors (MOSFET) employed in the CMOS technology has been motivated by the resulting increase in

switching speed and integration density. Yet, the power consumption has not been effectively decreased along with the reduction in the transistor dimensions.[25] The figure-of-merit that serves to quantify the effect of voltage on the switching performance in MOS transistor is the subthreshold swing (S), which determines the amount of voltage swing necessary to switch the transistor from the OFF to the ON state. The expression for S can be obtained from the equation that describes the drain current of a MOSFET operated at subthreshold gate voltages:[26]

$$I_D = I_{D1} exp\left(\frac{q(V_{GS}-V_T}{nkT}\right)\left(1 - exp\left(\frac{qV_{DS}}{kT}\right)\right) \quad (1.2)$$

Where I_{D1} depends on the doping concentration, device dimensions (W,L) and temperature. In equation (1.2) n can be expressed as $n=(1 + C_d/C_{ox})$, where C_d and C_{ox} are the depletion and the oxide capacitances, respectively. Therefore, in a usual subthreshold plot of log (I_D) versus V_{GS} for $V_{DS} >> kT/q$, the slope of the curve will be given by $q/ln(10)nKT$. The inverse of this slope represents the gate voltage required to change the drain current by an order of magnitude (one decade), the subthreshold swing, S:

$$S = \left(1 + \frac{C_d}{C_{ox}}\right)\frac{kT}{q}\ln(10) \quad (1.3)$$

Therefore, a steep-slope in the I_D-V_{GS} curve is desirable to access the low power region. However, in conventional MOSFETs, the minimum S is dictated by the operation temperature (≈ 60 mV/dec at 300 K). Alternatively, tunneling FETs have been considered as steep-slope low power devices, since they rely on band-to-band tunneling charge injection into the channel, instead of thermal injection.[27,28] By means of the temperature independent tunneling mechanism, the fundamental limit of the subthreshold swing set by the thermal voltage could be reduced, which in turn could decrease the operational voltages. This particular characteristic of the TFET

devices results ideal for low-power applications.[29] A representative TFET structure is presented in Figure 1.3a, where n^+ and p^+ are the heavily doped regions of the channel representing the source and drain terminals, respectively, whereas i represents the intrinsically doped active region of the channel.[30]

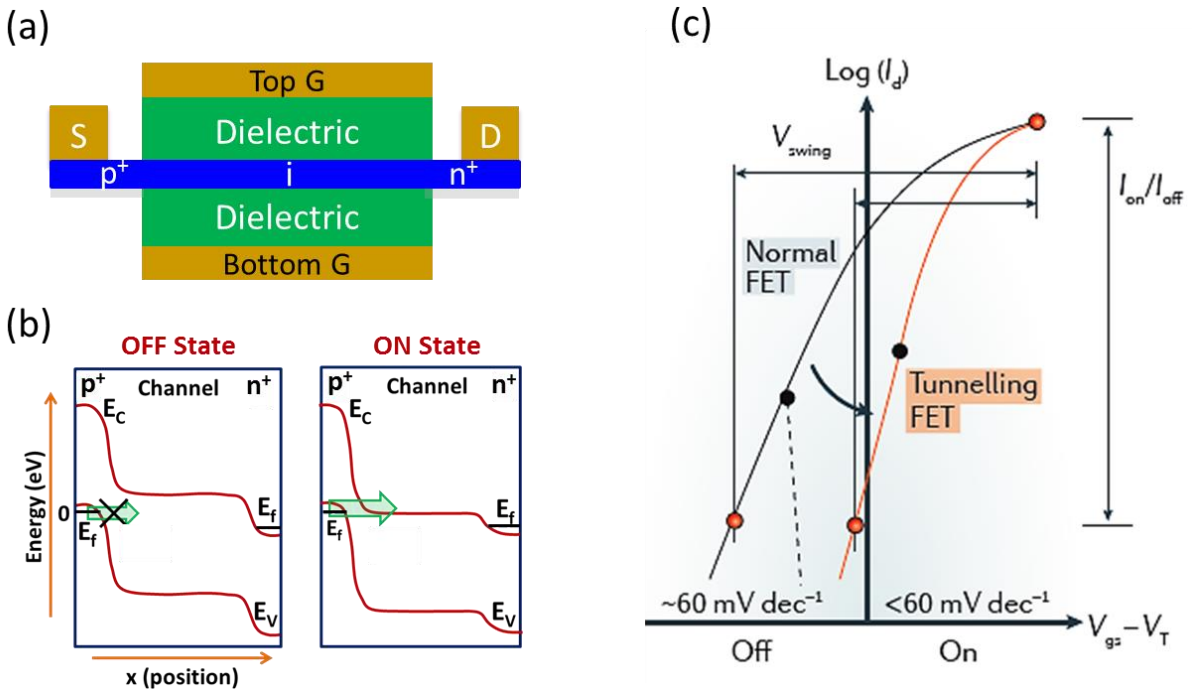

Figure 1.3. (a) Device structure of a 2D TMD-based tunneling field-effect transistor (TFET) and (b) the corresponding energy band diagram for the OFF and ON states. Adapted from [29]. Copyright (2010) IEEE. (c) I_D-V_{GS} characteristics of a conventional FET and a tunneling FET Reprinted from [31]. Copyright (2016), with permission from Macmillan Publishers Ltd: [Nature Reviews].

In a TFET, the gate voltage V_G can electrostatically control the energy band alignment of the n-i-p structure. In the off state, no empty states are available in the channel for tunneling from the source. By applying a negative voltage V_G, the valence band energy of the channel is lifted above the conduction band energy of the source, and a conductive channel is formed where the carriers can tunnel into the empty states in the channel, reaching an on state.[29] Therefore, the

tunneling probability and the thickness of the tunneling barrier at the source-channel junction can be modulated by V_G. In contrast, in a conventional FET, the ON state is attained by thermionic injection of the carrier from the source to the drain regions for a given applied V_G. The difference in the operational principles between a conventional FET and a TFET is reflected in the I-V characteristics. Figure 1.3c shows that the steeper subthreshold slope of the TFET results in a higher I_{ON} current at a smaller gate voltage. This feature is expected to enable scaling of the voltage supply V_{DD} to lower values while maintaining a substantial ON/OFF ratio.

The ON-current (I_{ON}) in a TFET depends on the interband tunneling transmission probability T_{WKB} , which can be approximated as:[27]

$$I_{ON} \propto T_{WKB} \approx \exp\left(-\frac{4\lambda\sqrt{2m_r^*}\sqrt{E_g^3}}{3q\hbar(E_g+\Delta\varphi)}\right) \tag{1.2}$$

where m_r^* is the reduced effective mass, E_g is the band gap, $\Delta\varphi$ is the energy difference between the conduction band in the source to the valence band in the channel, and λ is the screening tunneling length, which has a dependence on the device geometry, as follows:

$$\lambda = \sqrt{t_{ox} t_{body} \frac{\epsilon_{body}}{\epsilon_{ox}}} \tag{1.3}$$

According to equations (1.2) and (1.3), to maximize the performance in a tunnel FET and to achieve a high I_{ON}, the desirable features of the channel material are a light-effective mass of the charge carriers, small bandgap, and a thin body thickness.[28] Potential channel materials for TFET applications include Si, III-V and carbon nanotubes. According to the literature, a reduction in λ has been demonstrated by placing a thin high-κ dielectric gate oxide (e.g., below 2 nanometers) on these channel materials.[29] However, the implementation of conventional 3D semiconductors,

such as Si and III-V semiconductors in TFET structures have encountered issues related to surface roughness scattering effects developed when the body thickness is scaled down, resulting in the reduction of the carrier mobility in TFETs. In addition, the rapid increase of the bandgap due to the effect of quantization with the decrease in thickness for some 3D materials can also have an undesirable impact on the I_{ON} current according to equation (1.2).[30]

Alternatively, layered TMDs materials have been proposed as potential channel materials for TFETs applications. In general, the thickness of semiconducting TMD can be scaled down to sub-nanometer dimensions without compromising the bandgap energy. The efforts in the implementation of layered TMDs in TFET applications has also been motivated by the concept that on the basal plane of the two-dimensional material all the bonds are satisfied, suggesting an ideal dangling bond-free surface. Therefore, it is expected that electrical response of TMD-based TFETs would not be affected by defect states associated with dangling bonds; however, this ideal condition is generally not attained.[32] Additionally, it is also predicted that by having a planar 2D structure in the channel, a high electric field can be obtained at the tunnel junction, increasing the tunneling current. Furthermore, TDMs offer a variety of bandgap and band alignments dictated by the different composition, which allows the engineering of various device configurations. In fact, it has been proposed that having a heterostructure for the channel composed of two dissimilar 2D crystals can significantly enhance the I_{ON} due to the band alignment tuning by an external perpendicular electric field.[31] In this case, the desired band alignment for the heterojunction would be of type-II (staggered, one of the bands of the narrow bandgap material lies outside the bandgap of that of the wider bandgap) or type-III (broken gap,

where the conduction band edge of one material lies below the upper valence band edge of the partner).[33]

Experimentally, the demonstration of TMD-based TFETs has been limited due to various factors, from the intrinsic electrical behavior of the channel material to fabrication process. A promising work by Sarkar *et al*.[34] shows a subthreshold swing of ~32 mV/dec and V_G of < 0.1 V for a MoS_2-based TFET structure, with a highly doped germanium as source. The prospect of reaching subthreshold swing values lower than ~60mV /dec is the motivation of the current effort for the development of 2D TMD based-TFETs.

1.3 Motivation

Currently, the implementation of a 2D TMDs as channel material in TFET structures imposes a set of requirements that includes:[31,33,35]

- The development of processes for the growth or synthesis of high-quality and large-area mono and few-layer TMDs films.
- The reduction of defects and impurities in TMD material.
- The engineering of metal contacts for TMD for the reduction of the Schottky barrier at the metal/TMD interface
- The integration of gate oxides on the TMD surface
- A controllable doping type and doping profile of the TMD material

Therefore, it is evident that in order to address these challenges, a clear understanding of the chemical and structural properties of the TMD materials is needed. Also, given the fact that the channel material is two-dimensional, the integrity of the surface will be an important element to

take into consideration in the design and development of the materials synthesis and processing. In specific, the scope of this work is centered on the integration of oxide films on the TMD surface and the development of a doping strategy for the TMD material, which are key areas for the development of the emerging TFET technology. Due to its availability, the studies presented here were performed mainly on MoS_2, and in some cases, on transition metal diselenides ($MoSe_2$, WSe_2).

1.3.1 Integration of Gate Oxides on the TMD Surface

The efficient electrostatic control of the gate over energy bands of the channel in the TFET structure, a high-quality and thin gate oxide is desirable. The starting point in the study of gate oxide films was the understanding of the initial state and reactivity of the TMD surfaces. In conventional bulk semiconductors such as Si, or III-V materials, dangling bonds are present at the surface, which are characterized by the presence of unpaired electrons or holes.[36] Dangling bonds tend to pair up followed by a reconstructing of the surface structure to reduce the surface energy. The reported surface energy for a silicon (111) surface is in the order of 1240 mJ/m^2.[37] Such high surface energy favors the formation of a thin oxide layer upon air exposure on the clean Si surface; this thin oxide serves as a passivation layer and minimizes the number of dangling bonds at the Si surface.[38] In contrast, the bonds at the basal planes of two-dimensional materials are satisfied, and ideally, a dangling bond-free surface is expected.[39] However, it is also known that the surface of TMDs presents various types of defects that are randomly distributed in local areas, such as atomic vacancies, and metallic-like defects.[32] For MoS_2, for example, the density of metallic defects (likely clusters of sulfur atoms) represent ~ 0.1-5% of the surface.[35] Interestingly, TMD surfaces are characterized by a low surface energy (e.g., ~54.5 mJ/m^2 for

MoS_2)[40], which is indicative of a limited surface reactivity. Furthermore, the low contact angle of these surfaces reflects the hydrophobicity of TMDs.[41] For such reasons, layered MoS_2, and other TMDs such as WSe_2, do not form an oxide passivation layer at the surface.

This situation is critical for the integration of dielectric film, since atomic layer deposition, a preferred technique for oxide deposition, requires reactive sites at the surface for conformal and uniform oxide growth. As a result of the limited reactivity of the TMD surfaces, it has been shown that the deposition of dielectrics follows an island-type growth, resulting in non-uniform films.[11,42,43] Figure 1.4 shows the films obtained after the deposition of HfO_2 on MoS_2 by ALD, where clearly, the film morphology reflects the islanding mechanisms during the initial stages of the ALD process on the relatively inert MoS_2 surface.

Yet, the generation of a reactive surface in two-dimensional materials results challenging as these materials are only ten of a nanometer in thickness, and it is desirable that any process to active the surface should preserve the structural and electrical of the material. Common semiconductor processes such as ion bombardment[44] or plasma treatments[45,46] can lead to severe modification or damage to the two-dimensional structure. On the other hand, mild wet treatments or non-covalent functionalization can also cause minimal effect on the surface reactivity.[11] In this work, different approaches for the surface functionalization of MoS_2 and transition metal diselenides were followed in order to achieve highly uniform and ultra-thin high-κ dielectrics deposited by atomic layer deposition (ALD). The composition, structural changes and reactions at the high-κ/TMD interface will be investigated. This study will also take into consideration the electrical properties of the high-κ dielectrics on the TMD surface.

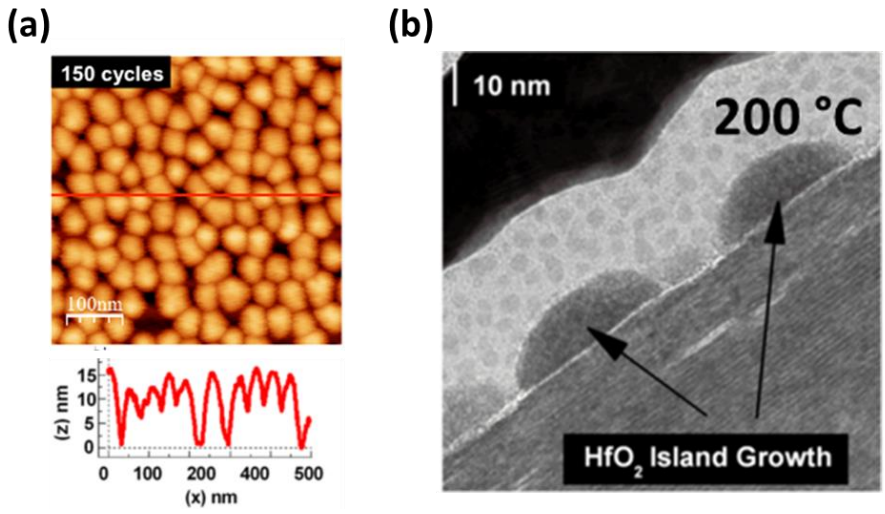

Figure 1.4. HfO_2 deposited on bare MoS_2 by ALD using 150 ALD cycles at 200 °C (a) surface topography and cross-sectional TEM image. Reprinted with permission from Ref [11]. Copyright (2013) American Chemical Society.

1.3.2 Covalent Doping of TMDs

As described previously, in a TFET structure, the source and drain regions of the channel material should be heavily doped for an adequate alignment of the bands. Theoretical studies have suggested that a doping concentration on the order of ~ 1×10^{20} cm^{-3} for monolayer TMDs is acceptable for the operation of the tunneling device.[47] Currently, the design and study of doping techniques for 2D TMDs is still under development. Different to conventional 3D semiconductors, ion implantation results impractical for 2D materials as high-energy particles can readily perturb or damage the 2D lattice. In this regard, the study of molecular doping using species such as NO_2,[48] polyethylenimine,[49] and benzyl viologen[50] represents an important step into the understanding of doping TMDs through charge transfer. However, due to the non-covalent bonding nature of the dopant molecules, this strategy has been limited by their volatility over time, making the control over doping concentration a challenge. Electrostatic doping is

another approach that has been employed to dope TMDs through the use of a polymer electrolyte or ionic liquid gating,[51,52,53] relying on the applied voltage to modulate the carrier density. In addition to these strategies, covalent doping of TMDs, where single atom dopants are introduced in the TMD lattice through metal or chalcogen substitution, is a potential route to achieve stable and controllable doping. An example of covalent p-type doping of MoS_2 has been demonstrated through Mo substitution by Nb during the growth process.[54,55] Furthermore, substitutional doping can induce new functionalities to TMD materials such as optical band gap tuning[56] or the prospect of magnetic behavior.[57]

In this work, a remote plasma treatment is proposed as an approach for covalent doping of MoS_2. The use of a mild plasma-based surface treatment is studied to investigate the chemical changes and the structural implications associated to due to the plasma exposure in MoS_2. The electrical characterization of the doped material is presented. This study aims to understand substitutional doping in TMDs for future implementation in tunneling FET.

1.4 Dissertation Outline

In this dissertation, different approaches for the surface engineering of TMDs for high-κ deposition and for covalent doping are presented. The study of the processes for the TMD surface engineering was carried out by in-situ surface characterization. In parallel, first principles calculations were employed to provide an understanding of the mechanisms involved in the surface modification attained experimentally. Complementary ex-situ materials characterization techniques were also performed to correlate with the in-situ surface analysis.

The first section of this dissertation described the experimental techniques employed for the in-situ and ex-situ surface and interface characterization.

In Chapter 3, the effect of the UV-O_3 treatment on the MoS_2 surface chemistry and structure is investigated. Evidence of oxygen functionalization of MoS_2 upon UV-O_3 treatment is presented. Then, the atomic layer deposition process for the deposition of high-κ dielectrics was studied on the functionalized MoS_2 surface by in-situ XPS. Finally, the chemical analysis is correlated with the electrical properties of the high-κ dielectric/TMD interface.

Chapter 4 presents the study of the UV-O_3 exposure extended to the transition metal diselenides: $MoSe_2$, and WSe_2. The surface chemistry observed on such surface is correlated with first principle calculation. Finally, the surface reactions during the HfO_2 deposition on the UV-O_3 treated surfaces are investigated by in-situ XPS, and the resulting morphology and structure of the HfO_2/transition metal diselenides are presented.

In Chapter 5, the study of ozone-based ALD as an alternative approach for dielectric deposition on WSe_2 is studied. First, the interaction of ozone with WSe_2 is analyzed by in-situ XPS. Then, the deposition temperature dependence of the high-κ dielectric/WSe_2 interface chemistry is studied and correlated with the ALD-dielectric nucleation. Finally, the band alignment of the deposited dielectrics on WSe_2 was determined for tunneling FET device analysis applications.

In Chapter 6 a process for covalent nitrogen doping of MoS_2 by a remote N_2 plasma surface treatment is proposed. The control in the nitrogen concentration with N_2 plasma exposure time is demonstrated. In addition, evidence of the p-type character of the nitrogen dopant in MoS_2 is provided. The implications in the MoS_2 structure upon nitrogen doping are also presented.

Finally, the concluding remarks and future work related to the processes for surface engineering of TMD for emerging 2D electronic device applications are discussed in Chapter 7.

CHAPTER 2

EXPERIMENTAL DETAILS

2.1 In-situ Surface and Interface Characterization

In this work, several characterization techniques were employed to investigate the chemical and structural properties of two-dimensional materials upon different surface treatments. The studies presented here were performed in an ultrahigh vacuum (UHV) cluster tool, which consists of a set of chambers for surface analysis, surface treatment, and thin film deposition all connected by a transfer tube that is maintained at a base pressure in the order of $\sim 10^{-10}$ mbar. Figure 2.1 shows the schematic of the UHV cluster tool. The following characterization techniques can be performed in the analysis chamber: X-ray photoelectron spectroscopy (XPS), ultraviolet photoelectron spectroscopy (UPS), low energy ion scattering (LEIS) and low energy electron diffraction (LEED). The capabilities for thin film deposition include metal deposition by physical vapor deposition (PVD chamber), molecular beam epitaxy (MBE chamber), RF-sputtering deposition (Sputtering chamber), and atomic layer deposition (ALD chamber). Additionally, thermal annealing under various gas environments (O_2, N_2, Ar, 5% H_2/N_2) can be carried out in the annealing chamber; UHV vacuum annealing by heat transfer from Pt and graphite heaters can be also performed in the Sputtering and PVD chambers. During a surface analysis experiment, an ultra-high vacuum environment is desirable in order to retard the adsorption of spurious/residual gas molecules contaminants. For example, a monolayer of a contaminant gas (e.g., $\sim 10^{15}$ atoms/cm^2) can be formed within 1 second under a working

pressure of ~ 10^{-6} mbar, assuming a sticking coefficient of 1 at 300 K. In contrast, the time to form one monolayer on the sample surfaces can be extended to > 10^{4} seconds in ultra-high vacuum, having a pressure in the order of ~10^{-10} mbar. Therefore, a UHV environment maximizes the time to analyze a surface by retarding the adsorption of contaminants during the experiment.

Furthermore, for the proper operation of photoelectron spectroscopy, UHV conditions are required to reduce the probability of low-energy electrons to be scattered by background gas molecules, maximizing the electron mean free path.

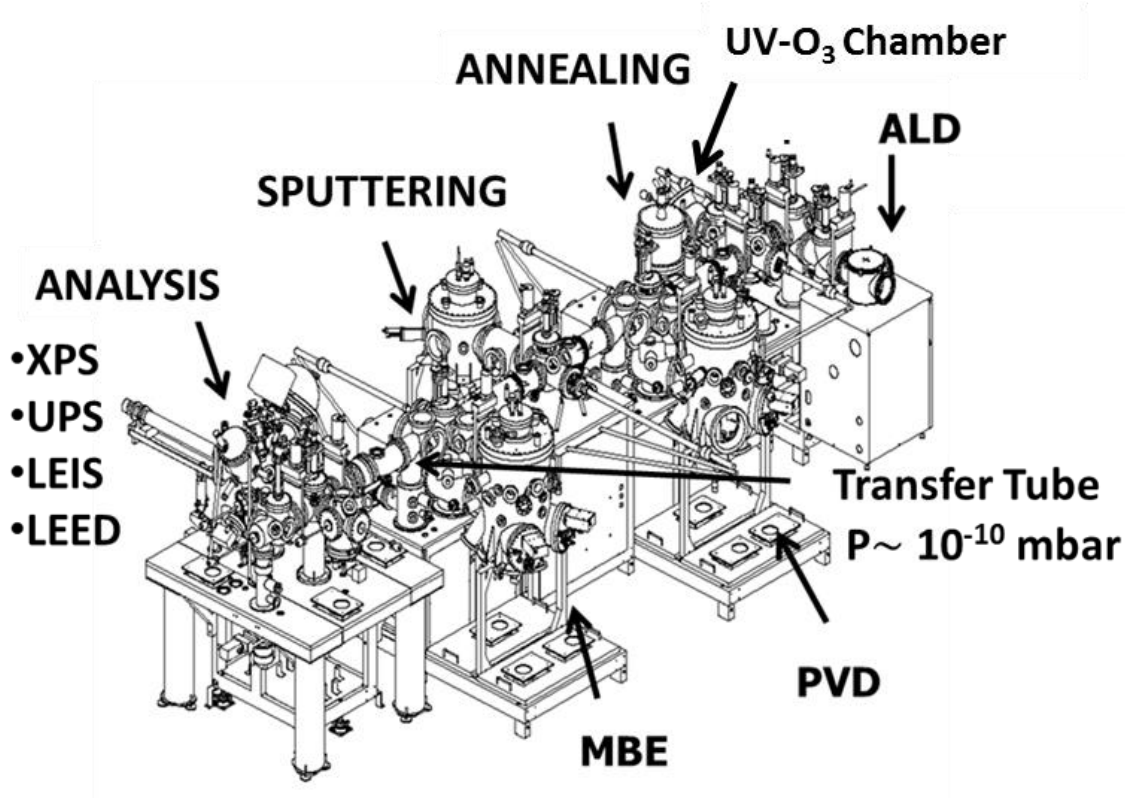

Figure 2.1. UHV cluster tool for *in-situ* surface characterization, surface treatment and thin-film deposition.

2.1.1 X-Ray Photoelectron Spectroscopy

XPS is a surface sensitive technique for elemental analysis of metals, semiconductors, dielectrics and even polymers. The sampling depth of this technique is ~10 nm from the outermost surface of a material. This technique can be employed for the identification and quantification of elements (except H and He), identification of chemical states (oxidation states, covalent bonding), determination of elemental surface composition, non-destructive and destructive elemental depth profiles, thin film thickness measurements, for the measurement of the band alignment in a heterostructure, and any other application related to the elemental analysis.

The fundamental principle of X-ray photoelectron spectroscopy is based on the photoelectric effect, where emission of an electron from a determined core level in the atom is caused by the excitation of incident X-ray photons of energy hν.

The energy transfer in this process is described as:[58]

$$E_{BE} = h\nu - E_K - \Phi_{sp} \tag{2.1}$$

Where, E_{BE} is the binding energy of the photoelectron being ejected, referenced to the Fermi level E_F, $h\nu$ is the energy of the incident X-ray photons, E_K is the kinetic energy of the photoelectron, and Φ_{sp} is the work function of the spectrometer. Here, for the measurement of the binding energy, a conducting sample and the spectrometer are placed in electrical contact so that the Fermi level is the common reference energy. The emission process is depicted in Figure 2.2, and the energy level diagram of the configuration employed for the measurement of the E_{BE} is presented in Figure 2.3. The peaks obtained from the XPS spectra correspond to the core levels of the atom from which the photoelectrons are ejected.

The convention for the nomenclature to identify the XPS peak from a determined core level is given by the orbital (l=0,1,2,3.. or *s, p, d, f*) quantum numbers and the total momentum of the photoelectrons .($J = l \pm s$).[44]

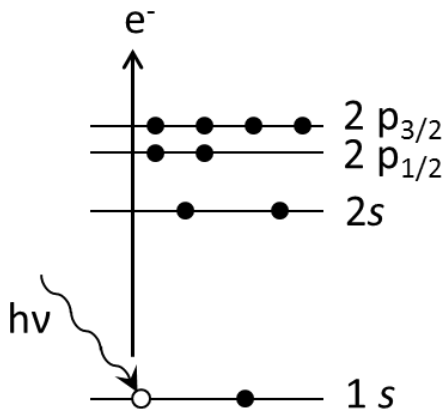

Figure 2.2. Schematic of the electron emission process upon the excitation by a photon of energy hν.

During photoelectron emission, the empty electron position left by the primarily ejected photoelectron can be filled by an electron from a higher energy level. The energy liberated due to this transition can be transferred to a third electron, denominated as an Auger electron, which is also ejected out of the surface in this process. Therefore, photoelectrons and Auger electrons will be simultaneously detected by an XPS spectrometer.

The binding energy of a photoelectron depends on the type of atom and its chemical environment (e.g., nuclear charge, electron distribution). Therefore, the binding energy in an XPS spectrum can be associated with the chemical state of an element in the material studied, allowing the identification of oxidation states, covalent bonds, shake-up transitions, organic functional groups, valence band fingerprints, among other applications.

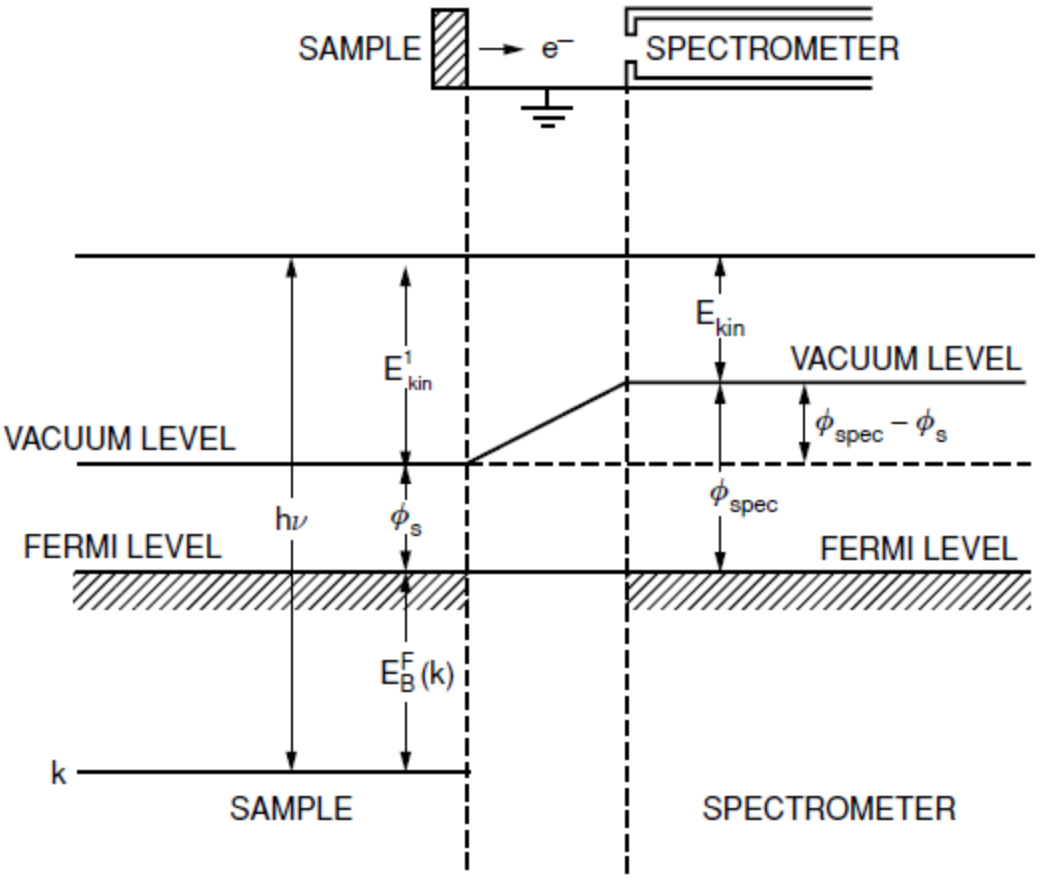

Figure 2.3. Schematic of energy levels for XPS binding energy measurements for a conductive sample, where E_b^F is the binding energy, Φ_s and Φ_{spec} are the spectrometer and the sample workfunction values, respectively, E_{kin}^1 is the photoelectron kinetic energy and E_{kin} is the measured kinetic energy. Reproduced from ref. [59] with permission of Springer-Verlag New York Inc.

In addition, XPS allows quantitative analysis since the photoelectron intensity of an element *i* is related to its elemental concentration n_i as:[60]

$$I_i = KTL\sigma_i \int n_i(z) e^{\frac{-z}{\lambda_{i,M} cos\theta}} dz \qquad (2.2)$$

Here, *K* is a constant that contains fixed operational parameters related to the spectrometer such as incident X-ray flux, efficiency of the detector, *T* is the analyzer transmission function which is

dependent on the kinetic energy, L is the angular asymmetry parameter for the emission from a determined core level, σ_i is the photoionization cross-section for a determined core level, λ is the inelastic mean free path length in a matrix M containing i, which depends on the kinetic energy of the photoelectrons, and θ is the emission angle (with respect sample normal). Assuming a constant concentration profile over the depth of analysis, equation (2.2) can be expressed as:

$$I_i = KTL\sigma_i n_i \lambda_{i,M} cos\theta \tag{2.3}$$

By performing the XPS experiments using fixed conditions for the spectrometer and by knowing the σ_i and L from the theoretical calculations by Scolfield[61] and Reilman, et. al.[62] respectively, a sensitivity factor S specific for a given core level can be obtained. Therefore, the fraction for a determined element i in a matrix of n components equals to:

$$X_i = {I_i/S_i}\Big/{\sum[I_n/S_n]} \tag{2.4}$$

Where S is the sensitivity factor that contains the values for $K,T, L, \sigma_i, \lambda_{i,M}$, for a given angle of emission θ, and I_n is the integrated intensity of the element n in the matrix. In this work, the sensitivity factors were obtained from the spectrometer's manufacturer (Physical Electronics, USA).[63]

Typically, the ejected photoelectrons travel finite distances through the material before they scatter either elastically or inelastically, which results in the attenuation of the electron signal as a function of depth. This electron signal attenuation can be described by the Beer-Lamber equation as:[60]

$$I = I_0 \exp\left(\frac{-d}{\lambda cos\theta}\right) \tag{2.5}$$

Where I_0 is the non-attenuated electron signal, d is the electron depth, θ is the emission angle, and λ, the inelastic mean free path or the average distance that an electron with a given energy travels between successive inelastic collisions. In practice, 3λ represents the depth from which 95% of the photoelectrons are detected at an emission angle parallel to the sample normal. Equation 2.5 also shows the dependence of the sampling depth with the emission angle, where near normal emission angles (e.g., $\theta = 0°$) are bulk sensitive and grazing emission angles (e.g., $\theta = 80°$) are surface sensitive. In fact, the expression for the XPS signal intensity in equation 2.5 can be applied to describe the photoelectron intensity from a substrate S with a thin overlayer A of thickness d. In this case, the overlayer will contribute to the attenuation of the substrate signal S as:

$$I_S = I_{0,S} \exp\left[\frac{-d}{\lambda_{S,A} cos\theta}\right] \tag{2.6}$$

And, the XPS signal intensity from the overlayer A corresponds to:

$$I_A = I_{0,A} \left[1 - \exp\left(\frac{-d}{\lambda_{A,A} cos\theta}\right)\right] \tag{2.7}$$

Where $I_{0,S(A)}$ are the signal intensities from thick S (A) layers, and $\lambda_{S,A}$ and $\lambda_{A,A}$ are the effective attenuation length of the photoelectrons in A emitted from the substrate and the overlayer, respectively. These expressions can be applied to estimate the layer thickness d of an overlayer based on the experimental integrated intensity ratio I_A/I_S at a given emission angle.

For the data acquisition, an X-ray photoelectron spectrometer is employed; a generic setup for the XPS spectrometer is presented in Figure 2.4. In this configuration, X-rays are generated from an X-ray anode to then pass through a monochromator, commonly composed of quartz crystals,

to produce photons of a single energy. The sample is irradiated by the monochromatic X-ray source and the ejected photoelectrons are collected by the analyzer system passing through the electrostatic lens, which retards the kinetic energy of the photoelectrons to the set passing energy of the energy analyzer. The photoelectrons enter to an hemispherical analyzer to determine their energy. The photoelectrons are counted once they exit the energy analyzer, by means of a multichannel detector.

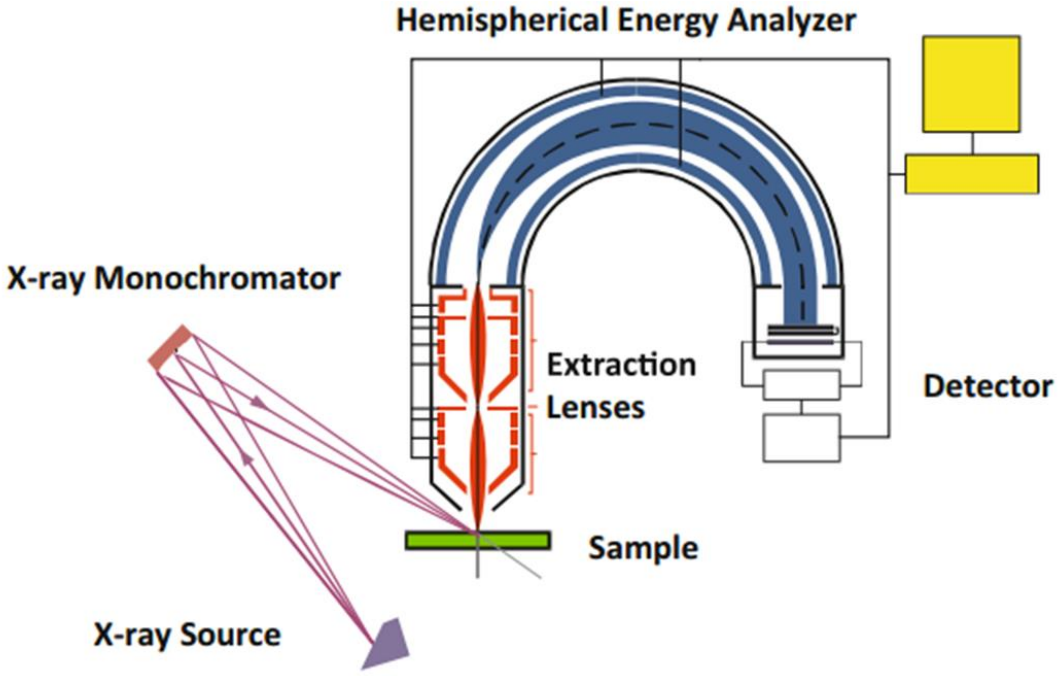

Figure 2.4. Schematic diagram of the setup for an X-ray photoelectron spectrometer. Reproduced from ref. [64]. Copyright © 2014, Springer Science+Business Media New York.

For the XPS experiments described in this work, an XPS spectrometer from Physical Electronics USA with a spectral resolution of ~0.5 eV was employed, equipped with an Omicron XM1000 quartz monochromator to filter the Al Kα component (hv= 1486.7 eV) from an Al anode. For the electron energy analysis, a 125 mm hemispherical analyzer was used along with 7 Channeltron®

detectors. In a typical XPS experiment, the hemispherical energy analyzer was operated at a pass energy of 15 eV.

The XPS spectrometer calibration of the binding energy was performed based on American Society for Testing and Materials (ASTM) Standard procedures.[65] The calibration consists in the measurement of the linearity of the binding energy and the repeatability standard deviation for the main calibration lines. To perform the calibration, the sputtered clean metals Au, Ag, Cu, are used, where the Au $4f_{7/2}$, Cu $2p_{3/2}$, Ag $3d_{5/2}$ peak positions are taken as the reference to extract the binding energy linearity and the spectrometer workfunction (Φ_{sp}). This procedure is performed every six months, and in the event of XPS system maintenance, the calibration is carried out after the procedures of the XPS anode outgassing.

The peak shape of the XPS spectra exhibits a lineshape commonly fit by the convolution of Gaussian and Lorentzian functions.[58] The subtraction of the background of the XPS spectra that is generated due to the inelastic processes and the energy loss processes is required for the correct extraction of the integrated peak intensity and peak position. In this work, the XPS peak analysis and deconvolution were performed using the software Aanalyzer, which allows the use of a Voigt function and a Shirley background subtraction in the peak fitting.[66]

2.1.2 Low Energy Electron Diffraction

Low-energy electron diffraction (LEED) is an electron diffraction technique employed to determine the surface structure of a crystalline material, by measuring the long and short range order from a surface.[60] In a LEED experiment, a low energy electron beam (50-200 eV) impinges on the sample surface and the diffracted electron beam is directed to a phosphorous

screen for the generation of the diffraction pattern, which can be recorded using a CCD camera. The diffraction pattern obtained from LEED represents the crystal lattice in the reciprocal space. The low energy provides the electrons with a shallow penetration depth of ~50-100 Å, depending on the energy spread and divergence of the incident beam, making this technique surface sensitive. In this work, LEED was carried out in-situ in the UHV cluster tool using a Scienta Omicron LEED tool, model Spectaleed. A range of beam energies between 80 eV-150 eV was set to obtain the LEED patterns from the TMDs surfaces.

2.2 Ex-Situ Materials Characterization Techniques

2.2.1 Raman Spectroscopy

Raman Spectroscopy is based on the molecular vibration of molecules and its interaction with electromagnetic radiation. Raman scattering or inelastic scattering occurs when the interaction of photons of a single frequency with molecules results in scattered photons with a different frequency than the initial radiation. This change in frequency or Raman shift corresponds to a determined molecular vibration mode of a molecule.[67] Only those vibrational modes that cause a polarizability change in the molecule will be Raman active and the possible vibrational modes are determined by group theory. Information about the phase of polymorphic solid, residual strain, identification of polymers and certain inorganic materials can be obtained from Raman spectroscopy.

Raman spectroscopy has been a widely employed technique for the identification two-dimensional TMDs, and for the evaluation of the crystal quality. Furthermore, the peak positions of the main Raman modes have been associated with the number of layers in a flake or a film,

allowing the determination the thickness in a convenient and practical manner.[68] For example, for bulk MoS_2, the characteristic Raman peaks have a Raman shift of ~382 cm^{-1} and ~ 407 cm^{-1} corresponding to the in-plane (E^1_{2g}) and out-of-plane (A_{1g}) vibrational modes, respectively. These peaks shift to lower and higher frequencies when decreasing the layer thickness, as presented in Figure 2.5.[69]

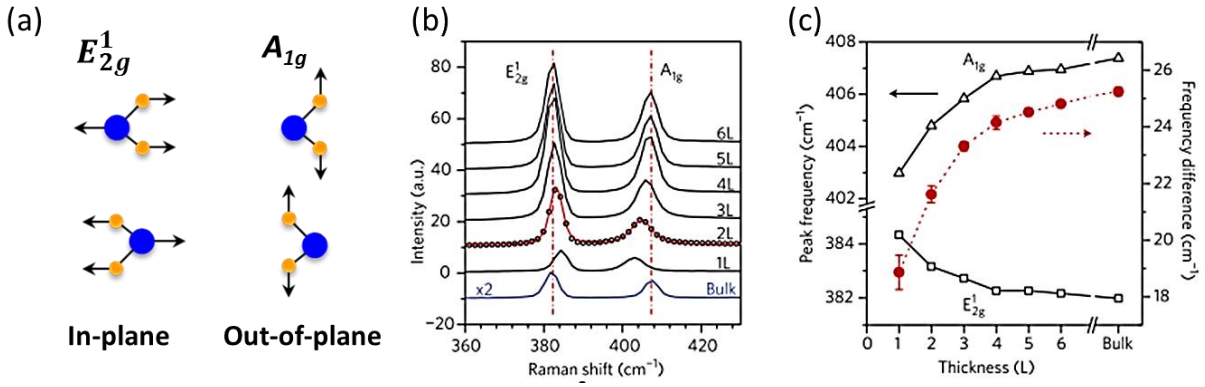

Figure 2.5. (a) Representation of the characteristic Raman modes in MoS_2. (b),(c) Layer dependence of the Raman peak positions in MoS_2 with layer thickness. Reprinted with permission from ref.[69].Copyright (2010) American Chemical Society.

Here, Raman spectra were acquired under air-ambient conditions using a Renishaw confocal Raman system model inVia using a 532 nm wavelength, with a laser power~0.22 mW, and spot size ~500 nm.

2.2.2 Atomic Force Microscopy

Atomic force microscopy examines and maps the surface topography of a material using a probe tip. The AFM operation is given by the near-field forces between the tip and the sample. Typically, the AFM tip employed to perform the surface scanning is mounted onto a cantilever spring. During operation, the forces between the tip and the sample are detected by a laser beam

deflection system. AFM offers a lateral resolution in the order of 0.1-3.0 nm for the measurement of the surface topography.[67] In this work, AFM measurements were carried out under air environment conditions using a Veeco, Model 3100 Dimension V atomic probe microscope, employing a Si-OTESPA tip for the measurements. The system was operated in tapping mode, and an amplitude voltage set point in the range of 200-350 mV.

2.2.3 Transmission Electron Microscopy

In transmission electron microscopy, an electron gun generates a high energy electron beam for the imaging of a specimen in a transmission mode. Due to the short wavelength of the electrons, a resolution in the order of ~0.1 nm can be achieved, by the proper correction of the lens aberration. The main components of a TEM system are electron source, condenser lens, specimen stage, objective lens and projecting lens. In addition, to increase the resolution, TEM is commonly operated at an acceleration voltage >100 kV.[67] Here, TEM imaging was employed to analyze the structure at the dielectric/TMDs interface. It was also used to investigate the structure of covalent-nitrogen doped MoS_2, as presented in Chapter 6. The TEM characterization was carried out by Dr. Ning Lu, Mr. Qingxiao Wang, and Mr. Xin Peng in collaboration with Prof. Moon J. Kim at UT Dallas. For these purposes, cross-sectional samples were made by the lift-out approach[70] using an FEI Nova 200 NanoLab dual-beam FIB/SEM system. High-resolution HRTEM imaging performed using a JEOL 2100F operated at 200 kV, and high angle annular dark field (HAADF) scanning transmission electron microscopy (STEM) performed using a JEOL ARM200F with probe spherical aberration (Cs) corrected operated at 200 kV, were both employed in this work.

2.3 Density Functional Theory

Density functional theory (DFT) is an ab-initio method applied to describe the ground state electronic properties of many-body systems such as atoms, molecules, and condensed phases.[71] For an N-electron atomic or molecular system, the energy can be described with the time-independent Schrodinger equation as:[72]

$$\hat{H}\Psi = \mathrm{E}\Psi \tag{2.8}$$

Where $\hat{H}$ is the Hamiltonian operator, E is the electronic energy, and Ψ is the wave function. For this system, the Hamiltonian can be expressed as:[71]

$$\hat{H} = \sum_1^N(-\frac{1}{2}\nabla_i^2) + \sum_1^N(v(r_i) + \sum_{i<j}^N \frac{1}{r_{ij}} \tag{2.9}$$

Where the external potential acting on electron i from the M nuclei of charges Z_α is a sum over all M nuclei

$$\mathrm{v}(r_i) = \sum_1^M(Z_\alpha / r_{i\alpha}) \tag{2.10}$$

In the approximation given by density functional theory, the energy is written as a function of the electron density, which is a function of three spatial variables. The basis of the density functional theory is provided by the Hohenberg-Kohn theorem.[71] This theorem states that (1) the non-degenerate ground-state electron density ρ_0 uniquely determines the external potential and that (2) the total energy functional has a minimum, which is the ground state energy E_0 at a unique ground state electron density ρ_0. Here, DFT calculations were carried out using a Viana ab-initio simulation package (VASP)[73] which uses a plane wave basis with pseudopotential approach allowing computation of large variety of materials properties. The DFT calculations were provided by Dr. Santosh K.C., Mr. Chenxi Zhang, and Prof. Kyeongjae Cho, performed at either

the multi-scale simulation lab (MSL) at UT Dallas or using the computing facilities provided by the Texas Advanced Computer Center (TACC) at the University of Texas at Austin.

2.4 Thin Film Deposition Technique

2.4.1 Atomic Layer Deposition

Atomic layer deposition (ALD) is a technique for deposition of thin-films by exposing the substrate to alternating pulses of different precursors. Different to a chemical vapor deposition process, in ALD, the precursor dosing steps are intermitted by purging steps to avoid direct reaction between the precursors.[74] This process allows the self-limiting reactivity of the precursors with the surface. As an example, the deposition of a metal-oxide material requires the use of a metallic precursor commonly in the form of an organometallic coordination compound and an oxidant precursor, commonly water. The thermal oxide dielectric ALD process consist of: (1) exposure of the first precursor on a substrate surface, (2) the purge of the reaction chamber to remove the unreacted precursors and the gaseous reaction by-products, (3) the oxidant precursor pulse and (4) the purge of the reaction chamber to evacuate unreacted precursors and reaction by-products, leaving a determined coverage of the metal oxide formed on the surface, as shown in Figure 2.6. The temperature range for a typical ALD process is 125-500℃,[75] depending on the precursor decomposition temperature and surface reactions. This process is repeated until the film reaches the desired thickness, according to deposition rate calibrations. Some of the advantages of ALD are the precise control of the film thickness at a monolayer level of few angstroms because the reactions are driven to completion during every reaction cycle, extremely

smooth and conformal (to the original substrate) films, and large area thickness uniformity and scalability. One disadvantage is that functionalization steps of the surface may be required.

Here, the dielectric depositions were performed in-situ in the UHV cluster tool, using a commercial Picosun™ thermal ALD reactor, which is kept at a base pressure of ~5 mbar. The dielectric materials Al_2O_3 and HfO_2 were investigated as dielectrics on the TMD surfaces, and for such oxides, trimethyl-aluminum (TMA) and tetrakis(dimethylamido)-hafnium were employed as metal-organic precursors, while deionized water and ozone (in specified cases) were used oxidant precursors.

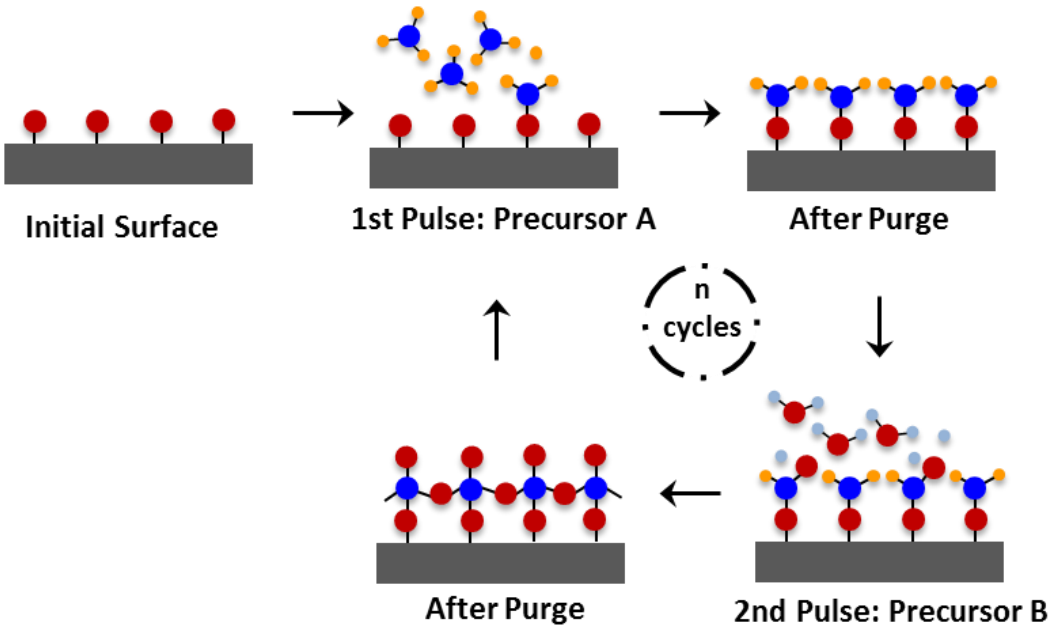

Figure 2.6. Schematic representation of the atomic layer deposition process.

2.5 Mechanical Exfoliation of Transition Metal Dichalcogenides

For the XPS measurements, bulk TMDs samples were employed. The use of exfoliated mono or few layer flakes was limited due to their dimensions, typically in the order of few microns, whereas the XPS spot size is ~0.5 mm. Natural bulk TMDs were purchased from SPI Supplies and 2D Semiconductors Inc. The initial surface was prepared by mechanical exfoliation of the outermost layers using the Scotch® Magic™ tape method,[1] as depicted in Figure 2.7

First, a piece of Scotch® Magic™ tape-(810) is adhered to the surface of the bulk material. Due to the weak van der Waals interaction between the layers, the outermost layers can be peeled off by gently removing the tape out of the surface.

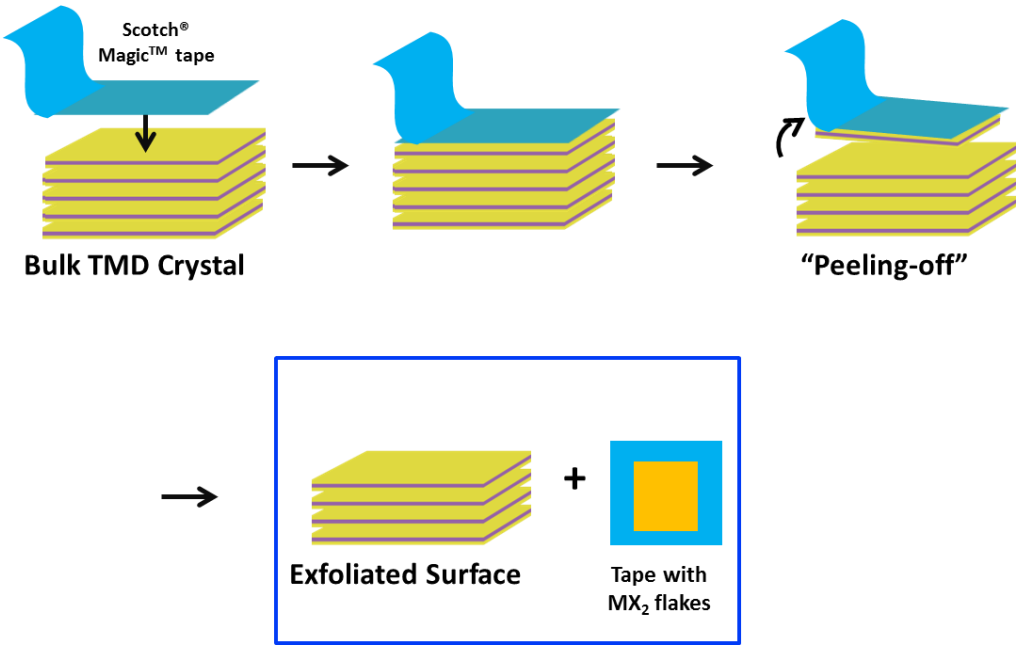

Figure 2.7. Schematic of the mechanical exfoliation process for layered TMDs.

The resulting surface leads to a smooth and flat surface as shown in Figure 2.8a, with a sporadic presence of irregular areas or step edges. The tape used in the mechanical exfoliation contains flakes of the TMD material, which can subsequently be transferred onto a substrate, commonly SiO2/Si, for the identification of mono or few layer flakes by optical microscopy by optical contrast as presented in Figure 2.8b.

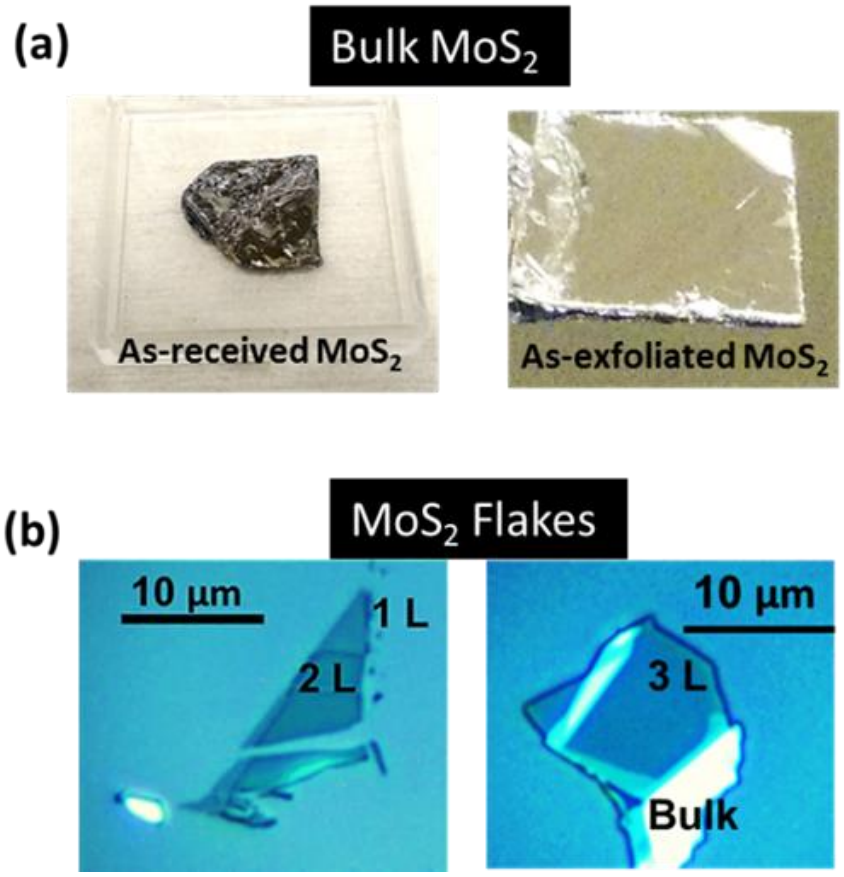

Figure 2.8. (a) Optical image for natural bulk MoS_2 as-received and after mechanical exfoliation of the outermost layers. (b) Optical image of exfoliated MoS_2 flakes transferred onto a 300 nm-SiO_2/Si substrate.

The identification of MoS_2 flakes on SiO_2/Si with a determined thickness can also be done by Raman spectroscopy. After mechanical exfoliation, the XPS survey spectrum from bulk MoS_2 in Figure 2.9 shows the characteristics core level peaks from MoS_2 and a C 1*s* signal due to adventitious carbon and/or from tape residues from the exfoliation process. Interestingly, the oxygen signal is at or below the XPS detection limits. The carbon signal detected on the as-exfoliated MoS_2 surface can be reduced to below detection limits by annealing at 300 °C for two hours under UHV, which indicates the carbon contaminants are only weakly adsorbed on the surface.

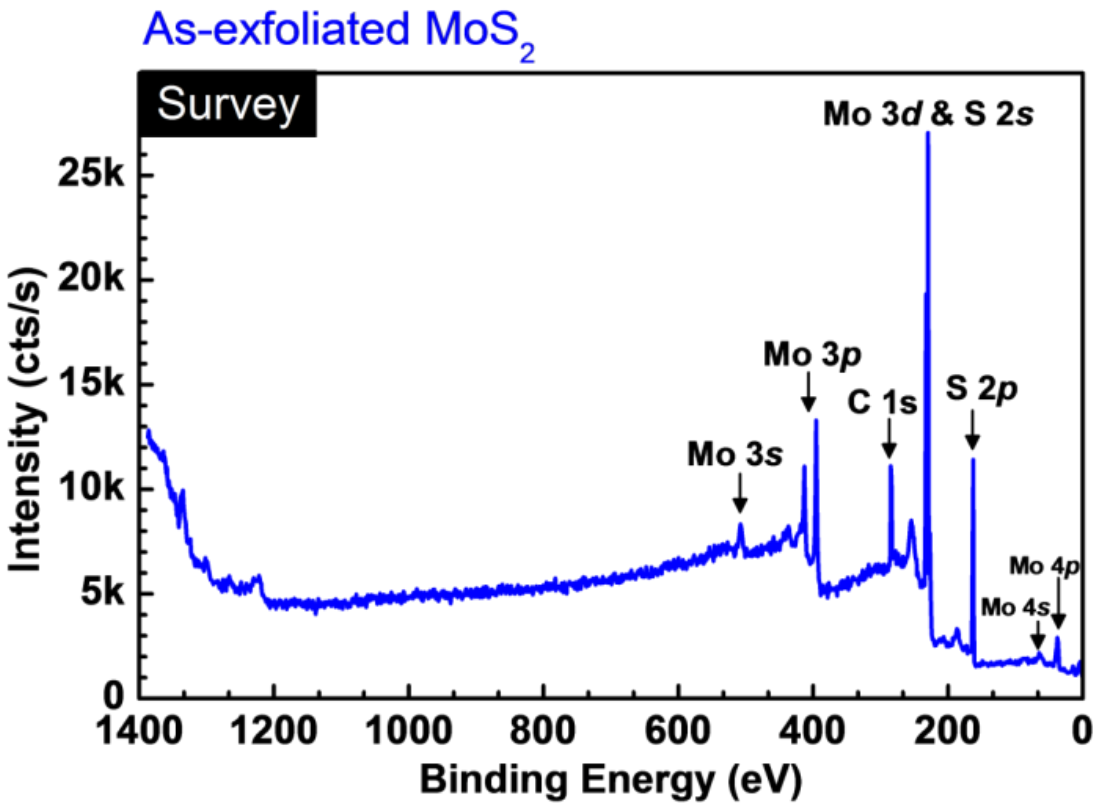

Figure 2.9.XPS Survey spectrum from ex-situ as-exfoliated bulk MoS_2.

Later, it is shown that a UV-O_3 exposure can also clean the adsorbed carbon contaminants from the MoS_2 surface. The XPS resulting spectra is shown in Figure 2.10, where it is shown that the vacuum annealing does not cause a change in the chemical state of MoS_2, and the oxygen level remains below detection limits upon annealing.

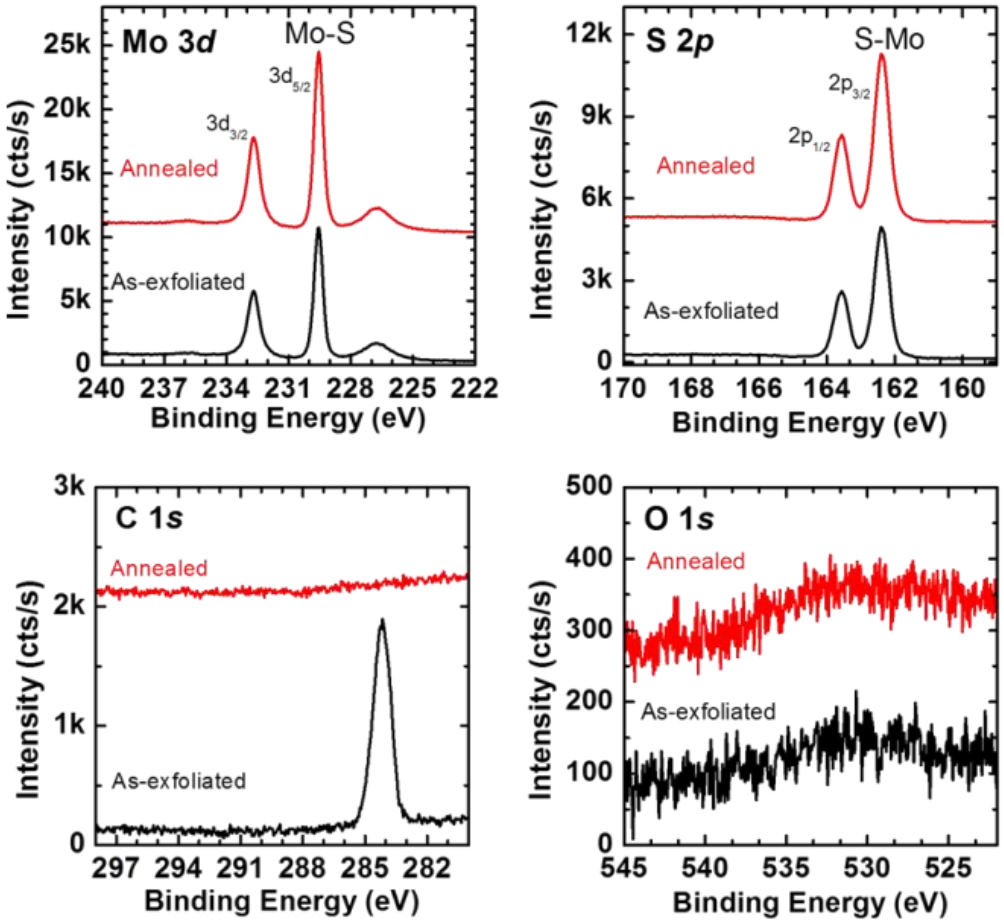

Figure 2.10. XPS spectra (Mo 3*d*, S 2*p*, C 1*s* and O 1*s*) of as-exfoliated bulk MoS_2 before and UHV annealing at 300 °C for two hours.

CHAPTER 3

SURFACE FUNCTIONALIZATION OF MOS_2 FOR HIGH-K DIELECTRIC DEPOSITION

3.1 Introduction

As scaling of the silicon-based complementary metal oxide-semiconductor is reaching its physical limits,[25] two-dimensional (2-D) transition metal dichalcogenides (TMDs) are being considered as ideal candidates for channel materials in field effect transistors (FETs) due to their atomic thickness and bandgap comparable to that of silicon.[7] Recent efforts in the integration of 2-D materials have reported promising results such as field effect electron mobility in the order of 470 $cm^2/ V{\cdot}s$ using multilayer MoS_2,[76] on/off ratios of $\sim 10^8$,[3] and a low interface trap density D_{it}.[77] It has been shown in the literature[4,78,79] that the presence of a high-κ dielectric material on top of the channel of 2-D material-based FETs induces an enhancement of the carrier mobility by one order of magnitude or higher; such situation has been attributed to dielectric screening effects.[80] Yet, uniform deposition of sub-10 nm dielectrics on TMDs by atomic layer deposition (ALD) results challenging due to their limited surface reactivity. McDonnell *et al.*[11] reported the HfO_2 deposition on bare MoS_2 leads to the formation of HfO_2 islands instead of a continuous film. In a different study, Liu *et al.*[81] showed the dependence of the Al_2O_3 nucleation on the deposition temperature during the ALD process on MoS_2. In that study, a temperature of 200 °C was proposed as an optimal condition to obtain uniform Al_2O_3 films of ~10 nm in thickness.

Later, Yang *et al.*[42] suggested that additional surface treatments for MoS_2 were needed to achieve thin and uniform as the conditions studied by Liu *et al.*[81] were not reproducible. Performing an oxygen plasma pre-treatment was demonstrated to improve the coverage of ALD-Al_2O_3 and HfO_2 on multilayer MoS_2 flakes.[42] However, by this method, MoO_3 was formed after the oxygen plasma treatment which could induce changes to the MoS_2 electrical properties due to the Mo-S bond disruption and modify the band alignments (i.e., MoO_3 is a semiconductor with a wide bandgap of ~3.1 eV, whereas the bandgap of monolayer MoS_2 is 1.8 eV). Consequently, the use of such aggressive treatment can degrade the dielectric/MoS_2 interface quality and would be impractical for monolayer-MoS_2 based devices.

In this chapter, the study of UV-O_3 treatment as a non-destructive method to functionalize the MoS_2 surface is presented. By this method, the selective formation of oxygen-sulfur (S-O) bonds at the topmost sulfur layer was achieved without breaking sulfur-molybdenum bonds (i.e., no formation of MoO_3). Additionally, first principle calculations were used to investigate the energetics that involves the formation of the S-O bonds in MoS_2. Then, it is demonstrated that the oxygen functionalized MoS_2 surface is an ideal nucleation layer for ALD, allowing deposition of fully-covered and uniform Al_2O_3 thin films of ~4 nm on MoS_2. According to the *in-situ* XPS interface studies, the S-O species is reduced by the ALD process as no detectable S-O bonding was presented at the Al_2O_3/MoS_2 interface. The DFT calculations show that S-O bonding and the substitutional O bonding (O on a sulfur vacancy) has a minimal impact on the MoS_2 bandgap for coverages less than 10%. This work highlights the importance of the UV-O_3 treatment as a route toward high-quality ultra-thin dielectrics on transition metal dichalcogenide 2-D materials.

This chapter includes the material adapted with permission from a publication entitled **"MoS_2 functionalization for ultra-thin atomic layer deposited dielectrics"** [Appl. Phys. Lett. 2014, 104, 111601] Copyright 2014, AIP Publishing LLC. The authors are A. Azcatl, S. McDonnell, S. K. C., X. Peng, H. Dong, X. Qin, R. Addou, G.I. Mordi, N. Lu, J. Kim, M. J. Kim, K. Cho, and R. M. Wallace. My contribution was in planning, executing and analyzing the XPS, LEED, and AFM characterization, and writing the manuscript. The theoretical calculations by first principles density functional theory were performed by S. K. C. and K. Cho, and X. Peng, N. Lu, and M. J. Kim provided the TEM characterization. S. McDonnell, H. Dong, X. Qin and R. M. Wallace are acknowledged for the valuable input in guiding the experiments and manuscript writing.

3.2 Experimental Details

In this work, the UV-O_3 exposures were performed on the MoS_2 surface, and *in-situ* XPS was employed to monitor the chemical state changes without exposure of samples to the environment to avoid spurious contamination. The bulk MoS_2 crystal (SPI Supplies) was mechanically exfoliated using Scotch® Magic™ Tape to remove the outermost layers. The freshly exfoliated MoS_2 sample was then loaded into the ultrahigh vacuum (UHV) system within 5 min for XPS characterization of the initial surface. Then, the sample was transferred for UV-O_3 treatment to a chamber equipped with a low-pressure mercury lamp (BHK Inc.). Ozone was produced by UV photons[82] at an O_2 pressure of PO_2 = 900 millibar, where the sample surface was placed within a few mm of the mercury lamp. A detailed setup and process flow for the UV-O_3 treatment is presented in Appendix A. After UV-O_3 treatment, *in-situ* low energy electron diffraction (LEED) was performed at a beam energy of 127 eV under UHV environment. To investigate the energetics related to the interaction of oxygen with MoS_2, DFT calculations were carried out,

where a plane wave basis set and Projector Augmented Wave (PAW) pseudopotentials were implemented in the Vienna Ab-initio Simulation Package (VASP). The electronic wave functions are represented by plane wave basis with a cutoff energy of 500 eV. The exchange-correlation interactions are incorporated as a functional of Generalized Gradient Approximation (GGA). A model of 5×5 supercell of MoS_2 with the periodic slab separation of 16 Å vacuum in order to avoid spurious interaction between the two surfaces of the slab was used. In these calculations, the atoms are allowed to relax while the cell size is kept fixed. The DFT calculation and related analysis were provided by Dr. Santosh KC and Prof. Kyeongjae Cho at UT Dallas.

Following the UV-O_3 surface pretreatment on MoS_2, ALD experiments were performed in an attached Picosun SUNALE™ ALD reactor allowing for deposition and analysis without air exposure. Trimethyl-aluminum (TMA) and H_2O were used as the metal and oxidant precursors for Al_2O_3 deposition, respectively, while for HfO_2 deposition, tetrakis(dimethylamido)-hafnium and H_2O were employed. The precursor pulse and purge times were 0.1 and 4 s, respectively, at an operating pressure of P ≅ 10 mbar, using ultra-high purity N_2 as the carrier and purging gas. To investigate the Al_2O_3 coverage on MoS_2, *ex-situ* atomic force microscopy (AFM) was obtained in tapping mode from an Atomic Probe Microscope Veeco, Model 3100 Dimension V, located at the UT Dallas Cleanroom Facility. High-resolution transmission electron microscopy (HRTEM) imaging was performed using a JEOL 2100F operated at 200 kV. Transmission electron microscopy (TEM) cross-sectional samples were made by the lift-out approach[70] using an FEI Nova 200 NanoLab dual-beam FIB/SEM system. An Au layer (~70 nm) was e-beam deposited on the Al_2O_3 surface to eliminate electron charging. Layers of SiO_2 and Pt were also deposited to protect the region of interest during focused ion beam milling. TEM sample

preparation and HRTEM imaging were performed by M.S. Xin Pen, Dr. Ning Lu and Prof. Moon J. Kim at UT Dallas.

3.3 UV-O_3 Exposure on MoS_2

UV-O_3 treatment of the surface has been widely employed for surface cleaning purposes, as well as a method to form a thin oxide on semiconductor surfaces, such as silicon. Here, UV-O_3 was investigated to determine the effect this treatment on the MoS_2 surface chemistry by in-situ XPS characterization. The process employed for this purpose is described in Figure 3.1, where the UV-O_3 treatment was performed for 15 minutes at room temperature.

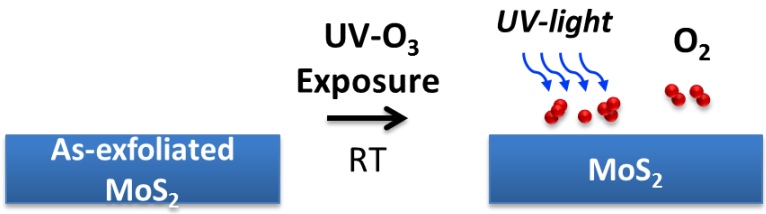

Figure 3.1. Schematic of the process for in-situ surface characterization by XPS for MoS_2 upon UV-O_3 exposure.

The XPS spectra of the initial as-exfoliated MoS_2 surface are shown in Figure 3.2, where characteristic peaks for the Mo-S bonds are detected. In MoS_2, molybdenum provides four electrons to fill the bonding states having an oxidation state of +4, whereas the oxidation state for sulfur is −2. The XPS peak positions for these elements in MoS_2 are Mo $3d_{5/2}$ at 229.5 eV and S $2p_{3/2}$ at 162.4 eV. As reported by McDonnell *et al.*,[35] a variation of these peak positions is commonly observed due to the variability in the unintentional doping type across the surface. After UV-O_3 treatment, the S *2p* spectrum showed an additional doublet peak at 164.8 eV, and concurrently, a peak at 530.6 eV was detected in the O 1*s* spectrum, suggesting oxidation of

sulfur. The fact that the additional S 2*p* feature appeared at higher binding energy than the Mo-S bond indicates the presence of sulfur in a higher oxidation state than S^{-2}. Yet, the binding energy of 164.8 eV is lower than of SO_x (168.8 eV), which was reported to be formed upon oxidation of MoS_2 by RF-oxygen plasma[83]. Therefore, the new sulfur state is likely to be due to oxidation induced by the formation of a covalent sulfur-oxygen bond (S-O).

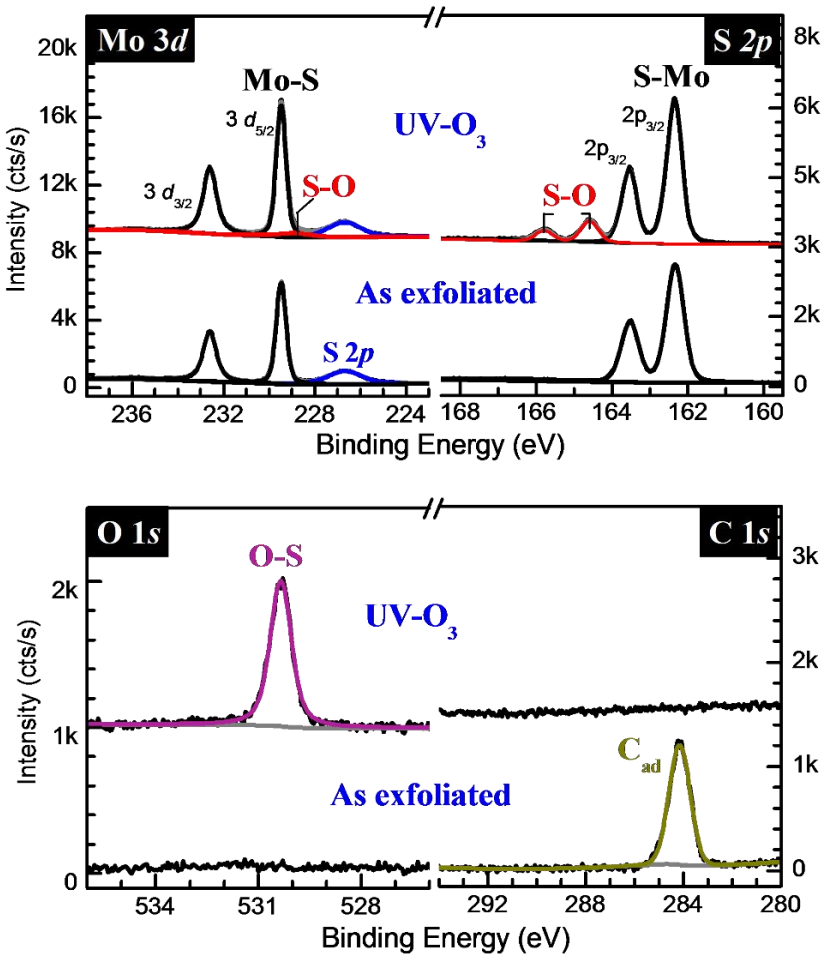

Figure 3.2. XPS spectra for the initial as-exfoliated MoS_2 surface and after UV-O_3 exposure for 15 min, showing the changes in the S 2*p* and Mo 3*d*, O 1*s* and C 1*s* core levels. k=1000.

Interestingly, in the Mo *3d* spectra, no metallic Mo (Mo^0 at 227.9 eV)[35] or Mo-O bonds (MoO_x at 232.7 eV)[42] were detected. The oxygen concentration is confirmed to be below the limit of

detection while carbon (C_{ad}), present in a mixture of graphitic and sp^3 hydrocarbons, is the only detectable contaminant on the *ex-situ* exfoliated MoS_2. The carbon coverage on MoS_2 was calculated to be ~0.5 monolayer, which was likely to be adsorbed from the environment after the exfoliation process. The oxygen coverage on the MoS_2 surface was calculated using the ratio of the S-O peak intensity ($I_{S\text{-}O}$) to total sulfur peak intensity from the S-O and S-Mo bonds (I_S). From the MoS_2 structure, I_S corresponds to the summarized intensity from the top (S_1) and bottom (S_2) sulfur layers as shown in Figure 3.3, with the total intensity of sulfur being equal to $I_{S1} + I_{S2}$.

Therefore, the $I_{S\text{-}O}/I_S$ ratio follows the equation (3.1):

$$\frac{I_{S-O}}{I_S} = \frac{I_{S-O}}{I_{S1}+I_{S2}} \tag{3.1}$$

This equation assumes that S-O layer is not attenuated by any overlayer ($I_{S\text{-}O} = I_{monolayer}$) and that the UV-$O_3$ treatment did not change the MoS_2 structure.

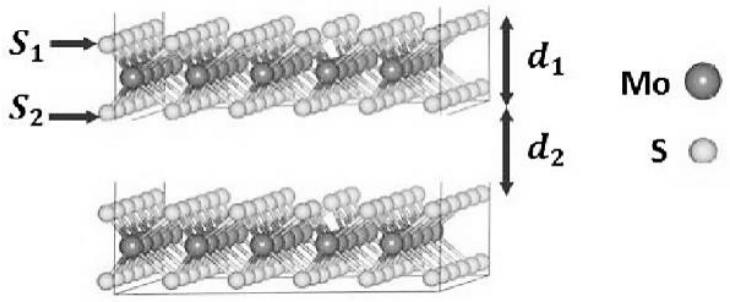

.

Figure 3.3. The layered structure of MoS_2 employed to create the model to calculate the oxygen coverage from the S 2*p* peak intensities. d_1= 0.316 nm and d_2= 0.30 nm are the S_1 to S_2 distance within the MoS_2 layer and the van der Waals interlayer distance, respectively.[84]

The signal intensities for S_1 and S_2 are calculated as follows:

$$I_{S_1} = I_{monolayer}\left[e^0 + e^{-\delta} + e^{-2\delta} + \cdots\right] = \frac{I_{monolayer}}{1-e^{-\delta}} \tag{3.2}$$

$$I_{S_2} = I_{monolayer}\, e^{-\frac{d_1}{\lambda sin\theta}}\left[e^0 + e^{-\delta} + e^{-2\delta} + \cdots\right] = I_{monolayer}\,\frac{e^{-\frac{d_1}{\lambda sin\theta}}}{1-e^{-\delta}} \quad (3.3)$$

Where, $\delta = \frac{(d_1+d_2)}{\lambda sin\theta}$

Thus,

$$\frac{I_{S-O}}{I_S} = 1/\left[\frac{1+e^{-\frac{d_1}{\lambda sin\theta}}}{1-e^{-\delta}}\right] \quad (3.4)$$

Here, the distances d_1 and d_2 correspond to 0.316 nm and 0.30 nm according to X-ray diffraction measurements.[84] The effective attenuation length (λ) for an electron traveling through MoS_2, λ_{MoS_2}=2.542 nm as calculated from the NIST electron EAL Database, version 1.3, and the take-off angle θ = 45°with respect to the surface plane. According to equation (3.4), the theoretical value for the $I_{S\text{-}O}/I_S$ ratio equals to 0.1330. Experimentally, the peak intensity ratio $I_{S\text{-}O}/I_S$ obtained from XPS corresponds to 0.1403 for the spectra obtained after 15 min of UV-O_3 exposure shown in Figure 3.1, which corresponds to an oxygen coverage of 1.05 monolayer (ML). Such coverage suggests that the topmost surface of MoS_2 is oxygen functionalized. It was also found from the S 2*p* and O 1*s* spectra that the S:O ratio the corresponding to the S-O bond is 1:1.3, indicating that oxygen could be not only bonded on top of each surface sulfur atom but also could occupy interstitial sites or sulfur vacancies. Interestingly, the analysis of several MoS_2 samples indicated that a S:Mo ratio of 1.93 $\pm$0.06 is obtained after UV-O_3 treatment, with an initial S:Mo ratio varying from ~2.3-1.8 for the as-exfoliated bulk MoS_2.[35] Additionally, as shown in Figure 3.1, the C 1*s* feature was no longer detectable after UV-O_3 treatment suggesting that carbon species were removed, likely through CO and/or CO_2 formation as reported for other

semiconductor surfaces,[82,85] without causing photochemical degradation as can occur for other two-dimensional materials, such as graphene.[86]

The interaction of oxygen with MoS_2 surface was studied by Density Functional Theory (DFT). As shown in Figure 3.4, the oxygen adatom has two possible adsorption sites: oxygen on top of sulfur (O_{ads}) and substitutional oxygen on a sulfur vacancy (O_S), having formation energies of -1.2 eV and -1.91 eV respectively. A previous study of MoS_2 surface defects showed that metallic defects (likely clusters of sulfur atoms) cover only 0.1-5% of the surface.[35] As such, for ~ 1 monolayer coverage of S-O species, the oxygen adsorbed on sulfur vacancy sites would have intensities below the limit of detection of XPS. Importantly, the DFT result highlights that the formation of S-O bonds is energetically favorable and can occur without Mo-S scission, which is consistent with the Mo and S chemical states shown in Figure 3.1. Moreover, the density of states (DOS) calculation shows that for low coverages of O adatoms (~0.1 ML), no gap states exist in the band gap, but rather shallow states at the band edge are created. The minimal effect of the oxygen adsorption on the MoS_2 bandgap results desirable as the electronic properties of this 2D semiconductor are being preserved after the oxygen functionalization. The calculation also shows that S mono-vacancy formation energy is relatively large (~2.45 eV) and a sulfur di-vacancy is less favorable than mono-vacancy. Furthermore, Zhou *et al*.[87] reported. Therefore, in the absence of pre-existing S vacancy, it would be even more unlikely for oxygen to replace sulfur, which is consistent with the detection of O-S bond formation without detectable O-Mo formation.

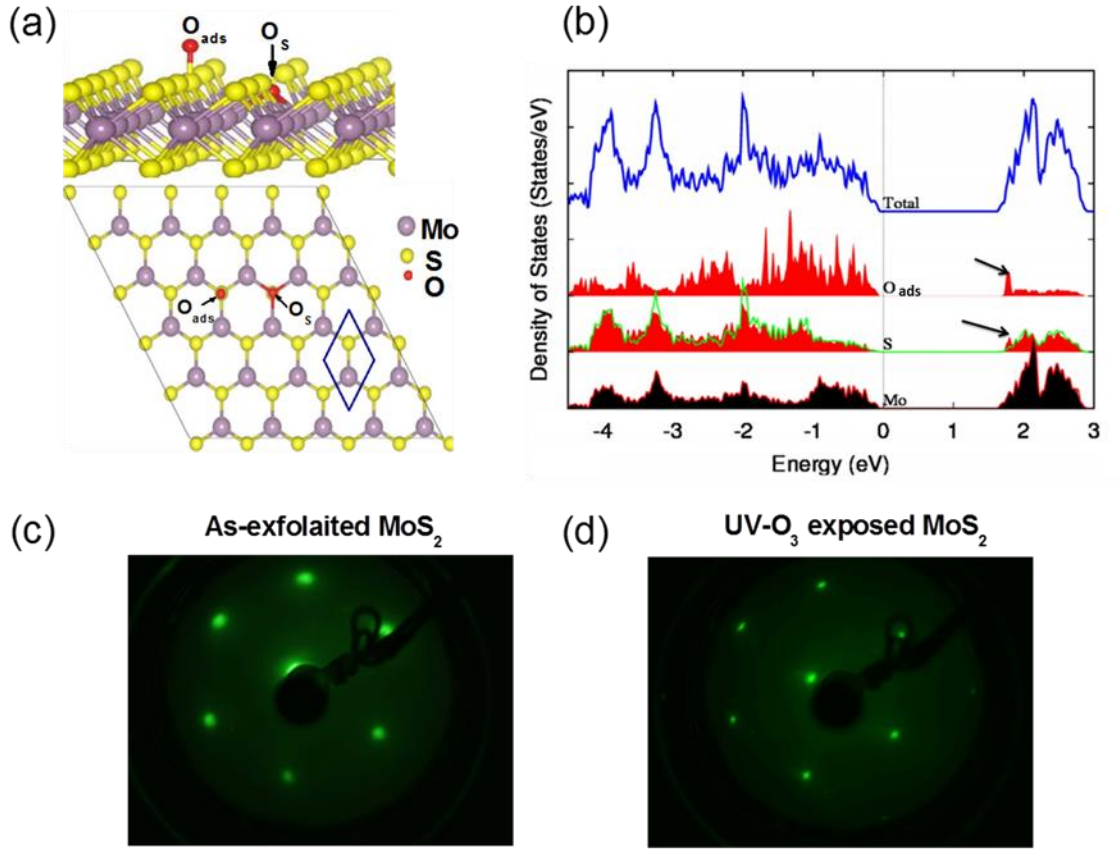

Figure 3.4 (a) (5×5) supercell of MoS_2 showing the most energetically stable adsorption sites for oxygen: oxygen on top of sulfur (O_{ads}) and substitutional oxygen on a sulfur vacancy (O_S). (b) Density of States (DOS) of MoS_2 generated upon O chemisorption on the O_{ads} adsorption site. Low energy electron diffraction pattern of (c) the initial as-exfoliated MoS_2 surface and (b) after UV-O_3 exposure, taken at a beam energy of 127 eV.

To investigate the surface structure of MoS_2 upon oxygen chemisorption upon UV-O_3 exposure, low energy electron diffraction was carried out. The LEED pattern on Figure 3.4 shows the characteristic hexagonal pattern of the unreconstructed MoS_2 (0001) surface[88] for the as-exfoliated surface. After the UV-O_3 treatment, sharper spots were observed likely due to the removal of the carbon contamination from the surface, as shown in Figure 3.1. Upon oxygen chemisorption, the hexagonal pattern spacing was not altered suggesting that the oxygen

adsorption sites are well-defined. In fact, the LEED pattern obtained after UV-O_3 treatment is in agreement with the most probable adsorption sites for oxygen, O_{ads} and O_S, calculated by DFT. In addition to LEED characterization, further studies were carried out on the oxygen functionalized MoS_2 surface to determine possible etching effects. Previous reports showed that when natural MoS_2 is treated with RF-oxygen plasma, MoO_x particles developed on the surface with a height of a few nanometers and length of 60-90 nm.[89] Such features were attributed to the breakage of the surface basal plane via etching and oxidation of molybdenum and sulfur. As shown in Figure 3.5, after UV-O_3 treatment, the MoS_2 surface remains smooth and no additional nanoscale features were observed. A minimal change in RMS roughness was measured in reference to the as-exfoliated MoS_2 sample. This result is consistent with our observations of lack of disruption of the MoS_2 surface given by in-situ XPS and LEED.

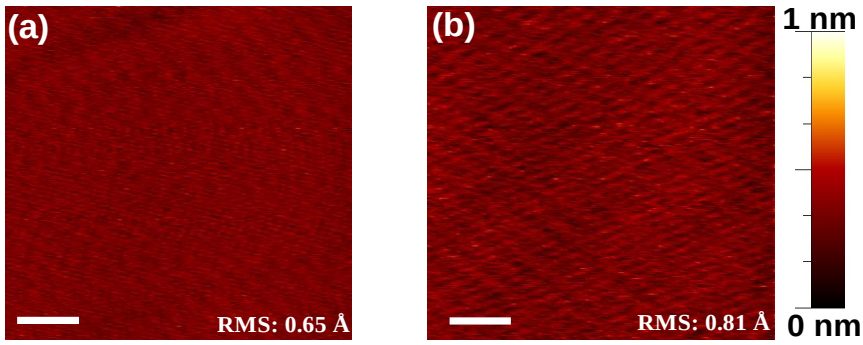

Figure 3.5. AFM images of bulk MoS_2 (a) as-exfoliated and (b) after UV-O_3 treatment. Scale Bar: 60 nm.

In the UV-O_3 process, along with the UV photons, chemical species such as atomic oxygen, molecular oxygen, and ozone are expected to be present, where atomic oxygen is generated by the dissociative reaction of O_2 and O_3 promoted by UV-light absorption.[82] To identify the reactive species that contribute to the oxygen functionalization of MoS_2, atomic oxygen and

ozone exposures were performed separately at room temperature without UV illumination. For the atomic oxygen exposure, an oxygen cracker was employed to perform the exposure on the MoS_2 surface at a pressure of 1.0 x 10^{-6} mbar during 10 min. The ozone exposure was performed using ozone generated from a remote source, at an ozone partial pressure of 900 mbar for 15 min. The *in-situ* XPS spectra are shown in Figure 3.6 for MoS_2 after ozone and atomic oxygen exposure.

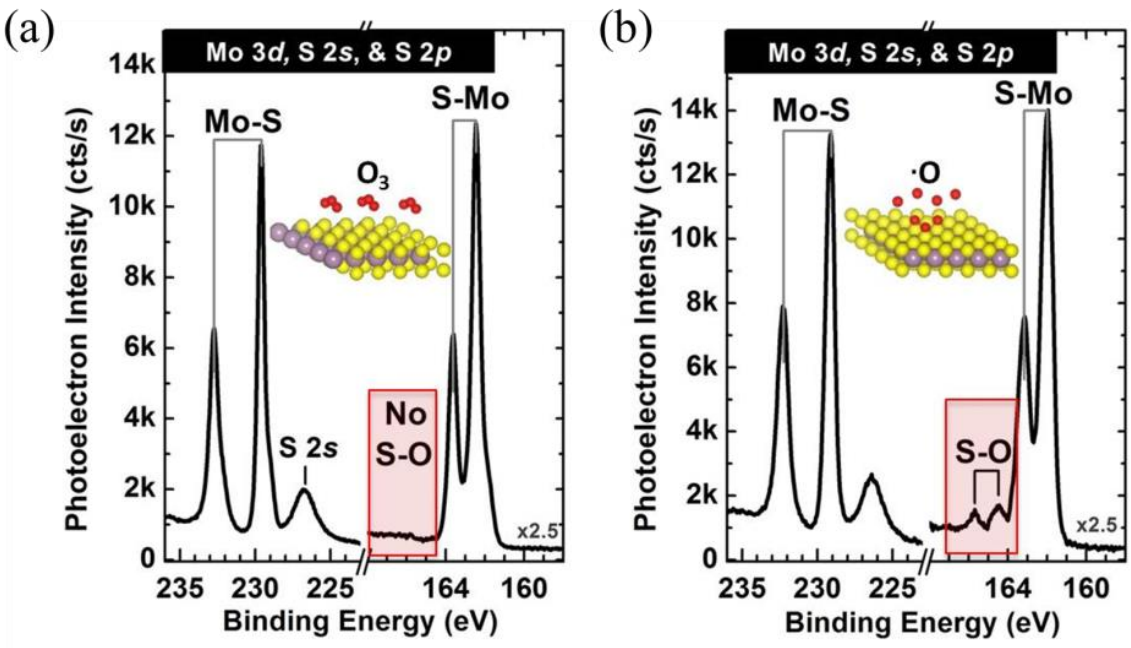

Figure 3.6. XPS spectra for MoS_2 (Mo 3*d*, S 2*s* and S 2*p* core levels) after (a) ozone exposure and (b) atomic oxygen exposure, both performed at room temperature.

It was found that the S-O bond was formed upon atomic oxygen exposure without molybdenum oxidation, which is analogous to the UV-O_3 exposure process. In contrast, there were no detectable S-O or Mo-O bonds after ozone exposure. Therefore, atomic oxygen is expected to be the main reactive species involved in the sulfur oxidation during the UV-O_3 treatment on MoS_2.

This result also suggests that the contribution of the UV illumination in the formation of the S-O bonds in MoS_2 is essential mainly to generate atomic oxygen from the dissociative reaction of O_2 and O_3 during the UV-O_3 process. Importantly, bulk MoS_2 is known to be a resistant material against photodegradation because the optical transitions occur between the d-states, and these will not affect or weaken bonds between the Mo and S atoms.[90] Only nanoscale MoS_2 clusters have been reported to be photochemically active for $\lambda > 400$ nm due to the increased surface area and reactive edges in comparison to bulk MoS_2.[91] Since the photochemical reactivity of bulk MoS_2 is negligible upon UV-light irradiation, its surface is not likely to catalyze or be involved in the O_3 or O_2 dissociation.

3.4 Atomic Layer Deposited Al_2O_3 on Oxygen Functionalized MoS_2

As discussed earlier, nucleation of dielectrics on TMDs is limited by the dearth of dangling bonds on these surfaces. However, for nanoelectronic applications, pin-hole free dielectric films with a uniform thickness are required. Therefore, the presence of S-O bonds at the functionalized MoS_2 surface could potentially enhance the nucleation in the ALD process. To investigate this hypothesis, Al_2O_3 depositions were carried out on UV-O_3 treated MoS_2 samples, at different temperatures and identical number of ALD cycles (30 cycles), and the interface chemistry of the Al_2O_3/MoS_2 stacks was investigated by in-situ XPS.

The XPS core levels, Mo 3*d* and S 2*p*, corresponding to the O-functionalized MoS_2 after Al_2O_3 deposition are presented in Figure 3.7. Interestingly, the S-O bonds are no longer detected in the S 2*p* core-level spectrum after Al_2O_3 deposition for all the studied temperatures. Instead, the XPS spectra shows that MoS_2 preserved its chemical identify after the ALD process. It is worth to

mention that since the total processing time for the 30 cycle films considered in this study is ~ 10 minutes and detectable S-O bonds are observed after 20 minute annealing at 150 °C, 200 °C and 250 °C, thermal desorption alone cannot explain the complete removal of the S-O feature during deposition.

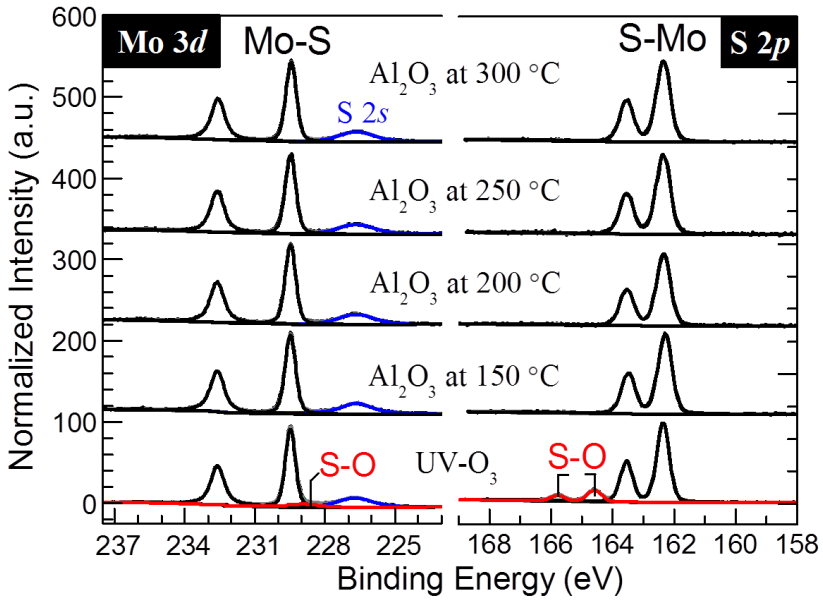

Figure 3.7. Mo 3*d* and S 2*p* XPS spectra from oxygen functionalized MoS_2 after Al_2O_3 deposition by ALD at 150 °C, 200 °C, 250 °C, and 300 °C.

It is likely that, in addition to thermal desorption, there is a direct reaction of the precursors with oxygen, similar to the self-cleaning effect reported for ALD on III-Vs.[92] Thus, the chemisorbed oxygen on MoS_2 acts as a sacrificial layer that is removed after the precursor pulsing and leaving a clear oxide-free MoS_2 surface. It is also noted that there is no detection of Mo-Al or S-Al chemical bonds, suggesting a non-covalent bonding of Al_2O_3 on MoS_2, similar to the case of HfO_2 on MoS_2. In the Al_2O_3 films, O-H bonds were present for all the deposition temperatures studied in this work. Also, various carbon species were present in the Al_2O_3 films possibly from

by-products of the ALD reactions, as shown in Figure 3.8. Interestingly, the deposition at 300 °C exhibited high carbon and O-H bond atomic percentage, indicating that the ALD reactions were not totally completed to form Al_2O_3 , which can be correlated to the minimal oxygen coverage at this temperature.

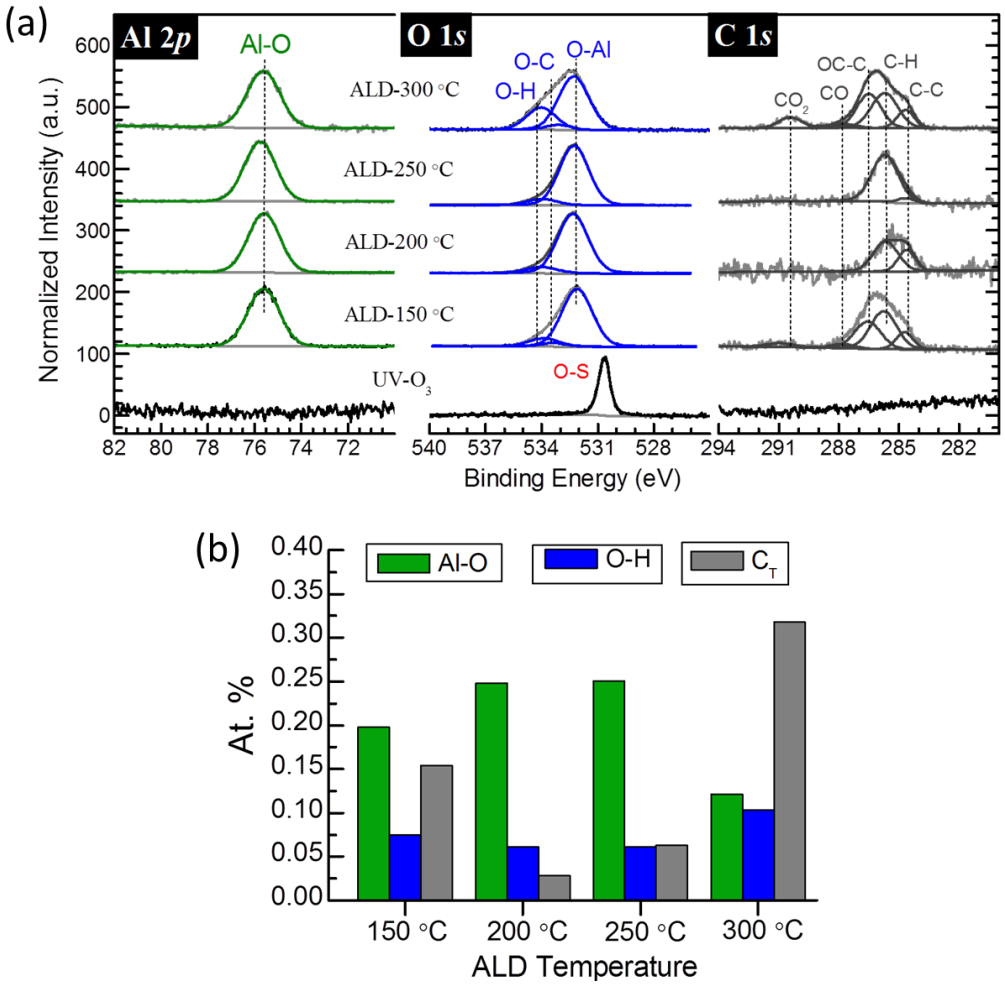

Figure 3.8. (a) Al 2*p*, O 1*s* and C 1*s* XPS spectra from O-functionalized MoS_2 before and after Al_2O_3 deposition by ALD at different temperatures. (b) Atomic percent (at.%) corresponding to the Al-O, O-H bonds and the total carbon concentration (C_T), calculated from the XPS spectra shown in (a).

A minimal carbon concentration was obtained at 200 °C, and for this reason, this temperature is suggested to be the optimal temperature for Al_2O_3 deposition by ALD on UV-O_3 treated MoS_2.

Figure 3.9 shows the Al-O peak intensity obtained in Al 2*p* for after 30 ALD cycles at deposition temperatures of 150 °C, 200 °C, 250 °C, and 300 °C (typical temperatures for ALD-Al_2O_3 processing)[93] on the UV-O_3 treated MoS_2 surface. The spectra of Al_2O_3 on exfoliated MoS_2 are also presented as reference. Interestingly, a significant increase in the Al_2O_3 deposition was achieved for the UV-O_3 treated MoS_2 samples in comparison to the as-exfoliated MoS_2, for all the studied deposition temperatures. The dependence of the Al-O peak intensity with the temperature is indicative of differences in the surface coverage of Al_2O_3 on the MoS_2 surface.

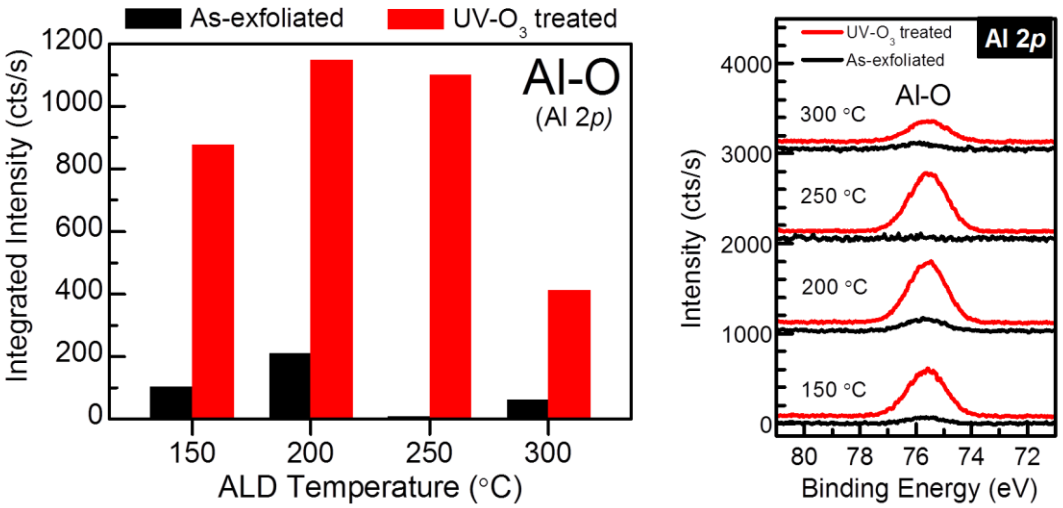

Figure 3.9 Integrated intensity of the Al-O bond detected in Al 2*p* on MoS_2 upon deposition of Al_2O_3 by ALD at different temperatures.

To correlate such differences in the Al-O peak intensities detected by XPS, the Al_2O_3 coverage on MoS_2 was investigated employing ex-situ atomic force microscopy (AFM). For the AFM experiments, the samples employed were identical to those prepared for the XPS analysis, using 30 cycles of TMA/H_2O to deposit Al_2O_3 at 150 °C, 200 °C, 250 °C, and 300 °C. The resulting AFM images are presented in Figure 3.10. It is evident that the nucleation occurs sporadically on

the as-exfoliated MoS_2, being favored at step edges. The density and size of the Al_2O_3 clusters on the surface were higher at lower temperatures. This result also demonstrates that the uniform Al_2O_3 after 110 cycles at 200 °C demonstrated by Liu *et al.*[81] could be caused by unintentional functionalization due to organic contaminants on the MoS_2 surface.[11]

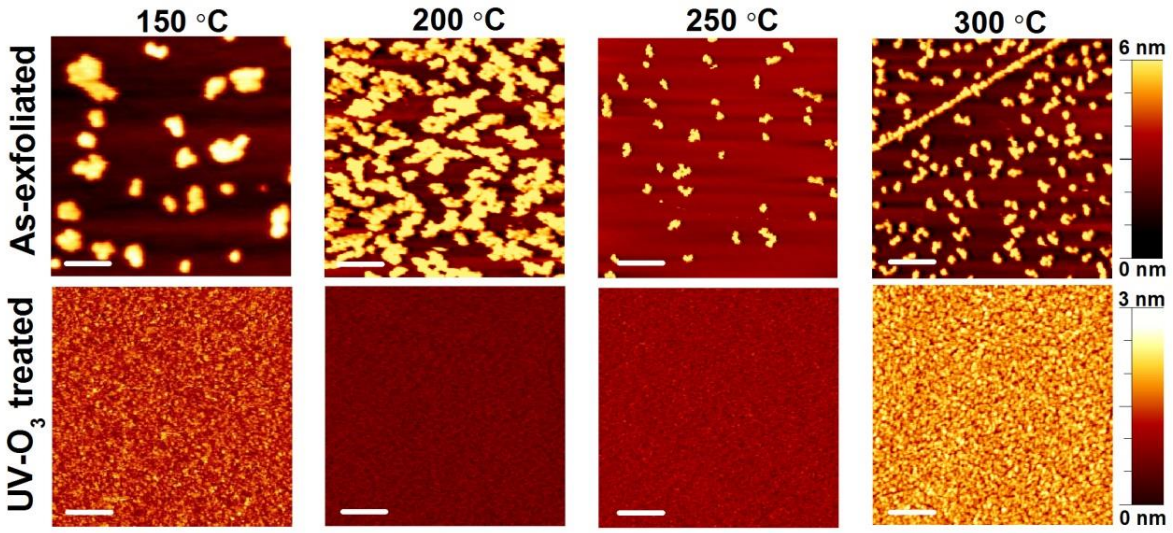

Figure 3.10. Atomic force microscopy (AFM) images of Al_2O_3 deposited by 30 ALD cycles at different deposition temperature on as-exfoliated and oxygen-functionalized MoS_2. Scale bar: 200 nm.

In contrast, the Al_2O_3 films deposited on the O-functionalized MoS_2 surface exhibited a significant improvement in nucleation, which is reflected in the observed surface coverage. The Al_2O_3 films showed RMS roughness values of only 0.31 nm, 0.14 nm, 0.17 nm, and 0.30 nm, for deposition temperatures of 150 °C, 200 °C, 250 °C, and 300 °C, respectively. Interestingly, only the film deposited at 300 °C presented pin-holes, having a depth of ~ 1 nm. The presence of pin-hole in this film suggests that the effect of the surface functionalization on the ALD nucleation was degraded at 300 °C. The Al_2O_3/MoS_2 interface of these films was also investigated by high-resolution transmission electron microscopy (HRTEM). The cross-section images in Figure 3.11

show a sharp interface between Al_2O_3 and MoS_2, where the Al_2O_3 films present an amorphous structure and MoS_2 presents the characteristic layered structure, which was not disrupted after the UV-O_3 treatment. Importantly, thin and fully-covered Al_2O_3 films were obtained at 200 °C, with a uniform thickness of only ~4 nm. Similar films were obtained at 250 °C, with the primary difference being an increase in surface roughness. However, the films deposited at 300 °C exhibit island-type growth, which is consistent with the appearance of pin-holes of 1 nm for the corresponding AFM image. Therefore, a clear dependence of film uniformity with deposition temperature was identified. The RMS roughness increase with deposition temperature suggests that the oxygen functionalization layer might not be stable at temperatures greater than 200 °C.

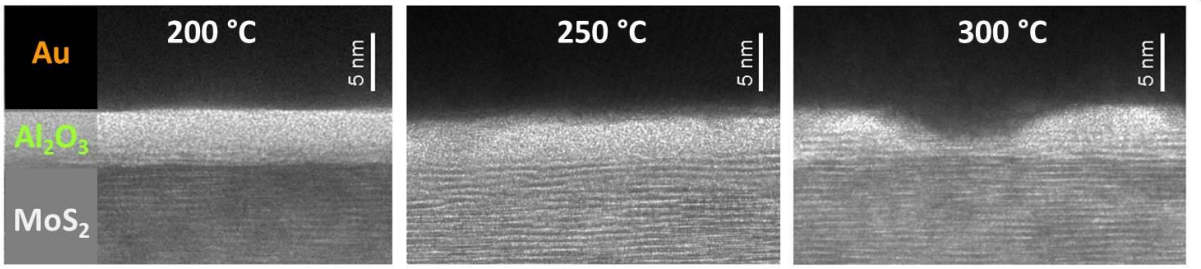

Figure 3.11. High resolution transmission electron microscopy (HRTEM) images of the Al_2O_3 films deposited on the O-functionalized MoS_2.

To test this hypothesis, identical O-MoS_2 samples were prepared and then exposed to the same deposition temperatures in the ALD reactor for 20 min under N_2, at ~10 mbar without precursor exposure. These surfaces were analyzed in-situ by XPS, and the resulting S 2p spectra are presented in Figure 3.12.

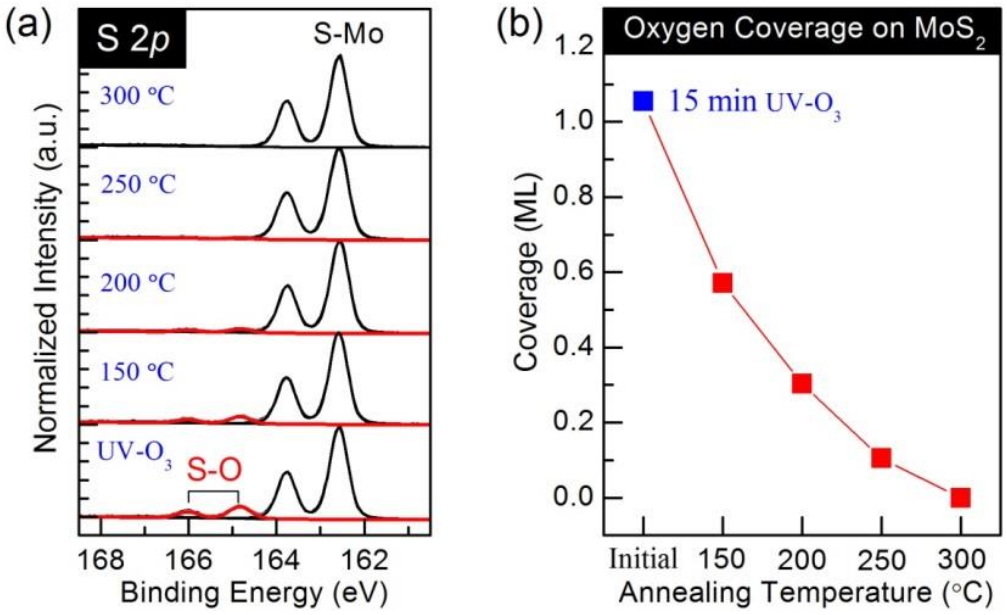

Figure 3.12 XPS spectra of the S 2p showing the thermal stability of the chemisorbed oxygen on MoS2. O-MoS_2 was annealed for 20 min under N_2 environment at ~10 mbar at the ALD chamber, without precursor exposure.

It was found that the initial S-O peak intensity from the O-functionalized MoS_2 decreased with annealing temperature. The oxygen coverage on the MoS_2 surface obtained from XPS is also presented in Figure 3.12. The oxygen coverage drop reflects the limited thermal stability of the covalent S-O bond at temperatures at which the ALD process is carried out. Therefore, desorption of oxygen from the surface can be translated as a depletion of nucleation sites for the subsequent ALD processing, resulting in less uniform films when increasing the deposition temperature to 250 °C and 300 °C.

3.5 Atomic Layer Deposited HfO_2 on Oxygen Functionalized MoS_2

The HfO_2 deposition on the oxygen functionalization of MoS_2 was also investigated in this work. HfO_2 is a dielectric material that has been implemented in monolayer MoS_2-based FETs and it

has received great interest as it has been related to the enhancement of the electron mobility.[3] For comparative purposes, 30 cycles were employed to deposit HfO_2 and the ALD temperature was set at 200 °C based on the optimized process for Al_2O_3. For the HfO_2 growth study by in-situ XPS, the effect of the initial ALD pulse, being either H_2O or TDMA-Hf, was investigated.

As shown in Figure 3.13, the S-O bond from the UV-O_3 treated MoS_2 was removed from the surface after HfO_2 deposition, as occurred with Al_2O_3, leaving a clean HfO_2/MoS_2 interface with HfO_2 interacting with MoS_2 in a non-covalent manner. An evident difference of the thickness HfO_2 films was obtained depending on the first ALD pulse. From the attenuation of the Mo-S peak in the Mo 3*d* region, the thickness was calculated as 2.3 nm and 3.3 nm for the films that was deposited using as 1st pulse TDMA-Hf and H_2O, respectively. Figure 3.13 also shows that even when the first ALD pulse had an implication on the HfO_2 growth, the Hf-O signals overlapped for both samples, indicating that HfO_2 was chemical identical. The presence of ~1 nm deep pin-holes in the HfO_2 film deposited with TDMA-Hf as 1st pulse is consistent with the lower Hf 4*f* signal in XPS. In contrast, by using H_2O as 1st pulse, the HfO_2 film is uniform and pin-hole free, as shown in the AFM images in Figure 3.14. The high selectivity of the oxygen functionalized surface towards the reaction with the first H_2O pulse instead of the TDMA-Hf pulse could be related to the increase in hydrophilicity of this surface after UV-O_3 treatment, as reported by S. Park, *et. al.*[94] During the ALD incubation period, where the reaction of the precursors with the nucleation sites is critical for a uniform coverage, the steric hindrance of the TDMA-Hf precursor can possibly play a role in the interaction with the nucleation sites, in this case, the S-O bonds on the MoS_2 surface.

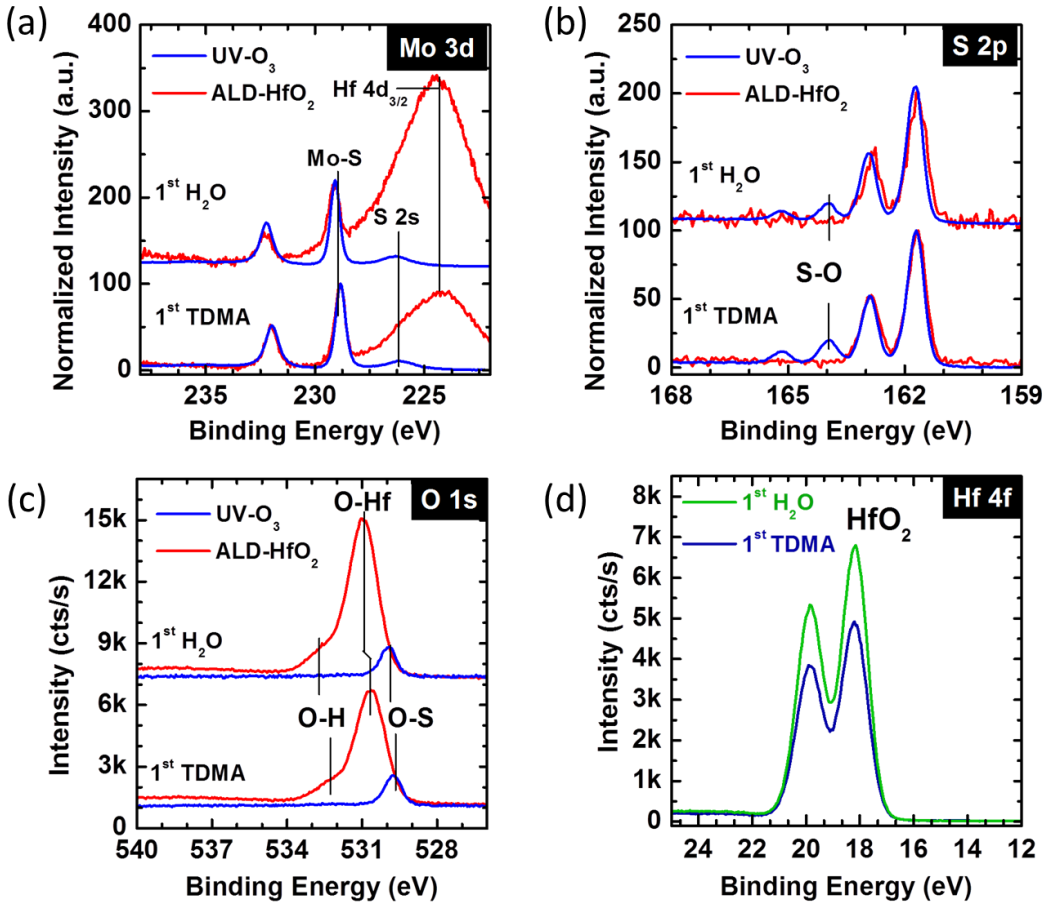

Figure 3.13. XPS spectra from MoS_2 as-exfoliated, after a 15 min UV-O_3 treatment and such surface followed by HfO_2 deposition by ALD. The effect of the 1st ALD pulse is compared: H_2O (top) and TDMA-Hf (bottom).

Using the optimized oxygen functionalization and deposition process for HfO_2 on MoS_2, top-gate FETs were fabricated and the electrical characterization was carried out by Mr. Peng Zhao and Prof. Chadwin Young at UT Dallas. This work in collaboration is contained in the manuscript entitle **"Electrical probing interface defects in the metal/HfO_2/MoS_2 gate stack"**, submitted to the journal of ACS Applied Materials and Interfaces, and presented at the International Conference on Microelectronic Test Structures (ICMTS)-2016.

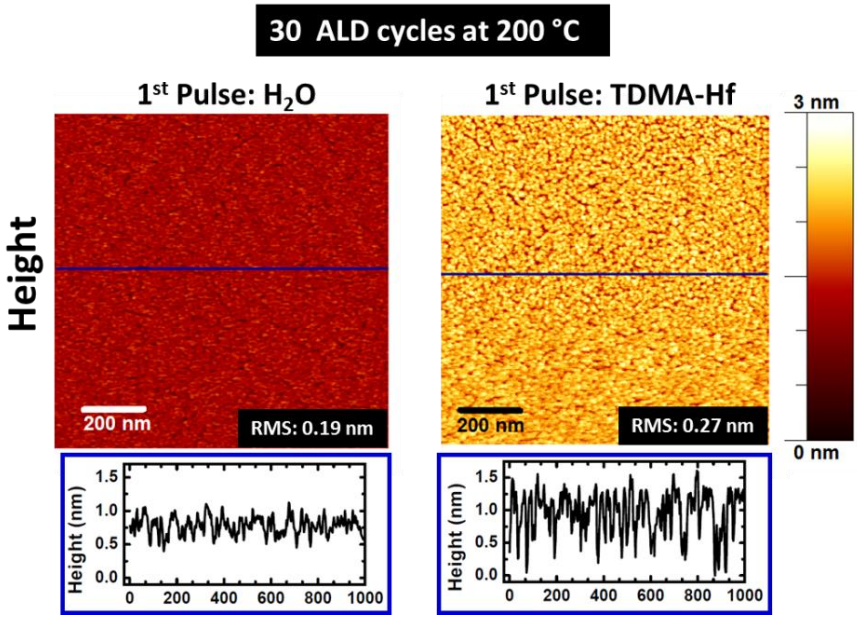

Figure 3.14. AFM surface topography and height profile of HfO_2 films deposited on O-functionalized MoS_2.

My contribution to this work was to perform the surface functionalization and HfO_2 deposition on multilayer MoS_2 and assisted in the design for the fabrication of MoS_2-FETs. The electrical characterization, analysis, and writing were carried out by Peng Zhao, and Prof. Chadwin Young. To investigate the electrical response of HfO_2 on MoS_2, a top-gate MoS_2 FETs was fabricated and the device structure is presented in Figure 3.15. For this device, MoS_2 was mechanically exfoliated onto a 270 nm SiO_2/ highly doped p-type Si substrate. Then, the multilayer MoS_2 flake was optically identified. Later, the areas for the source and drain contacts were patterned by conventional photolithography followed by deposition of 380 nm Au/20 nm Ti by e-beam deposition. The sample was then loaded into the UHV system for UV-O_3 treatment of MoS_2, followed by HfO_2 deposition at 200 °C. After high-κ deposition, Au/Ti was deposited for the top gate contact.

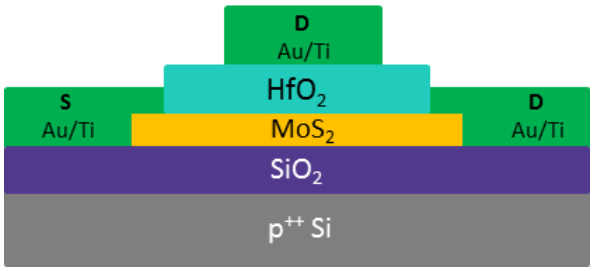

Figure 3.15. The device structure of the top-gate multilayer MoS_2-based FET.

The cross-sectional TEM imaging (not shown) confirmed 7 layers for the MoS_2 flake thickness and a thickness of 13 nm for HfO_2. Electrical measurements were carried out using a Keithley 4200 Semiconductor Characterization System and an Agilent E4980A LCR meter. The I_{DS}-V_G characteristics for this device show a high I_{ON}/I_{OFF} ratio of ~10^6, whereas the gate leakage current was at the level of 10^{-14} A, which reflects good insulating properties of the HfO_2 gate oxide. The threshold voltage V_T for this device occurred at -3V possibly related to the fixed charges in the HfO_2 film. The I_{DS}-V_{DS} characteristics for a V_{GS} sweep from -4 V to 0 V are also presented in Figure 3.16. A non-linear region was found at low V_{DS}, likely because of high contact resistance caused by the Schottky barriers at the source/drain contacts. The electronic properties at HfO_2/MoS_2 interface were investigated by capacitance measurements, having the source and drain connected to the positive electrode, and the gate to the negative electrode. The resulting C-V curve exhibits an accumulation capacitance is 0.76μF/cm^2. Knowing that the gate oxide thickness was 13 nm, a dielectric constant value of κ=11.2 is obtained. This device did not receive post-deposition annealing, which is expected to improve the HfO_2 quality by passivation of oxygen vacancies, increasing the κ value. Additionally, the presence of a frequency dependent hump in the depletion region of the C-V curve is indicative of interface trap charges at the high-

κ/MoS_2 interface. A plateau region at which the interface defects will only respond to DC bias was identified at 500 kHz.

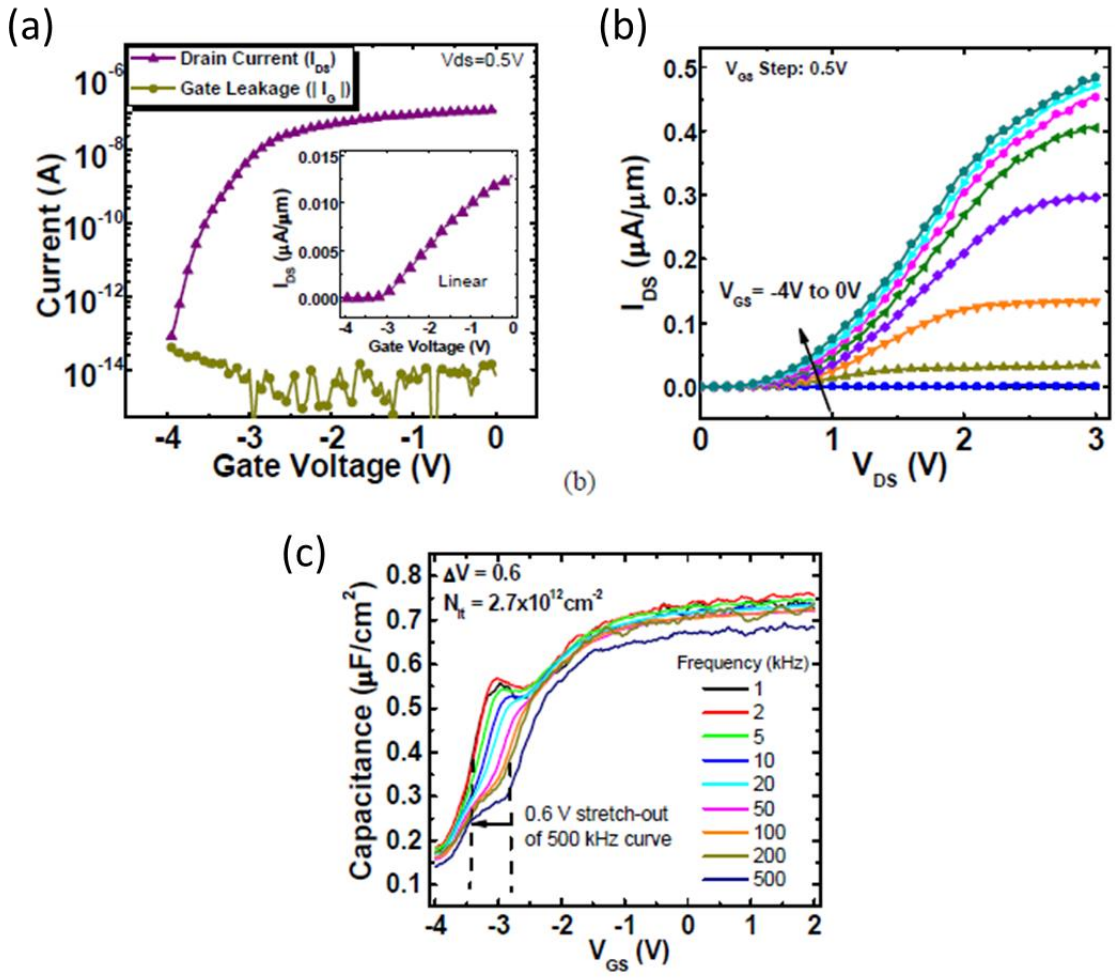

Figure 3.16. Electrical characterization of a top-gate multilayer MoS_2-based FET, having a 13 nm HfO_2 as gate oxide. a) I_{DS} - V_{GS} characteristics at V_{DS}= 0.5 V and gate leakage current $I_{G,}$. (b) I_{DS} – V_{DS} characteristics for V_{GS}= -4 V to 0 V, and (c) C-V: frequency dependence for frequencies in the range of 1 kHz-500kHz.

Therefore, the total interface trap density (D_{it}) was estimated from the oxide capacitance and the width of the plateau region at 500 kHz, which corresponds to -0.6 V as shown in Figure 3.16, resulting in a D_{it} value of 2.7×10^{12} cm^{-2}. These results suggest that multilayer MoS_2 FETs with

low leakage current and high I_{ON}/I_{OFF} ratio were realized by the implementation of the surface functionalization and dielectric deposition processes developed in this work. The device performance can potentially be improved by performing post-deposition gate oxide treatments to minimize the interface trap density and to reduce the contact resistance at the source and drain terminals.

3.6 Conclusions

In summary, the surface chemistry of MoS_2 upon UV-O_3 treatment was studied. It was found that after UV-O_3 exposure, the formation of an S-O bond at the MoS_2 surface occurs without the scission of the Mo-S bond. Atomic oxygen was identified as the main reactive species in this process, and it was indispensable for S-O bond formation under the conditions employed here. DFT suggests two favorable oxygen adsorption sites (i.e., on top of sulfur or adsorption on sulfur vacancies), where the experimental evidence suggests that adsorption on sulfur is dominant, likely due to the low areal density of initial sulfur vacancy sites. In addition, the oxygen-terminated MoS_2 surface was found to be ideal for ALD since high-κ dielectric thin films can be deposited uniformly on clean MoS_2, allowing precise control of dielectric thickness. The realization of top-gate MoS_2 based-FET was achieved by the implementation of the surface functionalization technique developed in this work. The electrical characterization show promising performance and low-leakage current using HfO_2 as the gate oxide in the top-gate structure FET, and further improvement is expected with the optimization of the device fabrication processes.

CHAPTER 4

HFO_2 ON UV-O_3 TREATED TRANSITION METAL DISELENIDES

4.1 Introduction

The electronic and optoelectronic properties of MoS_2, a readily available material in nature, have been extensively studied in recent years. However, the presence of a Schottky barrier at the metal/MoS_2 interface has limited the MoS_2-based field-effect transistors (FET) performance.[35] Moving forward into the exploration of other members in the TMD library, several efforts have focused on studying 2D WSe_2, where field-effect mobility (μ_{FE}) values up to ~500 $cm^2/V{\cdot}s$ have been reported.[95] Furthermore, band-to-band tunneling properties of WSe_2 for tunnel FET applications have been demonstrated.[96] Following these efforts, $MoSe_2$ has been implemented in FETs, exhibiting a promising performance (i.e., μ_{FE} ~150-200 eV) according to recent reports.[97,98] It has been demonstrated theoretically[80] and experimentally[3,99] that the limiting effect on mobility associated with Coulomb scattering can be reduced by a having a dielectric material on the 2D channel, motivating several studies related to dielectrics on TMDs. Here, it was shown that uniform, pin-hole free and thin Al_2O_3 and HfO_2 films can be obtained by the oxygen functionalization of the MoS_2 surface prior to the ALD process. Alternative processes have been reported in order to improve the ALD high-κ nucleation on TMDs such as oxygen plasma pre-treatment,[42] the use of ozone as an oxidant precursor during ALD of Al_2O_3,[100] metal oxide and organic based-seed layers.[101,102]

However, whether the proposed processes can be directly extended to other TMDs remains an important question, since different compositions could result in the variation of surface properties. In this work, *in-situ* monochromatic XPS studies were used to characterize the effect of a UV-ozone treatment of $MoSe_2$ and WSe_2 single crystal surfaces. Also, the surface reactivity towards oxidation of these TMDs was compared and modeled by density functional theory (DFT) calculations. It was found that surface oxides formed upon UV-O_3 exposure of the diselenides surface. Additionally, XPS monitored the interfacial chemistry between ALD-HfO_2 and the UV-O_3 treated TMD surfaces. Finally, the HfO_2 film uniformity on the UV-O_3 treated TMDs was investigated and correlated with the interfacial chemistry.

This chapter includes the material adapted with permission from a publication entitled **"HfO_2 on UV–O_3 Exposed Transition Metal Dichalcogenides: Interfacial Reactions Study"** [*2D Mater*. 2015, 2, 14004] Copyright 2015, IOP Publishing Ltd. (https://creativecommons.org/licenses/by/3.0/). The authors are A. Azcatl, S. KC, X. Peng, N.Lu, S. McDonnell, X. Qin, F. de Dios, R. Addou, J. Kim, M. J. Kim, K. Cho, and R. M. Wallace. My contribution was in planning, executing and analyzing the XPS, and AFM characterization, and writing the manuscript. The theoretical calculations by first principles density functional theory were performed by S. K. C. and K. Cho, and X. Peng, F. de Dios, N. Lu, and M. J. Kim provided the TEM characterization. S. McDonnell, X. Qin and R. M. Wallace are acknowledged for the valuable input in guiding the experiments and manuscript writing.

4.2 Experimental Details

The UV-O_3 treatments and ALD studies described here were performed *in-situ* in the UHV cluster tool. XPS was carried out using a monochromated Al Kα X-ray source (hν =1486.7 eV),

using a 15 eV pass energy. The XPS peak deconvolution was achieved with the software Aanalyzer, using Voigt functions with independent control of the Lorentzian and Gaussian components, and applying a dynamic Shirley background subtraction. The top-most layers from MoS_2 (SPI Supplies), $MoSe_2$ (2D Materials) and WSe_2 (Nanoscience Instruments, Inc) bulk crystals (all (0001) orientation) were mechanically exfoliated using Scotch® Magic™ tape, and the freshly as-exfoliated bulk materials were loaded immediately into UHV. All the UV-O_3 exposures were performed at room temperature. In an interconnected chamber, the sample surfaces are placed within a few mm from a UV lamp (low-pressure mercury lamp) in the presence of O_2 (O_2 partial pressure P_{O_2} = 900 mbar) to generate ozone, as described in Chapter 3. The ALD experiments were performed using a Picosun ALD reactor, with an operating pressure of ~10 mbar. For the HfO_2 deposition, TDMA-Hf and H_2O were used as the precursors for ALD, having a substrate deposition temperature of 200 °C. The precursor pulse and purge times are 0.1 and 4 s, respectively. High purity (99.999%) N_2 was used as the precursor carrier and purging gas. After 1 full-cycle of TDMA-Hf and H_2O, the samples were taken out from the ALD reactor and transported to the XPS analysis chamber through a transfer tube under UHV (~$1x10^{-10}$ mbar). After analysis, the samples were transported back to the ALD reactor for further deposition. This process was repeated for subsequent depositions for a total of 30 ALD cycles. Tapping-mode atomic force microscopy (AFM) images were obtained *ex-situ* using an Atomic Probe Microscope Veeco, Model 3100 Dimension V. High angle annular dark field (HAADF) scanning transmission electron microscopy (STEM) was performed using a JEOL ARM200F with probe spherical aberration (Cs) corrected operated at 200 kV. TEM sample preparation was accomplished using a FIB-SEM Nova 200.

The first-principles modeling, based on DFT[73,71] with plane wave basis sets and Projector Augmented Wave (PAW) pseudopotentials[103] as implemented in the Vienna *Ab-initio* Simulation Package (VASP)[104,105] were conducted to find the energetics of oxidation of TMDs. The electronic wave functions were represented by plane wave basis with a cutoff energy of 500 eV. The exchange and correlation interactions were incorporated as a functional of the Generalized Gradient Approximation (GGA).[73,106] A 5×5 supercell of host MX_2 monolayers (M=W or Mo and X=S, Se) was used for the DFT calculations. Each model has ~16 Å vacuum to avoid interaction between replica images as a result of the periodic boundary conditions (PBC). The k point grid of 12×12×1 was adopted for Brillouin zone sampling. The energy and Hellmann-Feynman force convergence criteria chosen were 10^{-4} eV and 0.01 eV/Å, respectively.

4.3 Reactivity of Transition Metal Diselenides ($TMSe_2$) upon UV-O_3 Treatment

In order to determine whether oxygen functionalization by UV-O_3 was extendable to TMDs beyond MoS_2, a room temperature UV-O_3 treatment was performed on WSe_2 and $MoSe_2$, while MoS_2 was also used as a control sample for comparison. XPS spectra of MoS_2, $MoSe_2$, and WSe_2, after 3, 6 and 15 minutes of UV-O_3 exposure, is shown in Figure 4.1 The sequential UV-O_3 exposure on MoS_2 shows that S-O bond formation is detected after 3 minutes, and by increasing the exposure time, i.e., 6 and 15 minutes, the oxygen adsorption saturates to form 1 ML. Under these conditions, no Mo-O bond formation is detected, as previously reported. It has also been reported that UV-O_3 can cause molybdenum oxidation in MoS_2 when the exposure is much longer (60 min).[107] This implies that the oxidation process is dose and time dependent.

In the case of $MoSe_2$, the 3 min UV-O_3 exposure initially results in the formation of Se-O bonding, without causing Mo oxidation. The nature of the Se-O results analogous to the S-O observed in MoS_2, which may be described as chemisorbed oxygen on the surface, i.e., covalent bond formation between oxygen and the top most selenium layer while preserving the covalent bonding within the $MoSe_2$ layer.

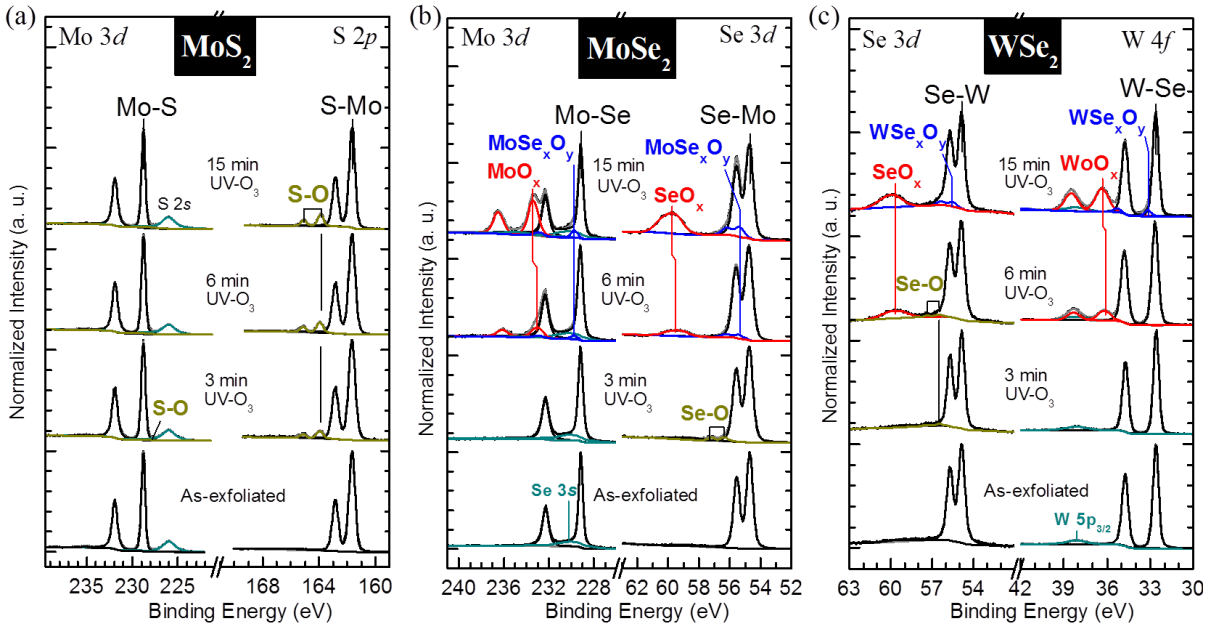

Figure 4.1. XPS spectra of the as-exfoliated (a) MoS_2, (b) $MoSe_2$ and (c) WSe_2 surfaces and after 3 min, 6 min and 15 min of UV-O_3 exposure.

However, in contrast to MoS_2, the 6 minutes UV-ozone exposure results in sub-stoichiometric molybdenum oxide (MoO_x) formation. The MoO_x peak shows a symmetric lineshape, suggesting that Mo is present in only one of the seven different phases that has been identified for MoO_x, x=2.75-3.[108,109] In the Se 3*d* region, the previously observed Se-O bond is below the detection limit, however, a new peak at ~59 eV indicates that selenium is further oxidized forming a

selenium sub-oxide SeO_x. In addition, an extra feature at ~0.6 eV higher in binding energy than the bulk $MoSe_2$ peak is observed in both Mo 3*d* and Se 3*d* core levels (blue peak in Figure 4.1). Previous studies in MoS_2 correlated the appearance of peaks at higher BE from the main bulk peak, for both Mo 3*d* and S 2*p*, with the existence of molybdenum oxysulphide (MoS_xO_y),[110,84,83] where the BE position of such peaks was dependent on the x and y values. A peak at a slightly higher BE (~ 0.5-0.8 eV) than the characteristic $MoSe_2$ peak in Se 3*d* could be also correlated with metallic Se,[111] however, the fact that both core levels showed this high BE feature makes this chemical state assignment less probable. Another possible assignment could be a sub-stoichiometric $MoSe_x$ phase, however, the existence of $MoSe_x$ would cause the transition metal peak to shift lower in BE and the chalcogen peak to broaden,[112] and this situation is not observed. Thus, the feature in blue in Figure 4.1 is associated with $MoSe_xO_y$ formation, caused by oxidation during UV-O_3 exposure. Finally, after UV-O_3 for 15 minutes, the MoO_x peak shifted to 0.4 eV higher BE which is consistent with a higher oxygen content in MoO_x.[108, 113]. Also, the MoO_x oxide to bulk peak intensity ratio increases in comparison to the 6 min ratio, showing that the oxygen is inserted deeper into the material. In the case of Se 3*d*, the sub-stoichiometric SeO_x shows a shift to 0.4 eV higher BE, suggesting complete oxidation to SeO_2.

In comparison, the XPS spectra of WSe_2 after UV-O_3 exposure for 3 and 6 minutes, the Se-O bond is detected. However the Se-O to bulk WSe_2 peak intensity ratio is lower than that for $MoSe_2$, and W oxidation in the form of WO_x is detected after 6 minutes of exposure. Similar to $MoSe_2$, the UV-O_3 exposure of WSe_2 presents tungsten oxyselenide bonding (WSe_xO_y) after 15 min of exposure, in addition to WO_x and SeO_x formation. Table 4.1 summarizes the bonds

formed after UV-O_3, showing their binding energy and ratios of the integrated intensity of the corresponding peaks with respect to the bulk signal.

Table 4.1. Chemical species detected on MoS_2, $MoSe_2$, and WSe_2 after UV-O_3 exposure, showing the corresponding peak positions in eV. The integrated intensity ratio with respect to the bulk peak is shown in brackets"[ ]".

UV-O_3 Treatment Time		3 min	6 min		15 min	
MoS_2	S 2p	**S-O** 162.9 [0.06]	**S-O** 162.9 [0.1]		**S-O** 162.9 [0.1]	
	Mo 3d	---	---		---	
$MoSe_2$	Se 3d	**Se-O** 56.3 [0.04]	**$MoSe_xO_y$** 55.4 [0.05]	**SeO_x** 59.1 [0.10]	**$MoSe_xO_y$** 55.4 [0.12)	**SeO_x** 59.5 [0.34]
	Mo 3d	---	**$MoSe_xO_y$** 229.8 [0.05]	**MoO_x** 233.0 [0.22]	**$MoSe_xO_y$** 229.7 [0.10]	**MoO_x** 233.4 [0.79]
WSe_2	Se 3d	**Se-O** 56.5 [0.02]	**Se-O** 56.5 [0.02]	**SeO_x** 59.3 [0.14]	**WSe_xO_y** 55.4 [0.07]	**SeO_x** 59.6 [0.22]
	W4f	---	**WO_x** 36.1 [0.18]		**WSe_xO_y** 33.1 [0.06]	**WO_x** 36.3 [0.45]

Oxidation studies of these TMDs in the bulk form were performed previously by Jaegermann *et al.*,[114] where reactivity towards oxidation was found to go from lower to higher in the sequence: $MoS_2 < MoSe_2 < WSe_2$. This tendency was related to the degree of mixed metal d-states from the transition metal with the p-states in the chalcogenide, based on ionization energies arguments. However, in that study, the oxidation process was performed in solution by a photoelectrochemical method using electrolytes (i.e., K_2SO_4), which might have introduced additional variables in the oxidation processes. To have a better understanding of the difference in reactivity during the oxidation process in these TMDs, DFT calculations were performed.

The calculated formation energies of the oxygen adsorption and chalcogen substitution by oxygen are listed in Table 4.2, were equation (4.1) was employed:

$$E^{form} = E(O{:}MX_2) - E(Pristine) - n\mu_0 - n\mu_S \quad (4.1)$$

where E^{form} is the formation energy of the adsorbed or substitutional oxygen on MX_2 surfaces with total DFT energy *E (O:MX₂), E (Pristine)* is the DFT energy of the pristine MX_2 surfaces ((M=W or Mo and X=S, Se), μ_0 and μ_S are the reference chemical potentials of O (oxygen molecule) and S (bulk sulfur) and *n* is the number of adsorption or substitutional O atoms. Under this definition, negative values of the formation energy refer to thermodynamically stable oxidation process. Figure 4.2 shows optimized structures for MoS_2, $MoSe_2$, and WSe_2, respectively, when an oxygen atom is adsorbed on top of the chalcogen (O-Se, O-S) and when oxygen substituted the chalcogen to form a transition metal-oxygen bond (O-Mo, O-W).

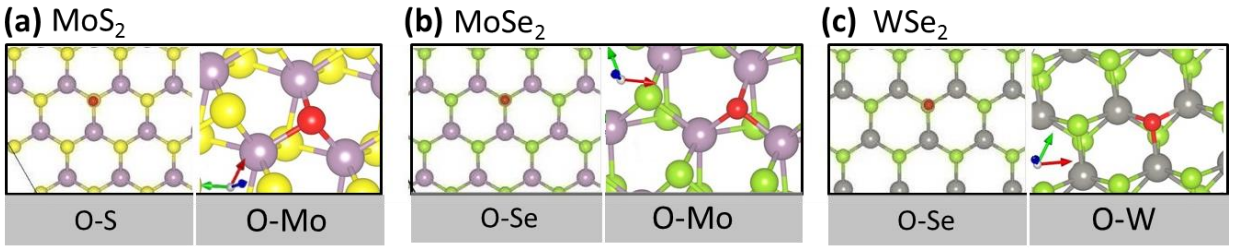

Figure 4.2. Optimized (a) MoS_2, (b) $MoSe_2$ and (c) WSe_2 structures after oxygen adsorption on top of the chalcogen atom (top view) and after replacement of the chalcogen atom with an oxygen atom (tilted top view).

According to the formation energies shown in Table 4.2, O-S bond in MoS_2 is more energetically favorable and therefore more stable in comparison to O-Se in $MoSe_2$ and WSe_2. The DFT calculations also indicate that oxygen desorption will occur more easily in $MoSe_2$ and WSe_2, in comparison to MoS_2. The formation energy required for the replacement of the chalcogen to

form a direct bond between oxygen and the transition metal is found to be more energetically favorable in the case of $MoSe_2$ and WSe_2 than for MoS_2, which is consistent with the XPS results after UV-O_3 exposure.

The relative lower stability of the O-Se bond in comparison to O-S implies that desorption of oxygen, and possibly the "kick-out"[115] of O-Se species, can leave unsaturated bonds for the transition metal, which then are readily available to form Mo-O and W-O bonds in presence of oxygen, such as during a UV-O_3 exposure.

Table 4.2. Formation energies of oxygen adsorption (E_f^{ad}) and oxygen replacement (E_f^{rep}) on MoS_2, $MoSe_2$, and WSe_2 calculated by DFT.

	E_f^{ad} (eV)	E_f^{rep} (eV)
MoS_2	O-S -1.12	O-Mo -1.912
$MoSe_2$	O-Se -0.284	O-Mo -2.504
WSe_2	O-Se -0.132	O-W -2.814

Experimentally, this oxidation process caused the formation surface oxides of 0.36 nm and 1 nm thickness in $MoSe_2$ for 6 min and 15 min of UV-O_3 exposure respectively, while the surface oxides in WSe_2 exhibited 0.33 nm and 0.66 nm thicknesses for the same mentioned exposure times, according to XPS thickness calculations.

4.4 Interface Chemistry of HfO_2 on UV-O_3 Treated $TMSe_2$

These UV-O_3 exposure studies demonstrate that the controlled oxygen functionalization of the outermost layers is more challenging for $MoSe_2$ and WSe_2 than for MoS_2. Yet, the impact of having surface oxides on these TMDs prior to high-κ dielectric deposition by ALD is still of interest. Thus, HfO_2 was sequentially deposited by ALD on the UV-O_3 treated $MoSe_2$ and WSe_2, while the interface chemistry was monitored by XPS. For comparison purposes, all the samples discussed here received a UV-O_3 exposure for 6 minutes.

Figure 4.3 shows that after one ALD cycle on the UV-O_3 exposed $MoSe_2$, the MoO_x peak intensity significantly decreases to ~24% its initial intensity. In Mo 3*d*, a new peak is detected at 231.9 eV, which is designated as Mo^{5+},[116] indicating that the Mo-O bonds are reduced (i.e., O was transferred to Hf, resulting in a lower oxidation state of Mo). Additionally, the SeO_x intensity decreases to below the detection limit, as shown in the Se 3*d* region. The decrease in oxide intensity during to precursor pulsing in ALD or "self-cleaning" effect was previously observed for III-V materials, such as GaAs.[92] The self-cleaning reduction reactions that occurred after one cycle involved the gradual reduction of the oxidation state from Mo^{6+} to Mo^{5+}. In addition, the fact that no Mo^0 or other chemical state was detected suggests that MoO_x went through a ligand exchange reaction with the Hf precursor, forming a volatile molybdenum compound possibly of the form $Mo(N(CH_3)_2)_x$.[117] Based on the thermodynamic quantities, HfO_2, with a Gibbs free-energy of formation of -251.8 kcal/mol,[118] results in a more energetically favorable reaction product than MoO_x, assuming that the Gibbs free-energy of MoO_x is close to -159.65 kcal/mol,[119] which is the corresponding value for MoO_3.

For the Se 3*d* feature, no lower oxidation states are detected (i.e., S^0), indicating that SeO_x, a volatile compound, is possibly thermally desorbed from the surface in the vapor phase.[120] Finally, the $MoSe_xO_y$ peak is not observed after one cycle, suggesting that the $MoSe_xO_y$ phase possibly recovers its initial state as $MoSe_2$ through the SeO_x desorption channel, thus contributing to the bulk Se peak signal intensity.

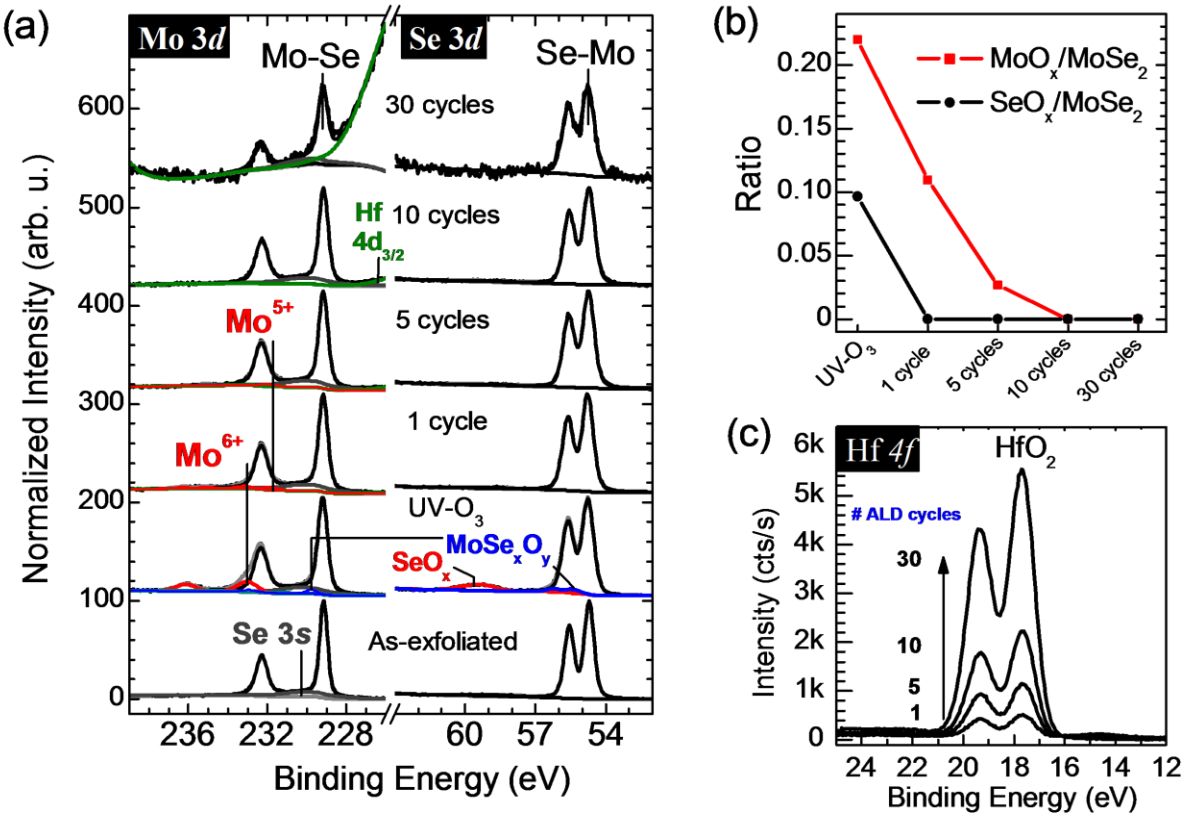

Figure 4.3. In-situ XPS spectra for $MoSe_2$ as-exfoliated, after 6 min of UV-O_3 exposure and after sequential HfO_2 depositions by ALD. b) The MoO_x and SeO_x to $MoSe_2$ ratio obtained from their respective integrated intensities. (c) Hf 4f spectra after 1, 5, 10 and 30 ALD cycles on UV-O_3 treated $MoSe_2$.

Further deposition of HfO_2 using five ALD cycles results in a decrease of the Mo^{6+} intensity to below the detection limit; only Mo^{5+} remains. As shown in Figure 4.3, the Mo^{5+} to $MoSe_2$

integrated intensity ratio is ~0.03, suggesting that most of the surface oxides undergo "self-cleaning" reactions. The Se 3*d* spectra show no change after five cycles. After ten cycles, no interfacial oxides from $MoSe_2$ are detected, and further HfO_2 deposition only caused attenuation of the $MoSe_2$ features. It should be noted that the chemical identity of HfO_2 remains constant throughout the sequential depositions.

In an analogous process, HfO_2 was sequentially deposited on UV-O_3 treated WSe_2 followed by XPS analysis. Figure 4.4 shows the evolution of WSe_2 chemical states through the experiment. It is shown that in contrast to $MoSe_2$, the decrease in intensity of the transition metal oxide in WSe_2 is minimal after the first cycle. In fact, the WO_x to bulk intensity ratio remains constant, however, the Se-O intensity decreases below the detection limit, and the SeO_x to WSe_2 ratio decreases by ~44%. Even when the formation of HfO_2 is more energetically favorable than WO_x based on the Gibbs free energy (WO_3 ≈ -195.7kcal/mol),[119] WO_x remains on the WSe_2 surface, exhibiting lower reactivity during the ALD "self-cleaning" reduction reactions in comparison to MoO_x. Various hypotheses can be made to explain the limited HfO_2 growth. First, assuming a ligand exchange mechanism as in the case of $MoSe_2$, then dissociation of W-O bond would be needed. The dissociation energy of the W-O bond is 720±71 kJ/mol,[121] which is much higher than the Mo-O dissociation energy 597.2±33.5 kJ/mol[121] thus the oxygen loss in WO_x and subsequent formation of a volatile $W(N(CH_3)_x)$ compound requires a higher energy than MoO_x. Secondly, WO_3 and MoO_3 clusters are well known for their catalytic properties toward oxidation, where it was found that Mo^{6+} will be more easily reduced to Mo^{5+} than W^{6+} to W^{5+} due to the high stability of WO_3.[122]

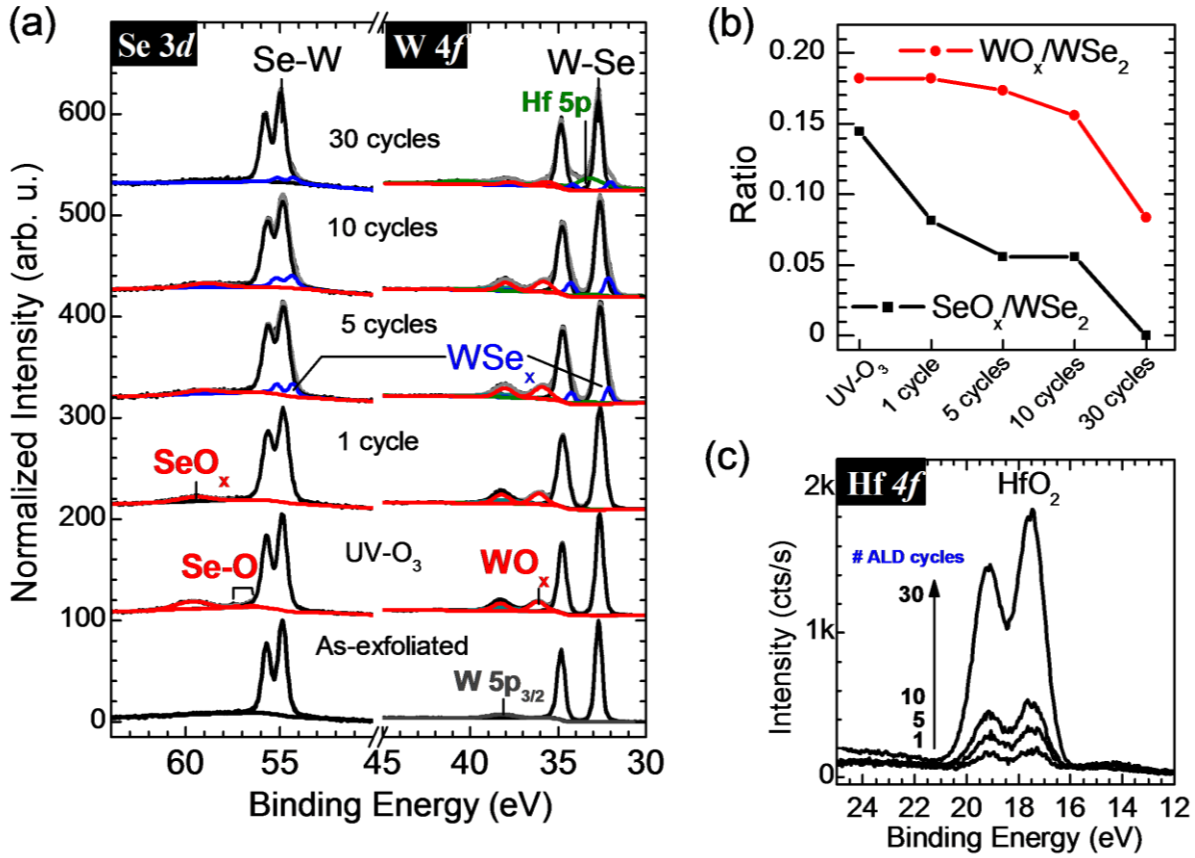

Figure 4.4. In-situ XPS spectra for WSe_2 as-exfoliated, after 6 min of UV-O_3 exposure and after sequential HfO_2 depositions by ALD. b) The WO_x and SeO_x to WSe_2 ratio obtained from their respective integrated intensities. (c) Hf 4f spectra after 1, 5, 10 and 30 ALD cycles on UV-O_3 treated WSe_2.

This is consistent with our observation in MoO_x and WO_x reactivity after one ALD cycle. The capability of WO_x to remain in the W^{6+} oxidation state makes WO_x an effective oxidizing agent of organic molecules.[83] Thus, another possible scenario is the reaction between WO_x and the organic ligand in TDMA-Hf inhibiting ligand exchange reactions. In fact, the sequential depositions of HfO_2 result in the presence of additional carbon features in WSe_2, such as C-O bonds, as shown in Figure 4.5. These carbons species were detected starting from the first ALD cycle and they likely arise from the by-products of the ALD reactions. In contrast, the carbon

species detected for $MoSe_2$ upon HfO_2 deposition were mainly of C-C type, and are reduced in intensity with increasing ALD cycles.

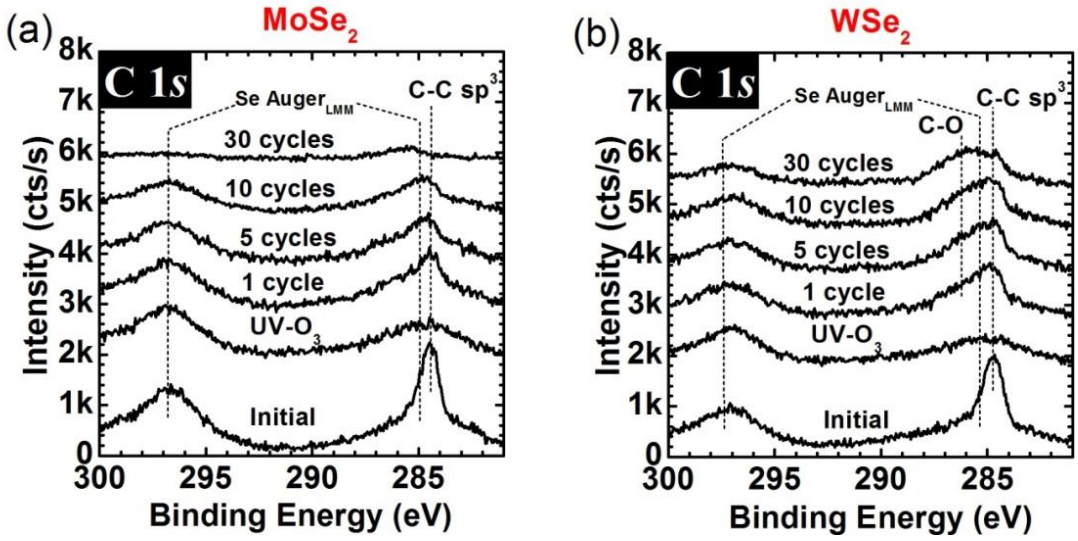

Figure 4.5. C 1*s* XPS spectra of the as-exfoliated and UV-O_3 exposed (a) $MoSe_2$ and (b) WSe_2 surfaces, and the spectra evolution upon the sequential HfO_2 deposition by ALD. Auger $_{LMM}$ features from selenium span the C 1*s* energy window.

After five cycles, the WO_x to WSe_2 peak ratio decreases by only 5% along with a WO_x peak shift to a lower BE of ~0.2 eV, while the SO_x to WSe_2 peak ratio decreases by 31% from its previous value. Interestingly, extra features at identical lower BE positions from the bulk WSe_2 signals, for both W 4*f* and Se 3*d* are detected. The appearance of low BE peaks in WSe_2 was previously reported and attributed to a non-van der Waals surfaces[123] characterized by edge planes and stepped surfaces. Such non-homogeneous surface potential can give rise to different Fermi level positioning, shifting the core levels in WSe_2 the same amount. Thus, these newly identified peaks can be identified as WSe_2 with a different Fermi level in reference to the initial WSe_2. A non-van der Waals surface could be generated from desorption of surface oxides leaving regions

in WSe_2 with unsaturated bonds and/or partially etched areas. After 30 ALD cycles, the SeO_x is below the detection limit, and the WO_x to WSe_2 peak intensity ratio decreases to a value of 0.08, with a final BE position ~0.53 eV lower than the initial WO_x BE, due to lower oxygen content in WO_x.[124] This indicates that lower oxygen content in WO_x improves the rate of ligand exchange reactions between WO_x and TDMA-Hf. It should also be noted that the Hf 4*f* integrated intensity is significantly different on $MoSe_2$ and WSe_2 for the same number of cycles as shown in Figure 4.6, where the final HfO_2 content on $MoSe_2$ is about three times that detected on WSe_2, suggesting differences in HfO_2 coverage.

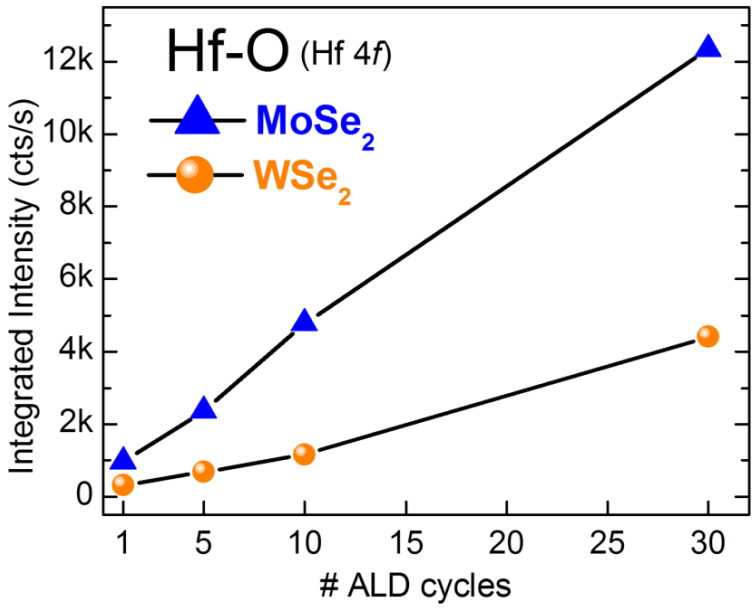

Figure 4.6. HfO_2 integrated intensity obtained in the Hf 4*f* spectra with number of ALD cycles on UV-O_3 exposed $MoSe_2$ and WSe_2.

4.5 Interface Chemistry-Structure Correlation for the $HfO_2/TMSe_2$ Stack

The surface topography of the HfO_2 films on the UV-O_3 exposed TMDs was investigated and the corresponding ex-situ atomic force microscopy images are presented in Figure 4.7.

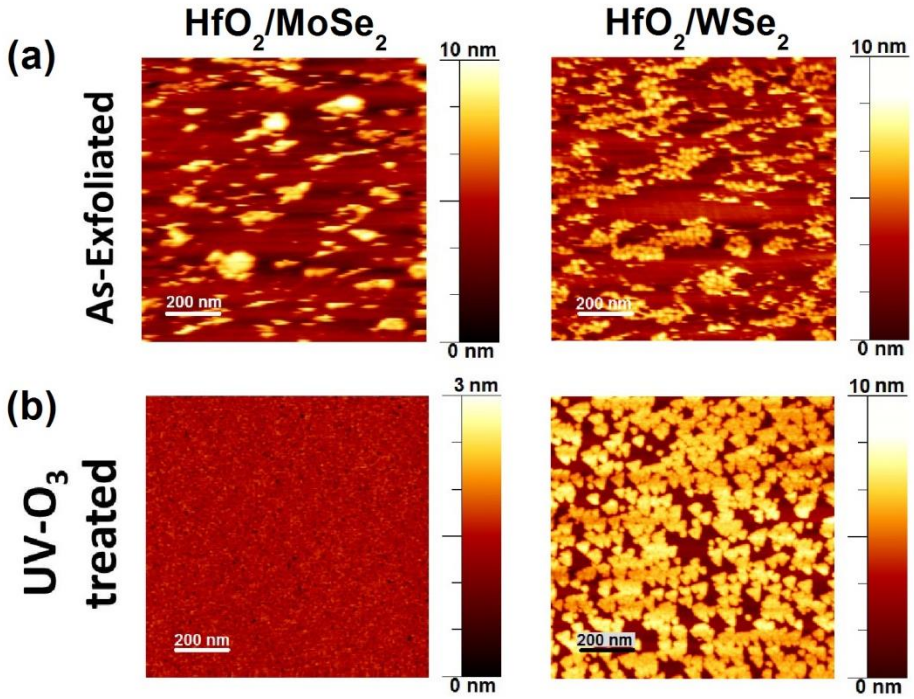

Figure 4.7. 1 μm x 1 μm AFM images of HfO_2 on (a) as-exfoliated and (b) UV-O_3 treated $MoSe_2$ and WSe_2.

For comparison, HfO_2 was deposited (30 cycles of TDMA-Hf and H_2O) on as-exfoliated non-treated samples, where the dearth of reactive sites on the $MoSe_2$ and WSe_2 surfaces impeded uniform ALD nucleation, thus HfO_2 is deposited following an island-type growth mechanism, as observed on MoS_2. In contrast, on the UV-O_3 treated $MoSe_2$, the HfO_2 film is fully covered and pin-hole free. Therefore, the presence of surface oxides formed after UV-O_3 enhanced HfO_2 growth rate in comparison to non-treated $MoSe_2$, leaving a completely covered HfO_2 film as a result with an RMS roughness of only 0.15 nm. Interestingly, on the UV-O_3 treated WSe_2, HfO_2 islands with a triangular shape are formed with edge length and height in the range of 30-60 nm and 4-5 nm, respectively. It has been shown that triangular hole-like structures can be generated on WSe_2 by oxidative electrochemical etching promoted by AFM[125,126] and STM[127] tip-sample

voltage. In this case, the presence of triangular hole-like structures on WSe_2 could have served as the nucleation site for HfO_2, resulting in a quasi-ordered triangular cluster growth. This implies that oxidative etching of WSe_2 could have taken place during UV-O_3 exposure for 6 minutes and/or ALD self-cleaning reactions. In fact, the last hypothesis correlates with the newly detected WSe_2 XPS peaks (blue features in Figure 4.1) and in turn with the formation of a non-van der Waals surface, as discussed previously.

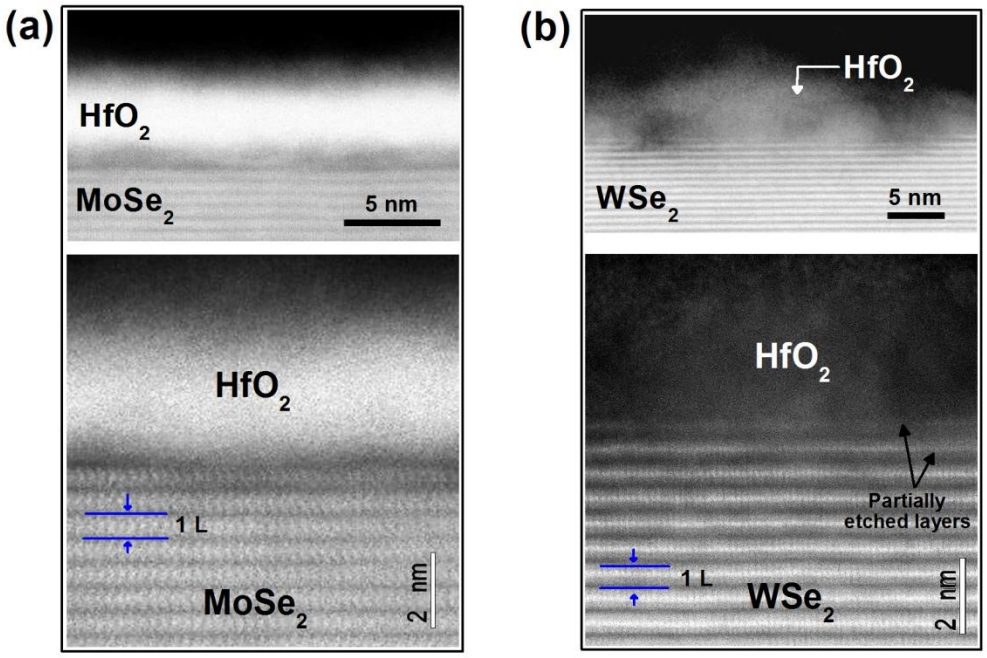

Figure 4.8. STEM micrographs of (a) HfO_2 on UV-O_3 treated $MoSe_2$ and (b) HfO_2 on UV-O_3 treated WSe_2.

In accordance with the AFM results, cross-section STEM images in Figure 4.8 shows a uniform HfO_2 film with thickness of ~4 nm on UV-O_3 treated $MoSe_2$, having a minimal variation in thickness across a length of 0.25μm Interestingly, the top-most $MoSe_2$ surface exhibits darker contrast regions that correspond to selenium-deficient $MoSe_2$ according to electron energy loss

spectroscopy (EELS) line scans across the HfO_2-$MoSe_2$ interface. The ALD self-cleaning reactions occurred right at the $MoSe_2$ surface are likely to be involved in the generation of such selenium-deficient regions. It is also evident that the $MoSe_2$ layers below the darker contrast region are continuous and unaltered.

Finally, the high magnification STEM image provides further information about the structure at the HfO_2 /WSe_2 interface. Figure 4.8 shows that partially etched WSe_2 layers are identified at the interface, which correlates with the XPS and AFM results described above. Here, the contrast of the partially etched WSe_2 layers is weaker at the HfO_2/WSe_2 interface than it is in the bulk WSe_2. This can be explained by considering that a STEM image is averaging cross-sectional information from a finite ~ 100 nm thick material. Since the triangular hole-like structures observed in this work have an area smaller than the thickness analyzed in cross-section by STEM, their presence could only be observed in STEM as a weakening of the contrast, while some signal from the un-etched portions of that same layer will always be obtained. Clearly, various mechanisms are involved in the HfO_2 growth on UV-O_3 treated WSe_2. First, the presence of WO_x on the WSe_2 surface and its relatively high stability during self-cleaning reactions slows down the HfO_2 growth rate in comparison to $MoSe_2$ for the same number of cycles, generating a partially covered HfO_2 film. Secondly, the presence of triangular hole-like structures on WSe_2 generated by etching caused the preferential HfO_2 nucleation on such structures, forming triangular HfO_2 islands.

4.6 Conclusions

In summary, it is found that selective oxygen functionalization of the selenium-based TMDs studied here is limited by highly energetically favorable oxidation of the transition metal. These

results highlight the importance that the TMD composition has on the reactivity towards oxidation. The investigation of the atomic layer deposition of HfO_2 on the TMDs with initial surface oxides elucidates self-cleaning reduction reactions and the desorption of volatile species during the ALD process. According to the interface study, the surface oxides on $MoSe_2$ are completely removed by the self-cleaning reduction reaction upon HfO_2 deposition. In contrast, the self-cleaning effect is less effective in the oxide removal on WSe_2 mainly due to the relative stability that WO_x exhibits. Thus, the ability to assist the HfO_2 nucleation is superior for MoO_x than WO_x. Finally, the coverage of HfO_2 on the TMDs surfaces was improved by the UV-O_3 pre-treatment.

CHAPTER 5

DIELECTRICS ON WSE_2 BY OZONE-BASED ATOMIC LAYER DEPOSITION

5.1 Introduction

Monolayer WSe_2 is a promising channel material for 2D electronic device applications, demonstrating a hole mobility in the order of 250 $cm^2/V{\cdot}s$ when implemented in FETs.[48] Furthermore, it has been predicted that the $WSe_2/SnSe_2$ heterostructure can form a nearly broken band alignment, which is desirable for efficient interband tunneling in a thin-tunneling FET.[33] For the realization of the proposed TFET structures based on WSe_2, the integration of thin high-κ dielectric films is required. However, as presented in Chapter 4, the UV-O_3 treatment employed to functionalize the MoS_2 surface caused significant oxidation and etching of the outermost layers in WSe_2, degrading the uniformity of the dielectric films.[128] An alternative approach to deposit high-κ dielectrics on 2D TMDs consists in the use of ozone as oxidant precursor during the ALD process. Ozone-based ALD has been proven to generate thin Al_2O_3 films on graphene[129] and MoS_2.[43] Yet, it has been found that the conditions during the ALD process are critical as oxidation or etching of the 2D material can occur due to oxidant nature of the ozone precursor. In this work, the ozone-based ALD process was evaluated for the deposition Al_2O_3 and HfO_2 on WSe_2. To understand the high-κ dielectric nucleation and reactivity towards WSe_2, *in-situ* X-ray photoelectron spectroscopy characterization (XPS) was employed. Differences in the reactivity for the metal-organic precursors towards the formation of an interfacial WO_x were identified. This study helped to identify the temperature ranges at which etching of WSe_2 is avoided while a

uniform high-κ dielectric film is obtained. Finally, the energy band alignments for Al_2O_3 and HfO_2 on WSe_2 were determined.

5.2 Experimental Details

For these experiments, synthetic bulk WSe_2 purchased from 2D Semiconductors Inc. was employed. The initial surface was prepared by mechanical exfoliation of the outermost layers using Scotch® Magic™ tape. The freshly exfoliated surface was immediately loaded (within 5 min) into an ultrahigh vacuum (UHV) system. Then, the WSe_2 sample was annealed at 300 °C for 2 hours under UHV (~10^{-9} mbar) to remove the adsorbed carbon from the surface due to the short air exposure after exfoliation. After annealing, the adsorbed carbon signal in the C 1*s* XPS spectrum was below the detection limit. The annealed WSe_2 surface was then transferred *in-situ* to the ALD chamber to perform the Al_2O_3 or HfO_2 deposition by the ozone-based ALD as described in Figure 5.1. TMA was the metal-organic precursor used to deposit Al_2O_3, while TDMA-Hf was used for the HfO_2 depositions. The metal-organic precursors were introduced into the reactor with a pulse time of 0.1 sec, followed by a 4 sec Ar purge. Ozone generated from a remote source was used as the oxidant precursor with a pulse time of 0.1 sec, and a flow of ~70 sccm followed by a purge time of 10 sec to complete one cycle. In order to analyze the interface chemistry between the high-κ film and WSe_2 by XPS, all the depositions were performed using 30 ALD cycles at different temperatures. The i*n-situ* XPS characterization was carried out using a monochromated Al Kα source (hν = 1486.7 eV). The XPS spectra were acquired at a take-off angle of 45° and pass energy of 15 eV. For XPS peak analysis and deconvolution, the software *AAnalyzer* was employed, where Voigt line shapes and an active Shirley background were used for peak fitting.[66]

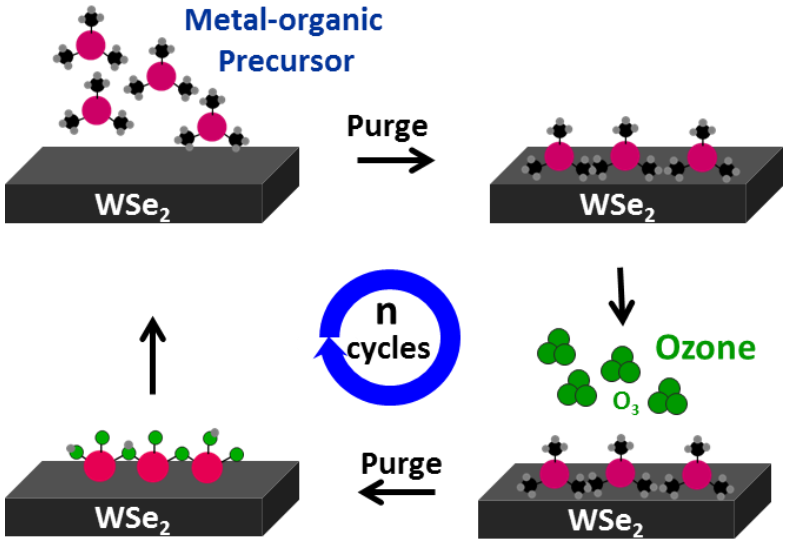

Figure 5.1. Schematic of the ozone-based ALD process on WSe_2 studied in this work. The ozone source was remotely generated and was employed as the oxidant precursor for ALD of high-κ dielectrics.

5.3 Ozone Interaction with WSe_2

Prior to the discussion of the ozone-based ALD process on WSe_2, the reactivity of ozone alone with WSe_2 is presented. For these experiments, ozone exposures were performed on WSe_2 in the ALD chamber using 30 ozone pulses of 4 sec at different temperatures. XPS was used to investigate the surface chemistry of WSe_2 after the ozone exposures, and Figure 5.2 shows the resulting XPS spectra. It was found that the ozone pulsing at 30 °C did not generate changes in the WSe_2 spectra with respect to the initial WSe_2 surface. In addition, the resulted O 1*s* signal was below detection limits. At 150 °C, a Se-O bond was formed upon the ozone exposure with at a binding energy of 56.5 eV in Se 3*d* and the corresponding oxygen signal was detected at 529.7 eV. As described previously, the Se-O bond is indicative of oxygen chemisorption on the top most selenium layer. Interestingly, tungsten oxidation was below detection limits in the W 4*f*

spectra, while a low-intensity O-W peak was detected in the O 1*s* region, suggesting an initial stage in the tungsten oxidation. For the ozone exposure at 200 °C, no signals from a Se-O bond were identified in Se 3*d* or O 1*s*. Since the Se-O bond can be formed at a lower temperature (150 °C), the absence of this species at 200 °C provides evidence that the Se-O bond is not stable at this temperature. Also, the appearance of sub-stoichiometric WSe_x peaks in W 4f and Se 3d is indicative of partial etching at the surface, as described in the previous chapter. Therefore, the XPS spectra at 200 °C suggest an initial selenium oxidation and desorption of Se-O bonds, leaving sub-stoichiometric WSe_x on the surface. The spectra for the ozone exposure at 300 °C resulted in the oxidation of WSe_2 forming tungsten oxide, where the corresponding peak at 36.2 eV in W 4*f* and stoichiometry is consistent with the oxidation state of 6+ in WO_3 according to the literature.[130] At this temperature, no selenium oxide species were detected on the surface, but the presence of WO_3 suggests that selenium should have been oxidized possibly forming a volatile product such as SeO_2.[120] In addition to the surface oxidation upon ozone exposure, the presence of WO_3 on WSe_2 generated a shift of the core levels to lower binding energies by 0.9 eV, which can be interpreted as a movement of the Fermi level towards the valence band or upward band bending. Similar Fermi level shift has been observed for the MoO_x/MoS_2 system characterized as band bending at the interface due to the differences in work function of these materials. Therefore, a similar effect is expected in the case of the WO_3/WSe_2 system. Clearly, different surface chemistry was obtained on WSe_2 upon ozone exposure as a function of temperature, having a mild oxidation at 200 °C, to a more severe oxidation of WSe_2 at 300 °C. This reactivity study results important for the understanding of the ozone-based ALD process as described in the following section.

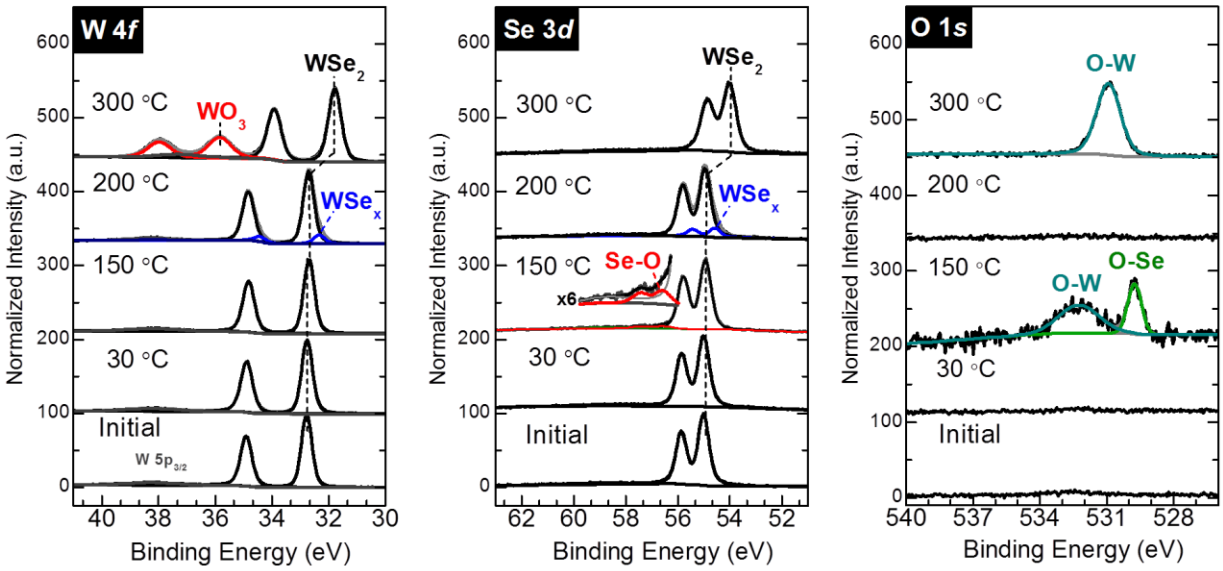

Figure 5.2. XPS spectra of WSe_2 before and after ozone exposure at different temperatures. The initial WSe_2 surface received a UHV annealing at 300 °C for one hour.

5.4 ALD Temperature Dependence on the High-κ Dielectric/WSe_2 Interface Chemistry

5.4.1 Al_2O_3 on WSe_2

A temperature dependence study was performed to investigate the effect on the growth and interface chemistry upon Al_2O_3 deposition on WSe_2 by in-situ XPS. For this purpose, the ozone-based ALD process was carried out using a fix number cycles, in this case, 30 cycles of TMA and O_3 while the deposition temperature was varied. The interface chemistry of WSe_2 after Al_2O_3 deposition is presented in Figure 5.3. It was found that for the deposition at 100 °C and 150 °C did not promote the oxidation of WSe_2, meaning that the chemical identity of WSe_2 was preserved. Additionally, there was no evidence of reactivity between WSe_2 and Al_2O_3, suggesting that the interaction between these materials is non-covalent. Increasing the deposition temperature to 200 °C caused the formation of substoichiometric WO_x ($x<3$) detected at a

binding energy of ~36.0 eV. According to the study of the ozone reactivity with WSe_2, WO_x is not expected to be generated at 200 °C. Therefore, the detected oxidation of WSe_2 is likely to be promoted during the reaction between ozone and the metal-organic precursor TMA.[131]

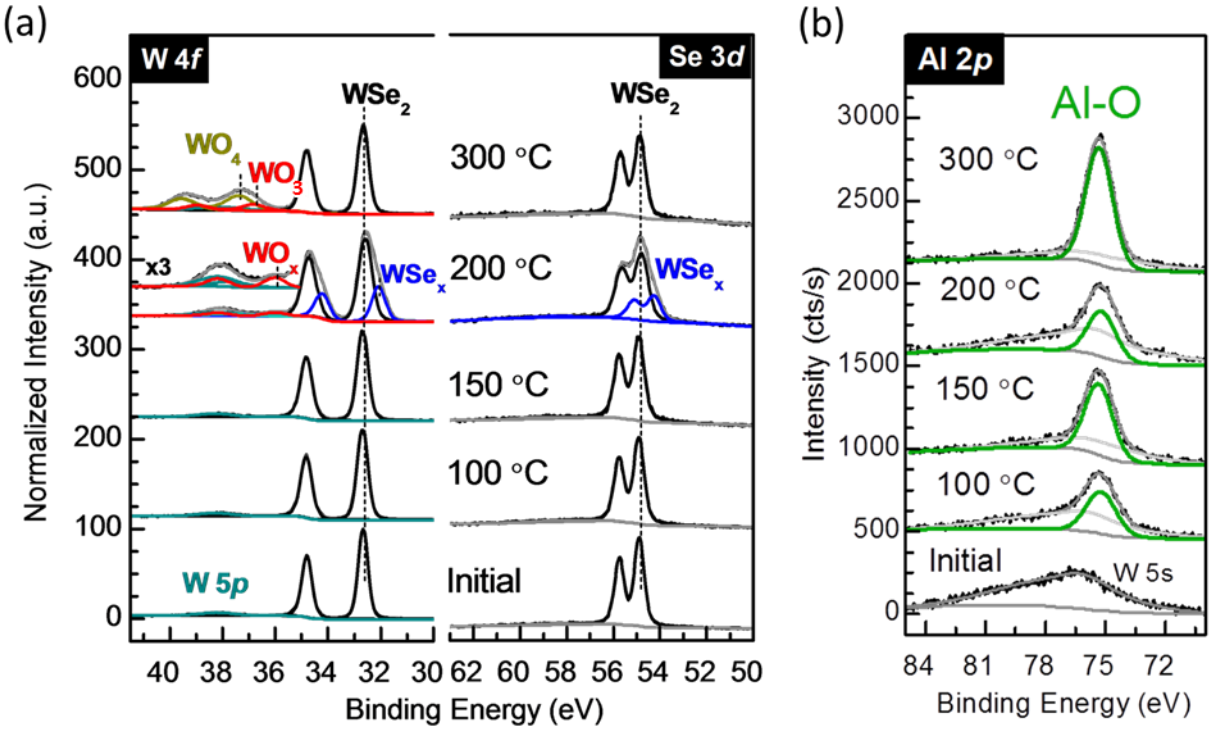

Figure 5.3. (a) W 4*f*, Se 3*d*, and (b) Al 2*p* XPS spectra of the initial WSe_2 surface and the interface chemistry upon Al_2O_3 deposition on WSe_2 by ozone-based ALD at different temperatures.

In addition to WO_x, WSe_x peaks were detected at 0.5 eV lower in binding energy that the bulk WSe_2 peak in W 4*f* and Se 3*d*, which is indicative of partial etching of the outermost WSe_2 layers as a result of non-uniform WSe_2 oxidation.[128] Interestingly, the oxidation of WSe_2 during the ALD process did not generate selenium oxide at the interface. Similarly, the Al_2O_3 deposition at 300 °C led to oxidation of WSe_2, generating WO_3 (~36.2 eV) at the interface; yet, in this case, no WSe_x peaks were detected. In addition to WO_3, a chemical state at ~36.7 eV was detected.

According to the literature, this binding energy corresponds to a tungstate compound.[132] Given the tendency of WO_3 to react with Al_2O_3 to form $Al_2(WO_4)_3$, this compound is possibly present at the interface.[133] Based on these results, it was found that in order to avoid interfacial reactions and subsequent WSe_2 oxidation, the deposition temperatures for Al_2O_3 on WSe_2 can be performed at 150 °C or below. The corresponding Al-O peak for all the studied temperatures shows a single chemical state. Here it should be noted that in the W 5s peak spans the Al 2p region, and careful peak fitting was required to subtract the contribution of this peak to the Al 2p signal from the Al-O bond. The deposition temperature effect on the Al_2O_3 coverage is later discussed.

5.4.2 HfO_2 on WSe_2

Similarly, the ozone-based ALD process for the deposition of HfO_2 on WSe_2 was investigated by in-situ XPS. For comparison purposes, 30 cycles were also employed in the deposition of HfO_2, at different temperatures using TDMA-Hf and ozone as precursors. In this case, the temperature of 100 °C was not tested to avoid condensation of the low-vapor pressure TDMA-Hf precursor. Figure 5.4 shows the interface chemistry for the HfO_2/WSe_2 interface. Analogous to Al_2O_3, the deposition at 150 °C did not generate an oxide interlayer (IL) on WSe_2, and only the peaks corresponding to WSe_2 were detected. However, the interfacial chemistry at 200 °C differs to that generated for Al_2O_3. In the case of HfO_2, there were no detectable WO_x or WSe_x species that could indicate partial etching of WSe_2. This result highlights the difference in reactivity that TMA and TDMA-Hf exhibit towards oxidation of the substrate during the ozone based ALD process. Such differences and the resulting lack of oxidation at 200 °C for HfO_2 could be related to the relative higher steric hindrance of the TDMA-Hf precursor in comparison to TMA,

reducing its ability to react with the oxidant precursor.[134] Finally, the deposition at 300 °C resulted in the formation of WO_x, with an estimated thickness of ~0.8 nm according to the thickness calculations from the W 4*f* signal attenuation. Also, there was no presence of a tungstate (WO_4) compound as occurred for Al_2O_3 at that temperature.

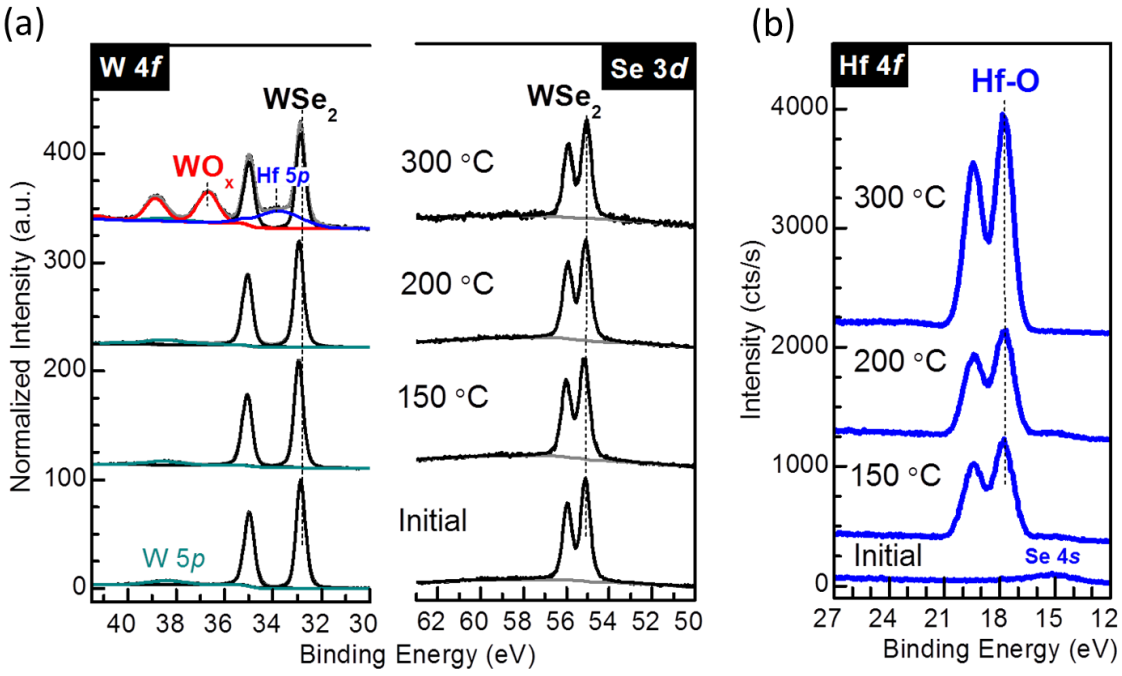

Figure 5.4. W 4*f*, Se 3*d* and Hf 4*f* XPS core levels showing the interface chemistry for HfO_2 deposited on WSe_2 using 30 cycles of TDMA-Hf and O_3 at 150 °C, 200 °C and 300 °C.

The effect of the deposition temperature on the high-κ dielectric thickness for an identical number of ALD cycles was also investigated. The use of the same number of cycles allows having a comparison of the deposition rate at the given temperatures for the ozone-based ALD process. Figure 5.5 summarizes the estimated thicknesses for Al_2O_3 and HfO_2 on WSe_2 calculated from the signal attenuation of W 4*f* due to the overlayer film with respect to the initial W 4*f* peak from bulk WSe_2. In the case of WO_x formation at the determined temperatures, the

estimated thickness also accounted for the oxide IL thickness, following the procedure described by Vitchev *et al.*[135] for a stack of n layers.

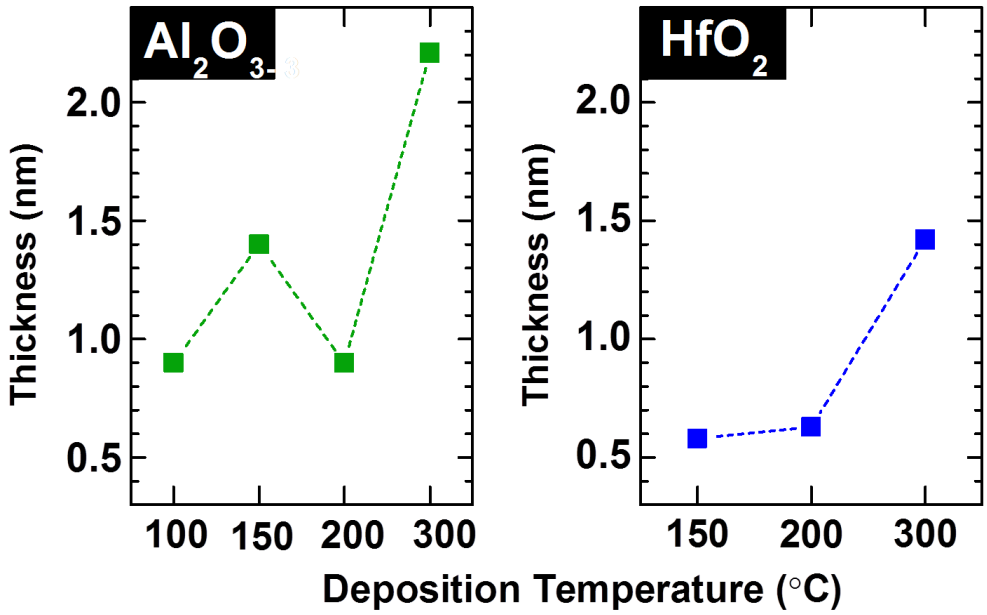

Figure 5.5. Deposition temperature dependence on the Al_2O_3 and HfO_2 thickness after 30 ALD cycles on WSe_2. The thickness is estimated based on the signal attenuation from the W 4f bulk WSe_2 peak, and accounting for the presence of an interfacial oxide layer. Lines are drawn to guide the eye.

Figure 5.5 shows that increasing the deposition temperature from 100 °C to 150 °C leads to an increase in Al_2O_3 thickness from 0.87 nm to 1.40 nm, respectively, for the same number of cycles. Interestingly, the increase in temperature to 200 °C caused a drop in Al_2O_3 thickness in comparison to 150 °C. This reduction can be related to the formation of WO_x and possible etching of WSe_2, which possibly had an effect on the deposition rate for Al_2O_3. The deposition at 300 °C led to a significant increase in Al_2O_3 thickness, even when an oxide IL was formed. This suggests that at 300 °C, the kinetics of the reaction enhanced the deposition rate, even when there were parallel reactions for the formation of WO_x and $Al_2(WO_4)_3$ during the ALD process. In the

case of HfO_2, the difference in thickness for deposition temperatures of 150 °C and 200 °C was minimal, and the deposition rate was increased significantly at 300 ° C. It is worth noting that for all the tested temperatures, the deposition rate for Al_2O_3 was superior in comparison to HfO_2 using the ozone-based ALD process on WSe_2.

5.5 ALD Temperature dependence on the dielectric/WSe_2 topography

Following the in-situ XPS characterization, the surface topography of the deposited films was determined by ex-situ AFM. Figure 5.6 shows the AFM images from these films along with the schematic of the interface that was obtained from XPS characterization.

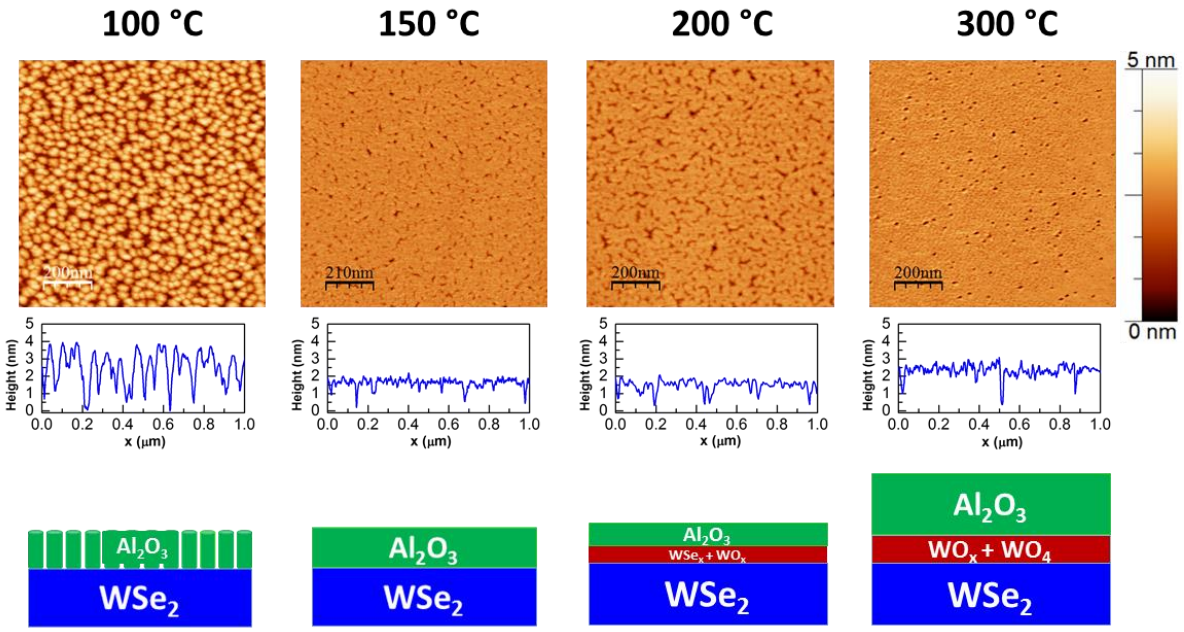

Figure 5.6. AFM images showing the surface topography of Al_2O_3 deposited on WSe_2 at different temperature using 30 cycles in the ozone-based ALD process.

Significant differences were obtained for in the surface topography of these films. For the deposition at 100 °C, Al_2O_3 clusters were obtained which reflect island growth. The Al_2O_3

islanding is consistent with the low Al_2O_3 thickness obtained by XPS. Better conformity and uniformity for the Al_2O_3 film grown at 150 °C was obtained. The improved growth could be related to the possible formation of Se-O bonds due to ozone exposure, as presented in section 5.3. Furthermore, at this temperature, no oxide is expected to be formed at the interface according to the XPS analysis. Therefore, 150 C can be a recommended temperature for Al_2O_3 deposition by ozone-based ALD. Yet, the film still presented a small density of pinholes with a depth of ~1 nm. For the film deposited at 200 °C, where WO_x and WSe_x are expected to be present at the interface, a higher density of pinholes was obtained, which is consistent with the decrease in thickness estimated from XPS. Interestingly, the 300 °C film, where an oxide IL was formed, presented pits at the surface, suggesting that the oxidation was non-uniform during the ozone-based ALD process.

The surface topography for HfO_2 deposited on WSe_2 was also investigated. Figure 5.7 shows that in contrast to the uniform Al_2O_3 film deposited at 150 °C, for the HfO_2 deposition at the same temperature, island growth occurred; and partial coverage was obtained after 30 ALD cycles. By increasing the deposition temperature to 200 °C, the HfO_2 islands started to exhibit coalescence, increasing HfO_2 coverage in comparison to the film at 150 °C. Full HfO_2 coverage was achieved at 300 °C, however, an interlayer oxide forms at this deposition temperature as detected by XPS. Interestingly, sporadic particles were found in this film, which could be formed due to an uneven morphology of the WO_3 interlayer. This result in the surface morphology is consistent with the lower thickness of HfO_2 detected by XPS in comparison to Al_2O_3. The poor coverage for the depositions at 150 °C and 200°C indicates that further optimization of the ALD parameter would be needed for the uniform deposition of this dielectric on WSe_2.

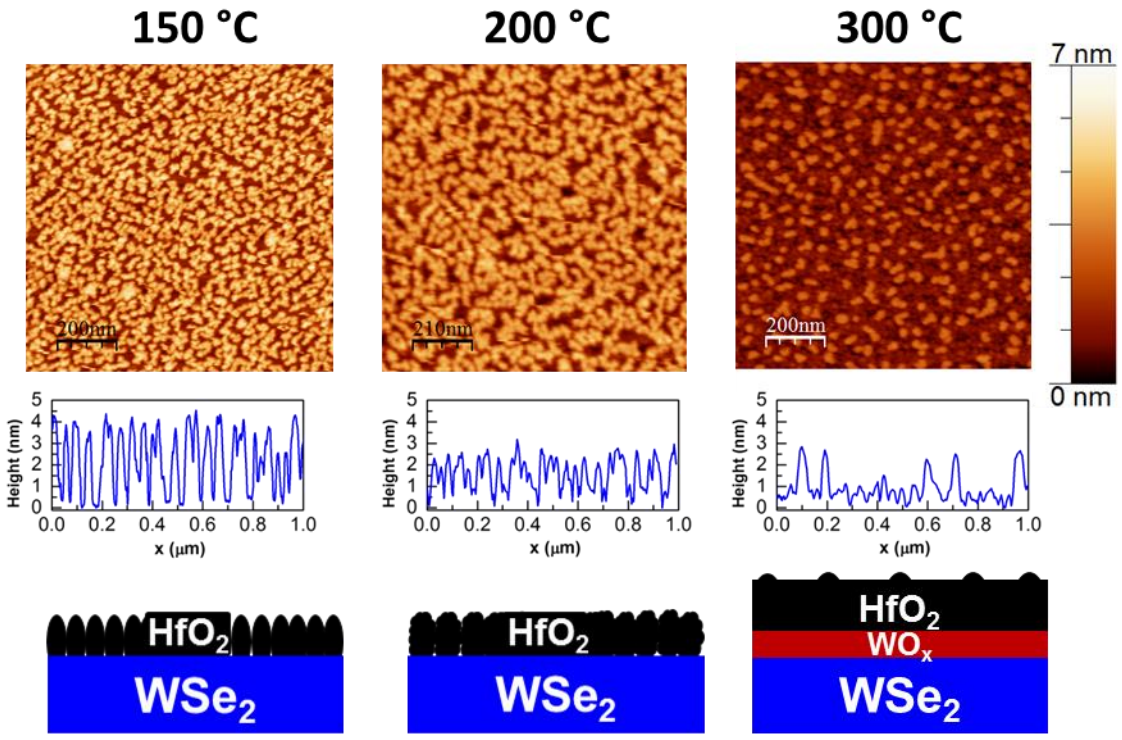

Figure 5.7. AFM images showing the surface topography of HfO_2 deposited on WSe_2 at different temperature using 30 cycles in the ozone-based ALD process.

5.6 Dielectric/WSe_2 Band Alignment

The determination of the valence band offsets (VBO) and conduction band offsets (CBO) values for the dielectric/WSe_2 system can serve as a guide for the design and analysis of WSe_2-based TFET. Therefore, the energy band alignment for the Al_2O_3/WSe_2 and HfO_2/WSe_2 stacks was obtained from in-situ XPS measurements. Since the presence of an oxide IL can contribute to the energy band alignment, the films employed for these measurements were deposited at temperatures at which no oxide formation was detected. Then, the VBO were calculated according to the procedure described by Kraut *et al.*,[136] following equation (5.1) for Al_2O_3 and (5.2) for HfO_2:

$$\Delta E_V = \left(E_{Al\ 2p} - E_{w\ 4f}\right)^{het} - \left[\left(E_{Al\ 2p} - E_{VBM}\right)_{Al_2O_3} - \left(E_{W\ 4f} - E_{VMB}\right)_{WSe_2}\right] \quad (5.1)$$

$$\Delta E_V = \left(E_{Hf\ 4f} - E_{w\ 4f}\right)^{het} - \left[\left(E_{Hf\ 4f} - E_{VBM}\right)_{HfO_2} - \left(E_{W\ 4f} - E_{VMB}\right)_{WSe_2}\right] \quad (5.2)$$

Where the valence band maximum energy values (E_{VBM}) were obtained from the linear regression of the valence band spectra from thick (>10 nm) Al_2O_3 and HfO_2 films, and from bulk WSe_2, respectively. The differences in the core level energies (e.g., $E_{Al\ 2p} - E_{w\ 4f}$) were obtained from Al_2O_3/WSe_2 and HfO_2/WSe_2 heterostructures (het).

The band gap values for Al_2O_3 and HfO_2 were determined from the energy difference between the peak position for the corresponding oxide in the O 1*s* core level and the onset of the O 1*s* loss feature[137,138] as shown in Figure 5.8a. The bandgap value for bulk WSe_2 was assumed to be 1.2 eV, according to the reported value in the literature.[139]

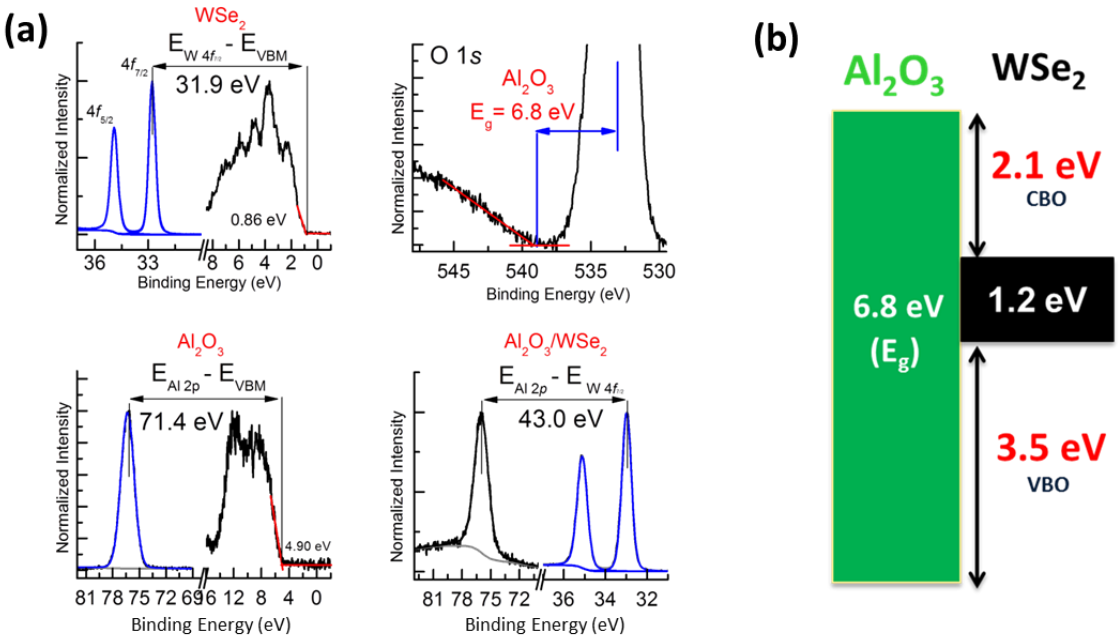

Figure 5.8. (a) XPS spectra from bulk WSe_2, thick Al_2O_3, and from the Al_2O_3/WSe_2 heterostructure, and the corresponding energy differences employed to construct the energy band alignment for Al_2O_3/WSe_2 in shown (b).

Figure 5.8 and Figure 5.9 shows the XPS spectra employed to determine the energy differences in equation 5.1 and 5.2 to construct the energy band diagrams for the Al_2O_3/WSe_2 and HfO_2/WSe_2 structures.

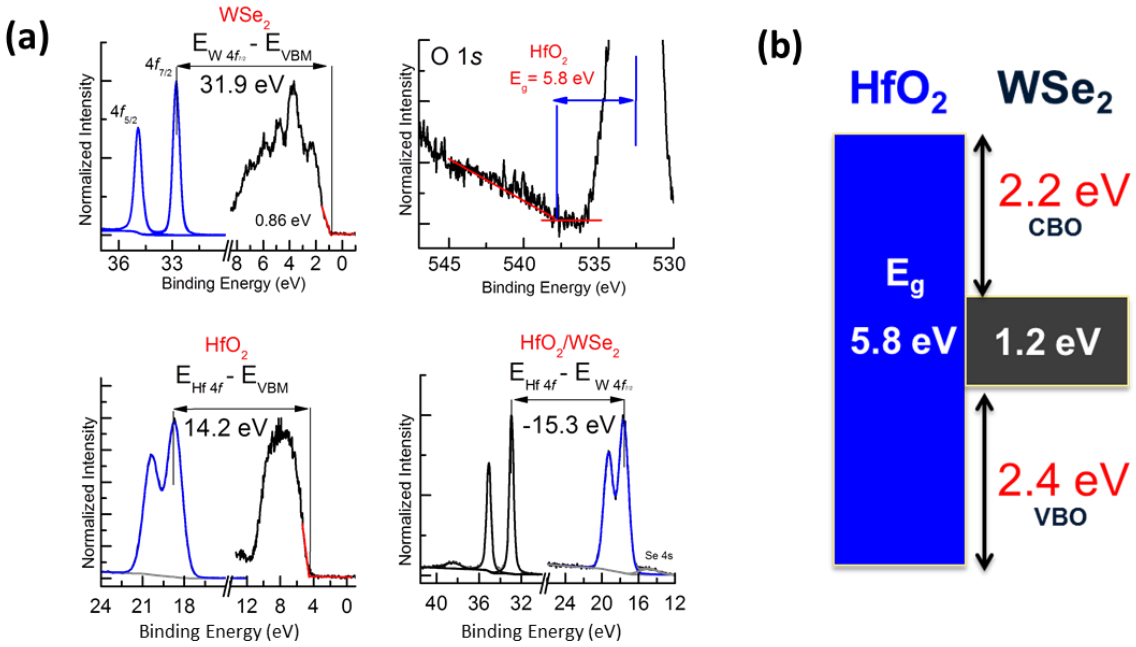

Figure 5.9. (a) XPS spectra from bulk WSe_2, thick HfO_2, and from the HfO_2/WSe_2 heterostructure, and the corresponding energy differences employed to construct the energy band alignment for HfO_2/WSe_2 shown in (b).

To reduce the probability of thermal emission from the channel to the gate, the valence band and conduction band offsets between WSe_2 and the high-κ dielectric are required to be large enough (> 1.0 eV).[140] According to the resulting band alignment, Al_2O_3 and HfO_2 fulfill such requirement, suggesting that these high-κ dielectrics are promising gate oxides to be implemented in 2D WSe_2 TFETs structures. Furthermore, the band alignment for Al_2O_3 suggests that this dielectric can be ideal gate oxide for p-type WSe_2 by providing a large valence band offset energy.

5.7 Low-Temperature AlO_x Seed Layer by Ozone-Based ALD

In order to further improve the nucleation of Al_2O_3 on WSe_2 and to avoid the presence of pinholes in the films, the use of an AlO_x seed layer grown by ozone-based ALD was investigated. The Al_2O_3 seed layer consists of exposing the surface to TMA and O_3 pulses at 30 °C. In fact, it was previously shown by Cheng *et al.*,[100] that a low-temperature seed layer allows the uniform deposition of Al_2O_3 on MoS_2. In that study, it was found that the ozone based ALD at 200 °C did not generate oxidation of MoS_2, and using a 5 cycles-Al_2O_3 seed layer deposited at 30 °C was sufficient to generate nucleation sites for subsequent ALD deposition.

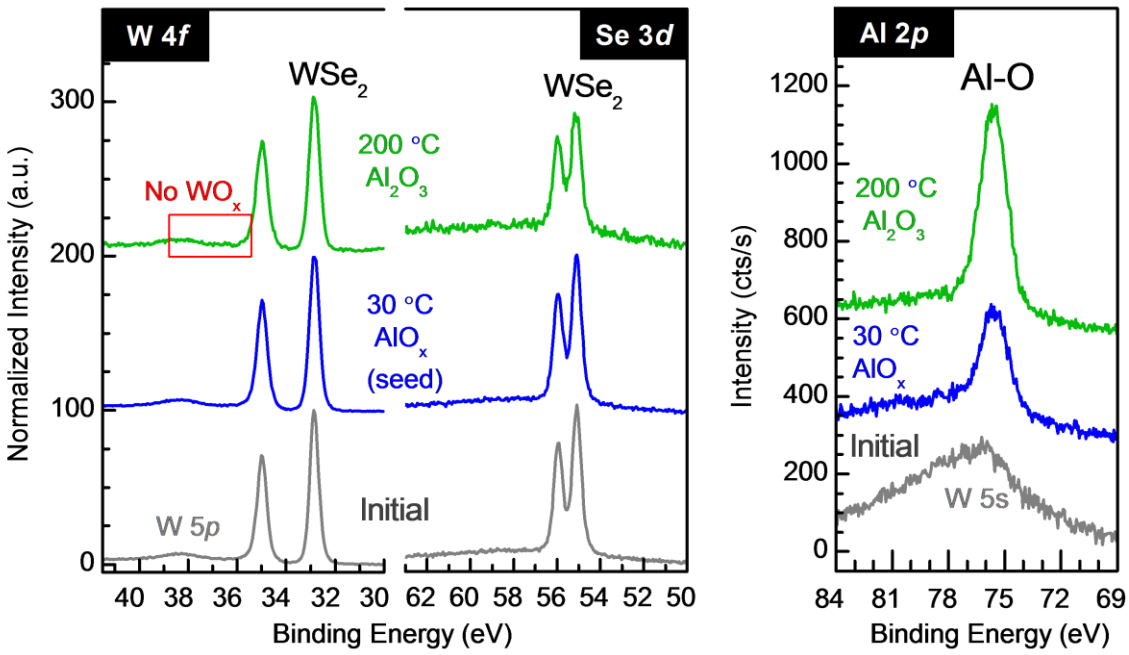

Figure 5.10. XPS spectra of WSe_2 upon deposition of an AlO_x seed layer at 30 °C and after subsequent Al_2O_3 growth at 200 °C by ozone-based ALD.

In contrast, a higher reactivity is observed for WSe_2, where WO_x and WSe_x are formed at 200 °C. Because of this difference in reactivity, careful control of the ALD parameters is needed. In

this study, the AlO_x seed layer consisted of 15 cycles of TMA/O_3 at 30 °C, followed by the Al_2O_3 deposition at 200 °C using 30 cycles of TMA/O_3. In-situ XPS was performed at each stage and the measured spectra are presented in Figure 5.10.

It was found that upon deposition of the low-temperature seed layer, no changes in the chemical state of WSe_2 occurred. This is consistent with the lack of reactivity observed for ozone only with WSe_2 as presented in section 5.3 In addition, the Al 2p spectra show a single peak for AlO_x at 75.6 eV, with an Al:O ratio of 1:1.6. The estimated thickness of the 15-cycles AlO_x seed layer from the signal attenuation of W 4*f* is ~0.7 nm. After a subsequent Al_2O_3 deposition at a higher temperature, 200 °C, on the seeded WSe_2, no evidence of interfacial oxidation was detected by XPS. Therefore, the presence of the seed layer prior the higher temperature ALD process prevented the partial etching and oxidation of WSe_2. In fact, the seed layer also enhanced the ALD nucleation of the film grown at 200 °C, as the surface morphology of the film shows uniformity with RMS roughness of 0.14 nm. Furthermore, the Al_2O_3 film was pinhole-free, which was confirmed by cross-sectional STEM imaging, presented in Figure 5.11.

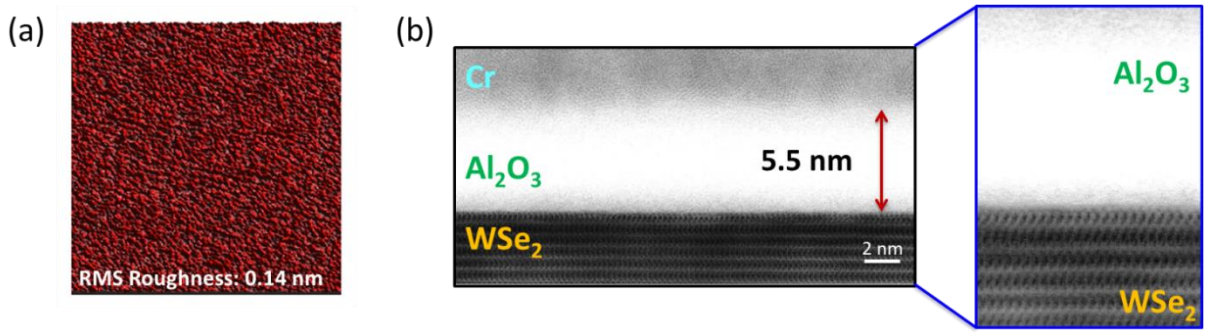

Figure 5.11.AFM and cross-sectional TEM imaging from the Al_2O_3 film grown on WSe_2 by ozone-based ALD using a 30 °C ALD-AlO_x seed layer followed by ALD-Al_2O_3 at 200 °C.

Also, a clean and sharp interface was obtained by the ozone-based ALD process described here, with a total thickness of 5.5 nm for the uniform Al_2O_3 film.

Finally, this process was implemented on monolayer WSe_2 flakes, which were obtained by mechanical exfoliation and transferred to a 300 nm SiO_2/Si substrate for characterization by Raman spectroscopy. The monolayer WSe_2 flake was first identified optically to acquire the Raman pre-scan, and then AlO_x deposition was carried out by ALD using 15 cycles of TMA/O_3 at 30 °C followed by 30 cycles of TMA/O_3 at 200 °C. The Raman spectrum was acquired after ALD. Figure 5.12 shows that the characteristic Raman peaks for WSe_2, E^1_{2g} at 249.5 cm^{-1} and A_{1g} at 260.5 cm^{-1}, were not perturbed after the ozone-based ALD process.

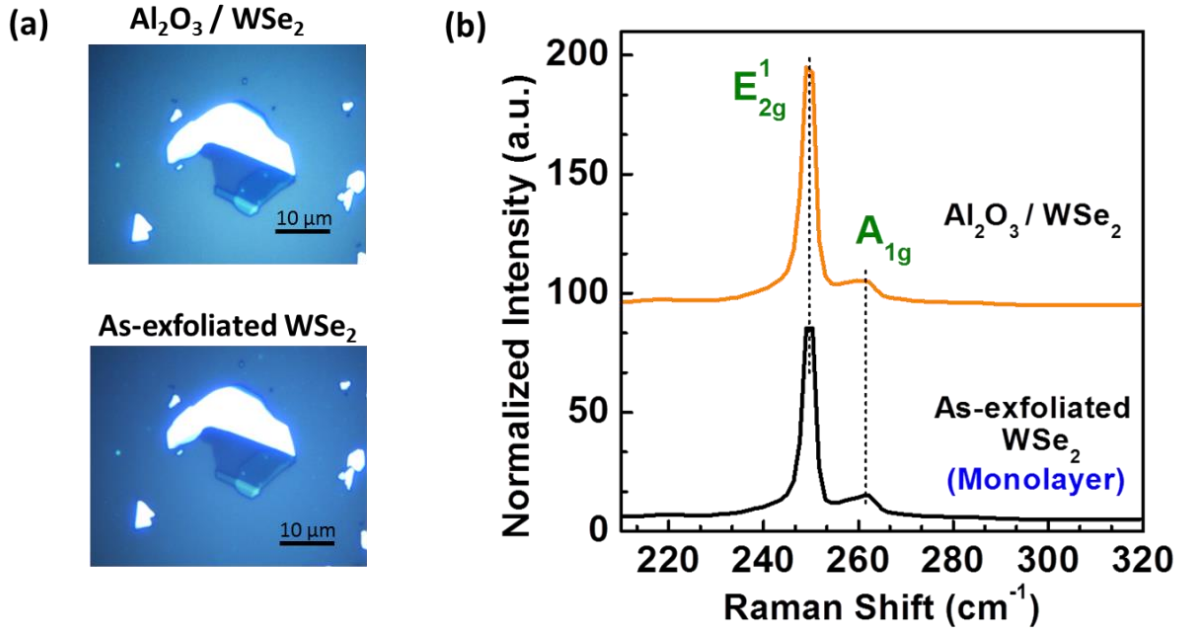

Figure 5.12. (a) Optical image and (b) Raman spectra of monolayer WSe_2 before and after Al_2O_3 deposition by ozone-based ALD.

Only a signal attenuation of ~0.71 occurred after Al_2O_3 deposition with respect to the initial spectrum. This result highlights that even for the case of monolayer or few-layer WSe_2, the use

of ozone-based ALD with the optimized parameters will not induce damage (e.g., layer etching) to the two-dimensional material.

5.8 Conclusions

In this work, ozone-based ALD was evaluated for the deposition of high-κ dielectrics on WSe_2. It was found that the interfacial chemistry, deposition rate and surface topography of Al_2O_3 and HfO_2 exhibited a dependence on the deposition temperature. Differences in reactivity were identified between the metal-organic precursors TMA and TDMA-Hf, upon deposition on the WSe_2 surface. This study provides a temperature window for the optimal deposition of $Al2O_3$ and HfO_2 by ozone-based ALD on WSe_2, which can serve to prevent oxidation and etching of WSe_2. The energy band alignments were determined from the high-κ dielectric/WSe_2 stack, which are important parameters for the device design and analysis of 2D WSe_2-based FETs Finally, the use of a low-temperature AlO_x seed layer was found to enhance the nucleation for the Al_2O_3 films grown at a conventional ALD temperature (200 °C) and it also prevented the oxidation of the WSe_2 substrate. With such ozone-based ALD process, uniform and thin Al_2O_3 films were demonstrated. The future work includes the determination of the electrical properties of these films through capacitor structures and integration of the Al_2O_3 deposited by the ozone based ALD in TFETs structures.

CHAPTER 6

NITROGEN DOPING OF MOS_2

6.1 Introduction

Recently, the use of plasma surface treatments has been proposed as a strategy to incorporate dopant atoms such as fluorine[141] and phosphorous[142] in the MoS_2 structure. However, these plasma-assisted doping processes can generate undesirable side effects of such as layer etching and degradation of the I_{ON} current for the respective plasma doped MoS_2 FETs, which suggests that improvement of the plasma processing for TMDs is still to be developed. Encouraged by the efforts on the exploration of plasma assisted doping strategies for TMDs, the use of remote N_2 plasma treatment for the introduction of nitrogen in MoS_2 as a dopant atom is investigated in this work. N_2 plasma exposure is a practical technique that has been widely used for the incorporation of nitrogen atoms into the lattice of various semiconductors[143,144] and metal gate materials,[145,146] and it has been successfully applied for nitrogen doping of graphene.[147] In the case of monolayer MoS_2, nitrogen doping is predicted to induce p-type behavior according to first principles calculations.[148,149] Here, evidence of the covalent nitrogen doping of MoS_2 upon remote N_2 plasma exposure is provided directly. It was found that a controllable nitrogen concentration can be realized with N_2 plasma exposure time. Furthermore, the electrical characterization indicates that nitrogen acts as a p-type dopant in MoS_2 and, more importantly, that the electronic performance of the N_2 plasma treated MoS_2 was preserved in reference with the untreated MoS_2. The structural changes associated with the N_2 plasma exposure on the MoS_2

surface are also presented here. We present the first report of strain induced by a single-atom dopant in a TMD material. Finally, first principles calculations were performed to estimate the relation between strain and nitrogen concentration in MoS_2.

This chapter includes the material adapted with permission from a publication entitled **"Covalent Nitrogen Doping and Compressive Strain in MoS_2 by Remote N_2 plasma exposure"** [Nano Lett. **2016**, 16, 5437–5443] Copyright 2016 American Chemical Society. The authors are A. Azcatl, X. Qin, A. Prakash, C. Zhang, L. Cheng, Q. Wang, N. Lu, M. J. Kim, J. Kim, K. Cho, R. Addou, C. L. Hinkle, J. Appenzeller and R. M. Wallace. My contribution was to conceive the idea, design the experiments, analyzing the data and writing the manuscript. A. Prakash and J. Appenzeller conducted the electrical characterization. C. Zhang and K. Cho. performed the theoretical work. L. Cheng assisted in the Raman measurements. Q. Wang., N. Lu and M. J. Kim performed the transmission electron microscopy. J. Appenzeller, C. L. Hinkle, and R. M. Wallace contributed to the data interpretation and inputs on the manuscript writing.

6.2 Experimental Details

Nitrogen doping of MoS_2 was achieved by exposing the MoS_2 surface to remote N_2 plasma generated by a 13.56 MHz RF plasma source at a power of 100 W, using N_2 as gas source flowing at 45 sccm, at a substrate temperature of 300 °C. The schematic of the setup employed for the remote N_2 plasma exposure is presented in Figure 6.1. It is important to note that a mixture of Ar (60 sccm) and N_2 (45 sccm) was used to generate the plasma; however, Ar was switched off during the treatment since Ar can cause etching of the outermost MoS_2 layers. All the remote plasma exposures were performed in a chamber which has a base pressure of $\sim 10^{-9}$

mbar and an operating pressure kept at 7×10^{-3} mbar during the remote plasma exposure. The distance from the source to the sample surface is ~30 cm.

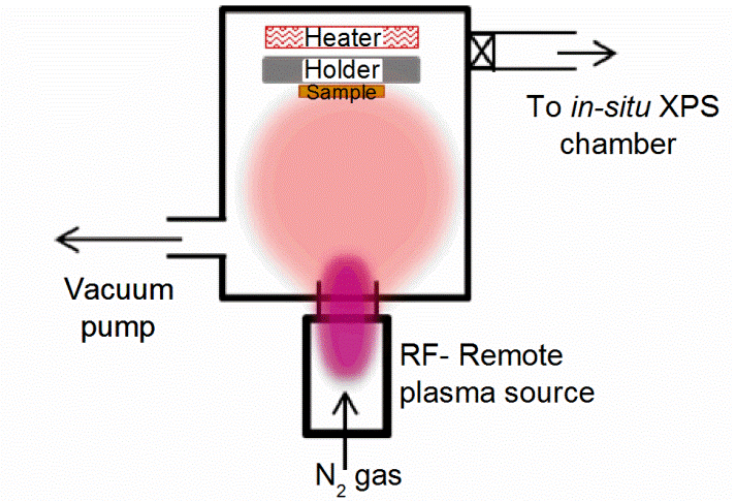

Figure 6.1. Schematic of the remote plasma system employed for the N_2 plasma exposures on MoS_2.

In-situ X-ray photoelectron spectroscopy characterization was performed in an ultrahigh vacuum (UHV) system described previously. XPS was carried out using a monochromated Al Kα source (hν = 1486.7 eV) and an Omicron EA125 hemispherical 7-channel analyzer. The XPS scans were acquired at a take-off angle of 45° with respect to the sample normal and pass energy of 15 eV. For XPS peak analysis and deconvolution, the software *AAnalyzer* was employed, where Voigt line shapes and an active Shirley background were used for peak fitting.[66] For the *in-situ* XPS characterization, natural bulk MoS_2 (SPI) was mechanically exfoliated using Scotch® tape to peel off the top-most surface layers, followed by loading into the UHV system (within five minutes). As noted in the text, annealing in UHV was conducted at 300 °C for one hour to desorb physisorbed species from the minimal air exposure of the exfoliated surface.

For the electrical characterization, MoS_2 flakes of various thicknesses were mechanically exfoliated onto two identical substrates, each with a top layer of 90 nm SiO_2 and underlying heavily doped (p^{++}) Si. Flakes of various thicknesses were initially approximately identified by optical contrast and the flake thicknesses were later determined accurately by atomic force microscopy (AFM). MoS_2 flakes on one of the two substrates were subjected to annealing, followed by the N_2 plasma treatment mentioned in the main text. Both sets of samples, one set consisting of as-exfoliated MoS_2 and the other consisting of N_2 plasma treated MoS_2 flakes were processed together to fabricate FETs. Electron beam lithography, followed by electron beam evaporation and lift-off was used to define the source and drain contacts. Ni was used as the contact metal. After fabrication of the devices, the electrical characteristics were obtained in air in a Lakeshore probe station using an Agilent semiconductor parameter analyzer. In all measurements, the 90 nm SiO_2 was used as the gate dielectric and the highly doped Si underneath was used as the back gate.

For Raman Spectroscopy, MoS_2 flakes were transferred onto 300 nm SiO_2/Si substrate by mechanical exfoliation. The Raman spectra were acquired using a 532 nm wavelength laser using a Renishaw confocal Raman system model inVia under air-ambient conditions. AFM characterization was performed on tapping mode, using an Atomic Probe Microscope (Veeco, Model 3100 Dimension V), also under air-ambient conditions. The processing of the AFM images was performed using WSxM 4.0 software.

High-resolution transmission electron microscopy (TEM) cross-sectional specimens of the N-doped MoS_2 samples were made by an FEI Nova 200 dual-beam focused ion beam (FIB)/scanning electron microscope (SEM) with the lift-out method. In FIB, SiO_2 and Pt layers

were deposited to protect the interested region during focused Ga ion beam milling. For TEM imaging, a JEOL ARM200F operated at 200 kV with a probe aberration corrector was used for atomic resolution high angle angular dark field (HAADF) scanning transmission electron microscopy (STEM). The contrast in an HAADF-STEM image is approximately proportional to Z^2, where Z is the atomic number.[150]

The modeling of the nitrogen-doped bilayer MoS_2 is performed within the framework of density functional theory (DFT) using Vienna *ab initio* package (VASP).[105] Calculations based on the generalized gradient approximation (GGA) using the Perdew-Burke-Ernzerhof (PBE)[151] functional are carried out with projector augmented wave (PAW)[104] pseudopotential plane-wave method. The few-layer, N-doped MoS_2 structures are optimized with a vacuum thickness of about 18 Å. The Monkhorst-Pack k-point sampling method in Brillouin zone is Γ-centered with a 4×4×1 mesh in ionic optimization.[152] The cutoff energy is 500 eV and the criteria of convergence for energy and force are set to be 1×10^{-4} eV and 0.02 eV/Å, respectively.

6.3 Nitrogen Doping of MoS_2

The presence and chemical identity of nitrogen in bulk MoS_2 upon N_2 plasma exposure was investigated by *in-situ* x-ray photoelectron spectroscopy (XPS). Figure 6.2 shows the XPS spectra for as-exfoliated MoS_2 before and after 30 min N_2 plasma exposure on the as-exfoliated surface and on a MoS_2 sample that received a pre-anneal at 300 °C for two hours under ultrahigh vacuum (UHV) to remove the carbonaceous contamination adsorbed during the short air exposure. As shown in Figure 6.2, two peaks in the N1*s* region are detected at 398.6 eV and 400.1 eV on the as-exfoliated (unannealed) MoS_2 surface after N_2 plasma exposure. By

correlation with the C 1*s* region, these chemical species are identified as CN_x and CN_x-H, respectively.[153] Therefore, without the pre-annealing step, the adsorbed carbon that is present on the initial MoS_2 surface (likely physisorbed from the brief atmospheric exposure after exfoliation and prior to placement in vacuum) is readily available to react with the nitrogen species present in the remote N_2 plasma to form the aforementioned cyano species, complicating the quantitative analysis of the N 1*s* region for the identification of the Mo-N bond. On the other hand, after N_2 plasma exposure on the annealed MoS_2, no detectable CN_x species were present on the surface. More importantly, an evident peak was detected at 397.5 eV in the N 1*s* region, indicating the presence of nitrogen in MoS_2. It should be noted that Mo $3p_{3/2}$ spans over the N 1*s* region, as evidenced by a peak associated with MoS_2 centered at ~394.8 eV. For this reason, the identification of nitrogen related peaks requires a detailed analysis of the high binding energy side of the Mo $3p_{3/2}$ peak. Examining the Mo 3*d* region, a shoulder at ~0.4 eV higher in binding energy than the Mo-S peak also developed after the N2 plasma exposure. By correlation of the new chemical states in N 1*s* and Mo 3*d*, the formation of a Mo-N bond was identified, with XPS peak positions consistent with those reported in the literature.[154,155]

In order to understand the formation of the covalent Mo-S bond in MoS_2 by remote N_2 plasma, sequential exposures on the annealed MoS_2 surface were carried out, while in-situ XPS characterization was employed to monitor the surface chemistry. The first N_2 plasma exposure ("*t1*") was performed for 2 min, after which a low-intensity peak at ~ 397.7 eV was detected in the N 1*s* region, as shown in Figure 6.3.

The corresponding feature in Mo 3d for the Mo-N was detected at 229.8 eV. Additionally, at *t1* the full width at half maximum (FWHM) of the Mo-S peaks in Mo 3*d* and S 2*p* increased by

~25% with respect to as-exfoliated MoS_2, reflecting some degree of bond diversity generated at the MoS_2 surface.

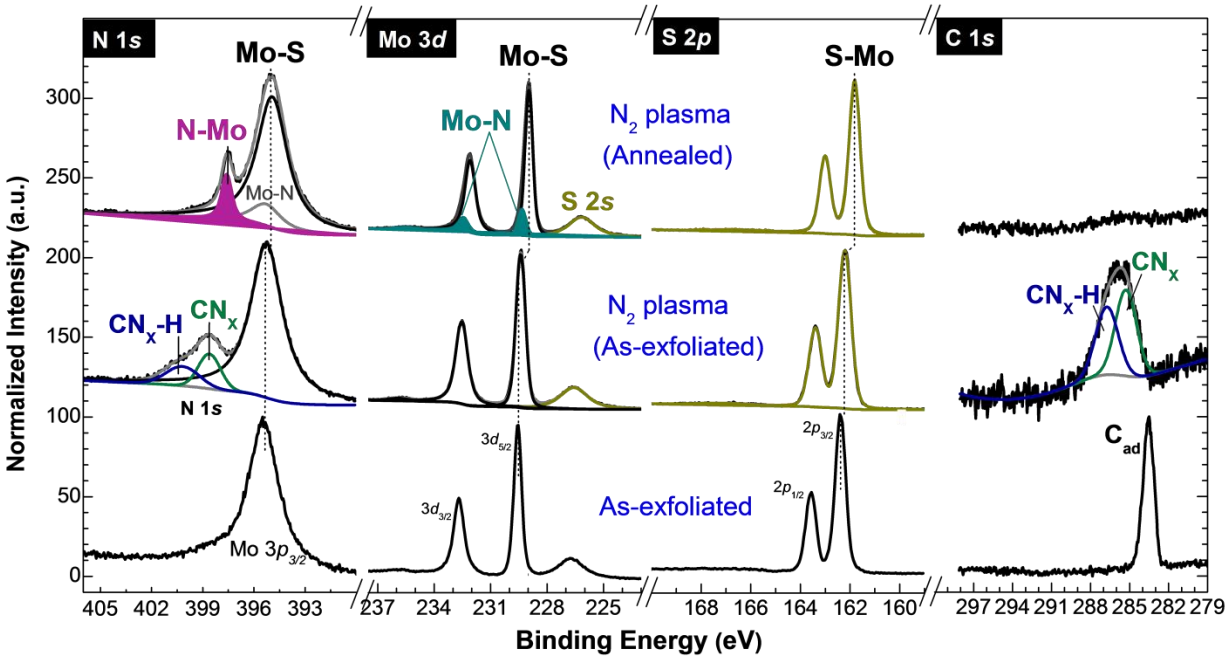

Figure 6.2. XPS spectra for MoS_2 before and after N_2 plasma exposure on the as-exfoliated surface and on a pre-annealed surface under UHV at 300 °C for two hours.

It is noted that nitrogen did not exhibit reactivity with sulfur, as no additional chemical states indicative of S-N bonding (164.8 eV)[156] were detected in the S 2*p* region. With further plasma exposures, *t2*=7 min, *t3*=15 min, *t4*=30 min, and *t5*=60 min, the intensity of the Mo-N bond in both N 1*s* and Mo 3*d* regions increased, while no additional nitrogen species were detected throughout the process.

In parallel with this increase in nitrogen concentration, the total sulfur content in MoS_2 decreased as shown in Figure 6.3b, suggesting preferential removal of sulfur. These concomitant changes in sulfur concentration with N_2 plasma exposure time suggests that the mechanism of formation of

N-Mo bonds involves sulfur substitution by nitrogen in the MoS_2 structure, consistent with first principle calculations which have shown that nitrogen will behave as a substitutional dopant.[148]

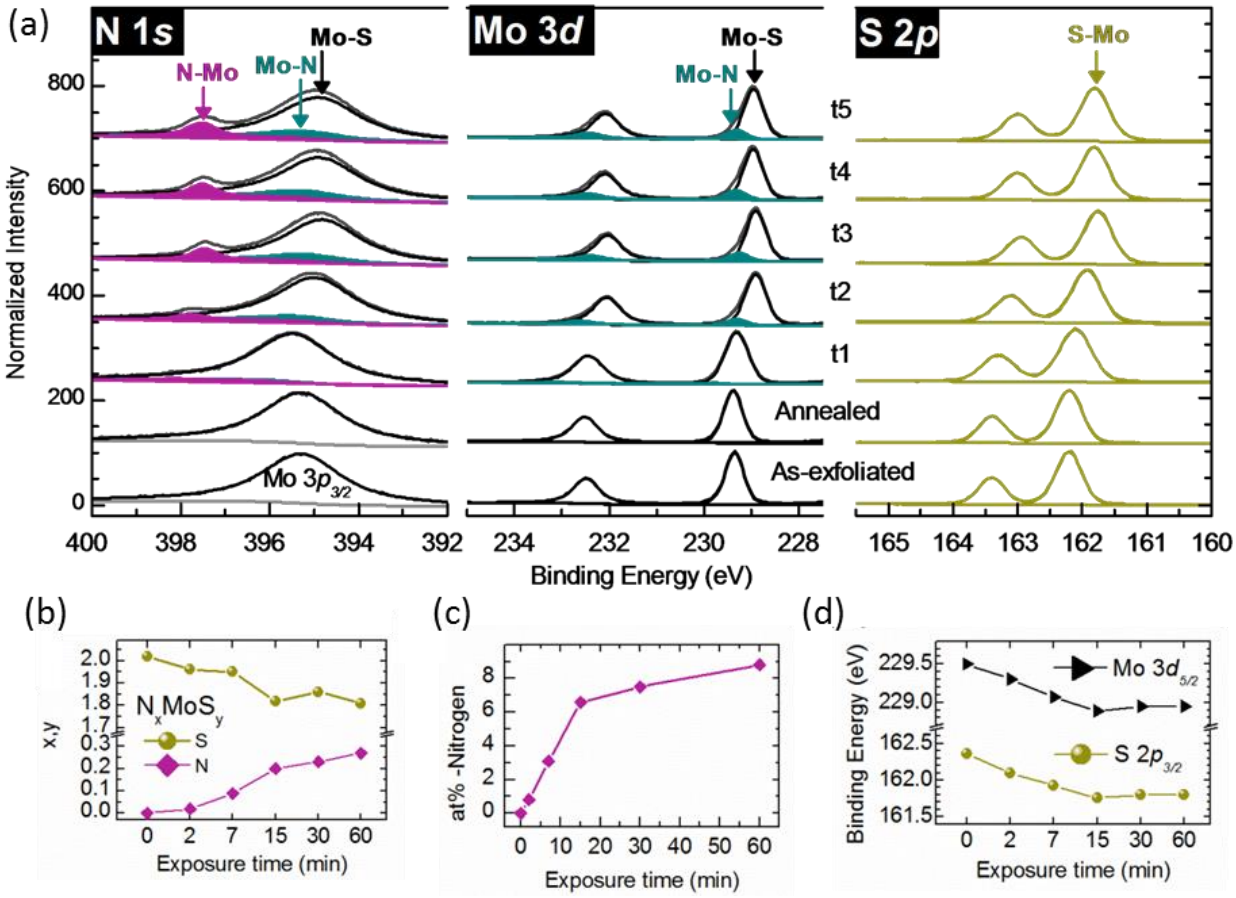

Figure 6.3. (a) XPS spectra from as-exfoliated MoS_2 showing the N 1*s*, Mo 3*d* and S 2*p* core levels after annealing and after sequential N_2 plasma exposures, where *t1*= 2 min, *t2*=7 min, *t3*=15 min, *t4*=30 min, *t5*=60 min. . (b) Stoichiometry for the N-doped MoS_2 system represented as N_xMoS_y. (c) peak positions for Mo 3d and S 2p from MoS2 with respect to N_2 plasma exposure time obtained from the XPS spectra in (a). (d) Atomic percentage (at %) of nitrogen in MoS_2 as a function of N_2 plasma exposure time.

The atomic concentration (at. %) of nitrogen in MoS_2 achieved by varying the N_2 plasma exposure time obtained from the quantitative analysis of the XPS spectra is shown in Figure

6.3c, where the at% of nitrogen exhibited a logarithmic relation with N_2 plasma exposure time. Importantly, the oxygen and carbon concentration on the MoS_2 surface were below XPS detection limits during the experiment, since an annealing step was carried out prior the sequential N_2 plasma exposures, as shown in Figure 6.4.

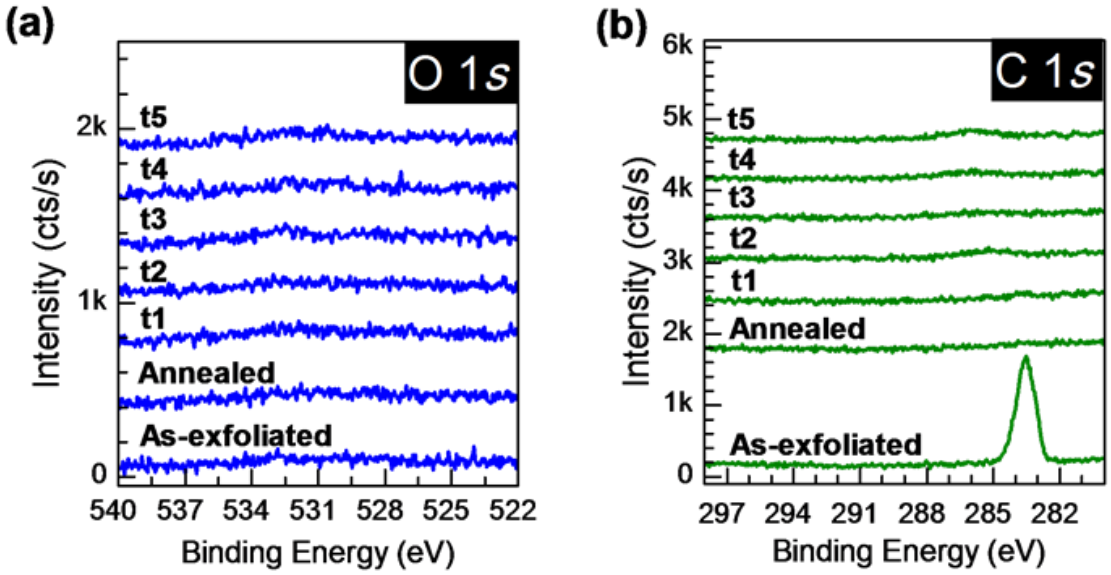

Figure 6.4. (a) O 1*s* and (b) C 1*s* from as-exfoliated MoS_2, after annealing at 300 C for one hour and after sequential N_2 plasma exposures (*t1*=2 min, *t2*=7 min, *t3*=15 min, *t4*=30 min, *t5*=60 min).

This highlights that there was no contribution from oxygen or carbon for the quantitative analysis presented in this work, which was achieved by performing the N_2 plasma exposures and XPS analysis *in-situ* in a UHV environment. In addition, the formation of undesirable by-products (e.g., oxy molybdenum nitride, or CN_x) was ruled out.

To estimate the areal density of nitrogen atoms on the MoS_2 surface, the nitrogen coverage (Θ_N) was calculated from the ratio of the integrated intensities of N 1*s* to Mo $3d_{5/2}$, using equation 6.1[157,158]

$$\Theta_N = \frac{I_N}{S_N} \Big/ \frac{I_{Mo}}{S_{Mo} \sum_{n=0}^{\infty} \exp[-n\, d_{MoS_2}/\lambda_{Mo} sin(\theta)]} \quad (6.1)$$

Where I_N and I_{Mo} are the integrated intensities from the N-Mo peak in N 1s and the Mo-S peak in Mo $3d_{5/2}$, respectively, λ_{Mo} is the inelastic mean free path for Mo 3d core level electrons in MoS_2 obtained from the NIST electron EAL Database, *n* corresponds to the number of planes that contributes to the XPS signal, d_{MoS_2}= 0.62 nm is the distance between two molybdenum planes in the MoS_2 structure, and S_{Mo} and S_N are the relative sensitivity factors for N 1*s* and Mo $3d_{5/2}$ which values correspond to 1.731 and 0.477, respectively.[159] All XPS spectra shown in the main text were acquired at a take-off angle of 45°.

For the N_2 plasma exposure times shown in Figure 1a, the resulting Θ_N is 0.1 ML for *t1*, 0.35 ML for *t2*, 0.77 ML for *t3*, 0.92 ML for *t4*, and 1.08 ML for *t5*, where 1 ML corresponds to 1.16×10^{15} atoms/cm^2 for the MoS_2(0001) basal plane. To further study the depth at which nitrogen is present in MoS_2, a bulk-sensitive take-off angle of 80° was also used to acquire the XPS data after 60 min N_2 plasma treatment on MoS_2. Figure 6.5 shows that the N-Mo peak intensity decreased when the spectra were acquired at the 80° take-off angle, indicating that nitrogen was not inserted into deeper MoS_2 layers in this process. Furthermore, using the XPS data acquired at 80° the resulting Θ_N is ~1 ML, as presented in Table 6.1, which is consistent with the coverage obtained at 45°. According to these values of nitrogen coverage and angle-resolved XPS measurements, the introduction of nitrogen by the remote N_2 plasma exposure occurs at the outermost MoS_2 surface.

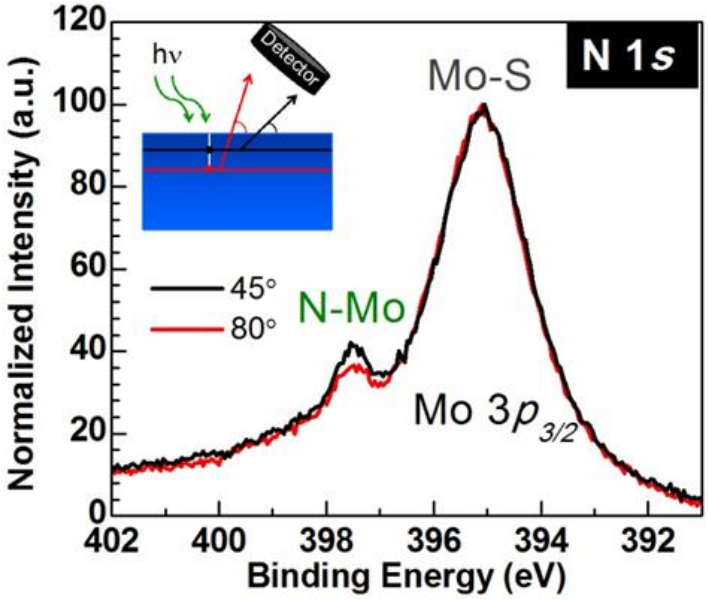

Figure 6.5. N 1s spectra from 60 min N_2 plasma treated MoS_2 acquired at take-off angles of 45° (surface sensitive) and 80° (bulk sensitive).

Table 6.1. Calculated nitrogen coverage obtained at take-off angles of 45° and 80°, and corresponding integrated intensity ratios for N1*s* and Mo 3$d_{5/2}$, and inelastic mean free path λ values used for the calculation.

Take-off Angle	$I_{N\,1s} / I_{Mo\,3d_{5/2}}$ Ratio	λ_{Mo}	N coverage (ML)
45°	0.081	2.431	0.99
80°	0.066	2.493	1.06

Nitridation of MoS_2 was previously reported to be achieved by exposing MoS_2 powder to NH_3 at 750 °C. Another approach for nitrogen doping of MoS_2 was reported to be performed by synthesis of MoS_2 nanosheets using a sol-gel method.[160] In contrast, the advantage of the N_2 plasma process described in this work is that a controllable concentration of the nitrogen dopant was realized, where the newly formed Mo-N bond owns a covalent character due to the strong

hybridization between the N 2*p* and Mo 4*d* orbitals.[161,162] Here, the thermal stability of the Mo-N bond was tested by performing annealing at 300 °C and 500 °C under UHV conditions (~10^{-9} mbar).of a 20 min N_2 plasma exposed MoS_2 sample. The XPS spectra in Figure 6.6 shows that the N-Mo/Mo-$S_{(\mathrm{Mo}3p_{3/2})}$ peak ratio of 0.072±0.004 remained constant upon annealing, which suggested that no desorption or thermal diffusion of nitrogen occurred at these temperatures. Such thermal stability of the N-Mo bond upon annealing is consistent with its covalent bonding nature.

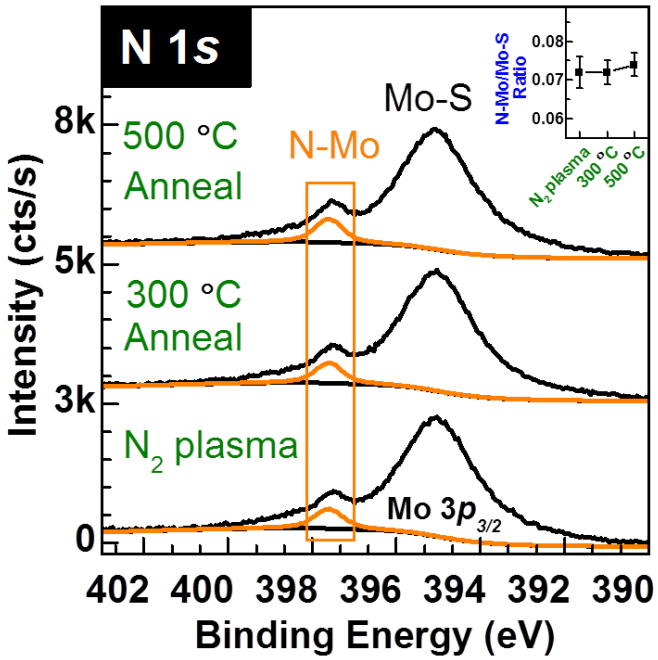

Figure 6.6. N 1*s* XPS spectra showing the N-Mo bond in MoS_2 generated after N_2 plasma and after annealing for an hour at 300 °C and 500 °C under UHV.

6.3.1 p-type Doping Effect of Nitrogen in MoS_2

According to the peak positions for Mo 3*d* and S 2*p*, the initial as-exfoliated MoS_2 surface exhibited the commonly observed unintentional n-type doping.[35] Interestingly, all regions in the

XPS spectra shifted identically to lower binding energies with N_2 plasma exposure from *t1* to *t3* as shown in Figure 6.3d, suggesting a change in the Fermi level associated with p-type doping. Yet, the interpretation of the magnitude of the Fermi level shift for nitrogen doped MoS_2 (N-doped MoS_2) is not straightforward. The charge transfer due to the presence of nitrogen as a p-type dopant,[149] with the band bending induced by the formation of Mo-N covalent bonds at the top-most layer and the preferential sulfur removal,[163] will both contribute to the measured shift. The overall effect on the valence band spectra reveals that the Fermi level moves closer to the MoS_2 valence band.

A comparative band alignment of MoS_2 before and after 15 min of N_2 plasma treatment is presented in Figure 6.7. The band diagrams were constructed from XPS measurements, where the work function (Φ) and the valence band maximum (VBM) were obtained from the secondary electron cutoff energy and the valence band edge, respectively. where a band gap value of 1.23 eV ± 0.02 eV for bulk MoS_2[11] was employed. The band gap of bulk MoS_2 was assumed to remain constant upon nitrogen doping. The resulting energy band diagram shows that the work function increased by ~0.26 eV after 15 min of N_2 plasma exposure, suggesting that nitrogen doping can potentially be applied to tune the work function of MoS_2. In addition, the Fermi level shift detected after the N_2 plasma exposure moves the valence band maximum from 0.87± 0.13 eV corresponding to n-type MoS_2 to a value of 0.34± 0.07 eV for nitrogen doped MoS_2, providing evidence of p-type doping.

It is also noted that during the doping process described in this work, the oxygen and carbon concentration on the MoS_2 surface were below XPS detection limits. Therefore, nitrogen was exclusively the only element involved in the Fermi level shift towards the valence band in MoS_2.

Finally, the estimated electron affinity, which was estimated using the measured Φ and VBM values, decreased after nitrogen doping, which can be related to the modification of surface termination in MoS_2, from sulfur to nitrogen terminated.[164]

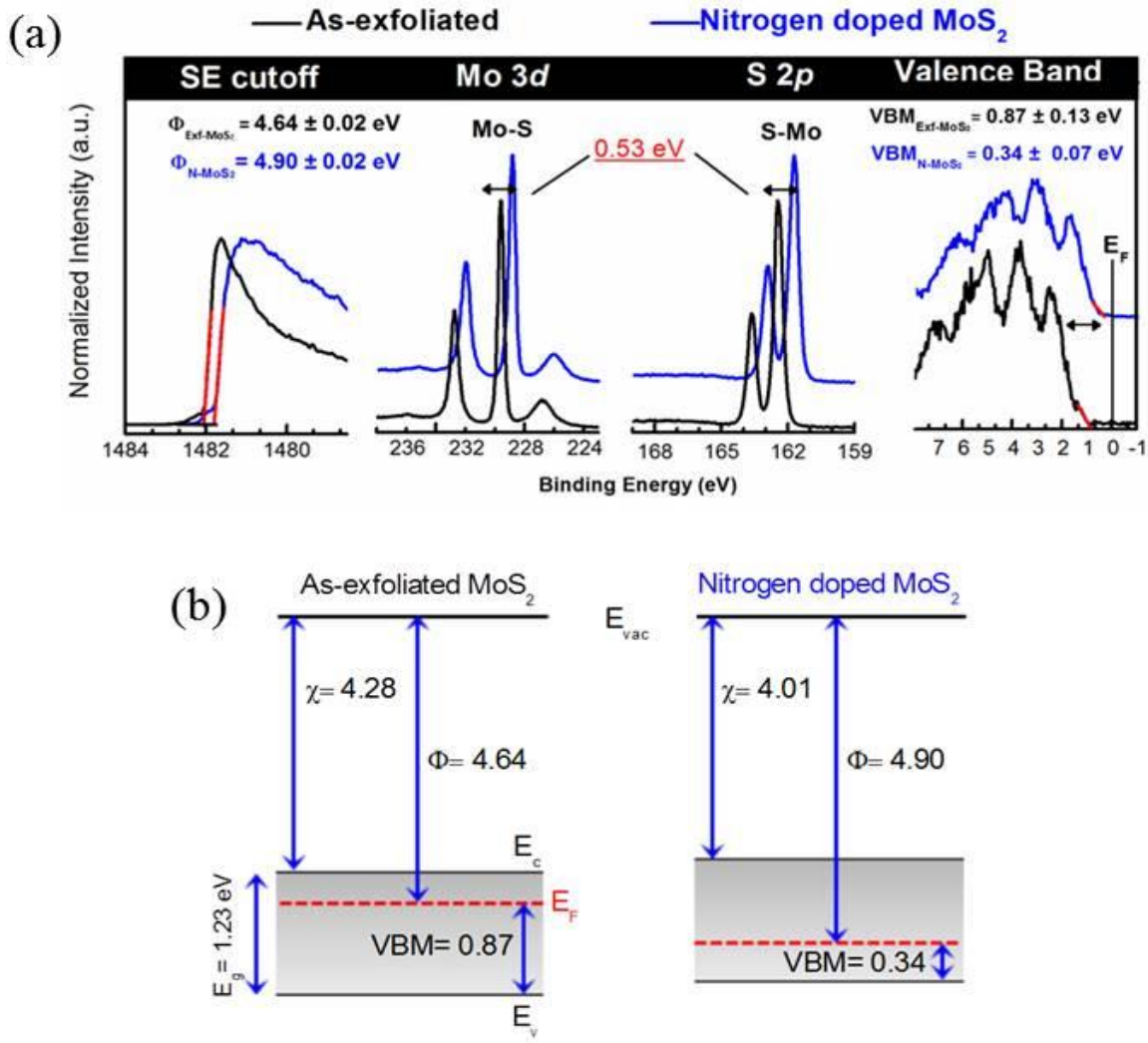

Figure 6.7. (a) The secondary electron (SE) cutoff energy, and the valence band edge measured by XPS to obtain the work function (Φ) and valence band maximum (VBM), respectively for as-exfoliated and N-doped MoS_2. Error bars for the linear fitting of the secondary electron cut-off energy and valence band edge are shown. (b) Energy band diagram for as-exfoliated MoS_2 and nitrogen doped MoS_2 constructed using the values of Φ and VBM from (a). The band gap (E_g) was obtained from the reported value for bulk MoS_2 (1.23 eV)[11] The electron affinity (χ) was estimated based on the measured Φ and VBM. All values shown here are in eV units.

To further investigate the electrical properties of the nitrogen doped MoS_2 and support the initial evidence of p-type doping given by XPS, back-gated field effect transistors (FETs) were fabricated with the device structure as shown in Figure 6.8. For the electrical characterization, a 15 min N_2 plasma exposure was performed on MoS_2 flakes with different thicknesses exfoliated on a SiO_2/Si substrate. Figure 6.8b shows the I_{DS}-V_{GS} characteristics for back-gated nitrogen doped MoS_2-based FET for flakes of various thicknesses, while Figure 6.9 shows the I_{DS}-V_{GS} characteristics specifying the number of MoS_2 layers employed in the measurements.

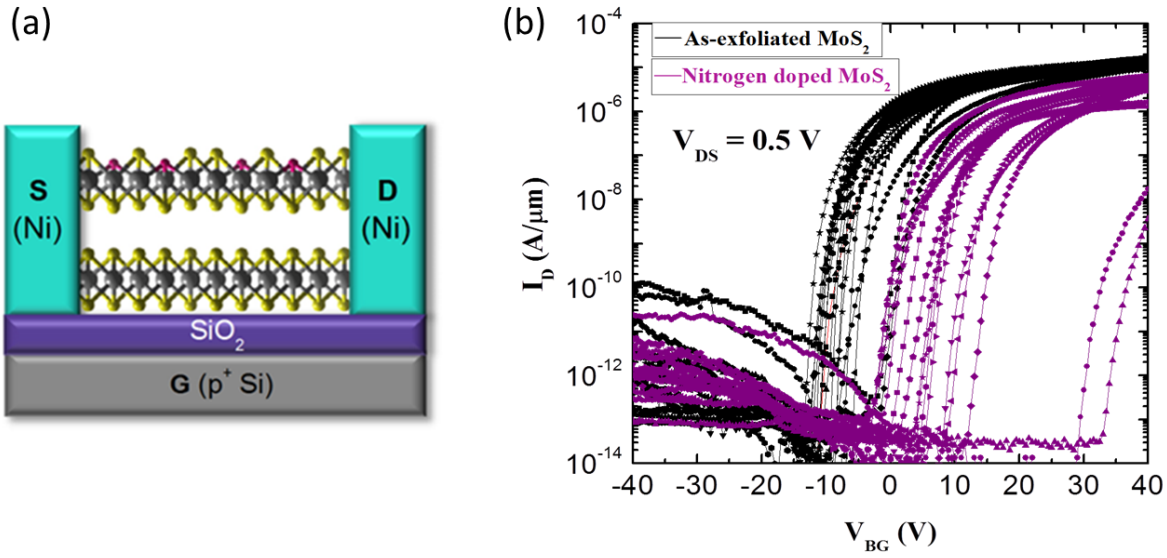

Figure 6.8. (a) Schematic of the back-gated nitrogen doped MoS_2 FET on Si/SiO_2 structure used in this study. (b) I_{DS}-V_{GS} characteristics from various MoS_2 FETs based on as-exfoliated MoS_2 (black) and nitrogen doped MoS_2 (purple), where each curve represents the measurement from a MoS_2 flake having a determined thickness.

Note that in all measurements the same scan conditions and gate voltage range was used to allow for a proper comparison of different devices. Also, while hysteresis is indeed present in the devices, all threshold voltages were only extracted by scanning from the on-state (positive gate voltage) to the off-state (negative gate voltage) at positive drain voltages.

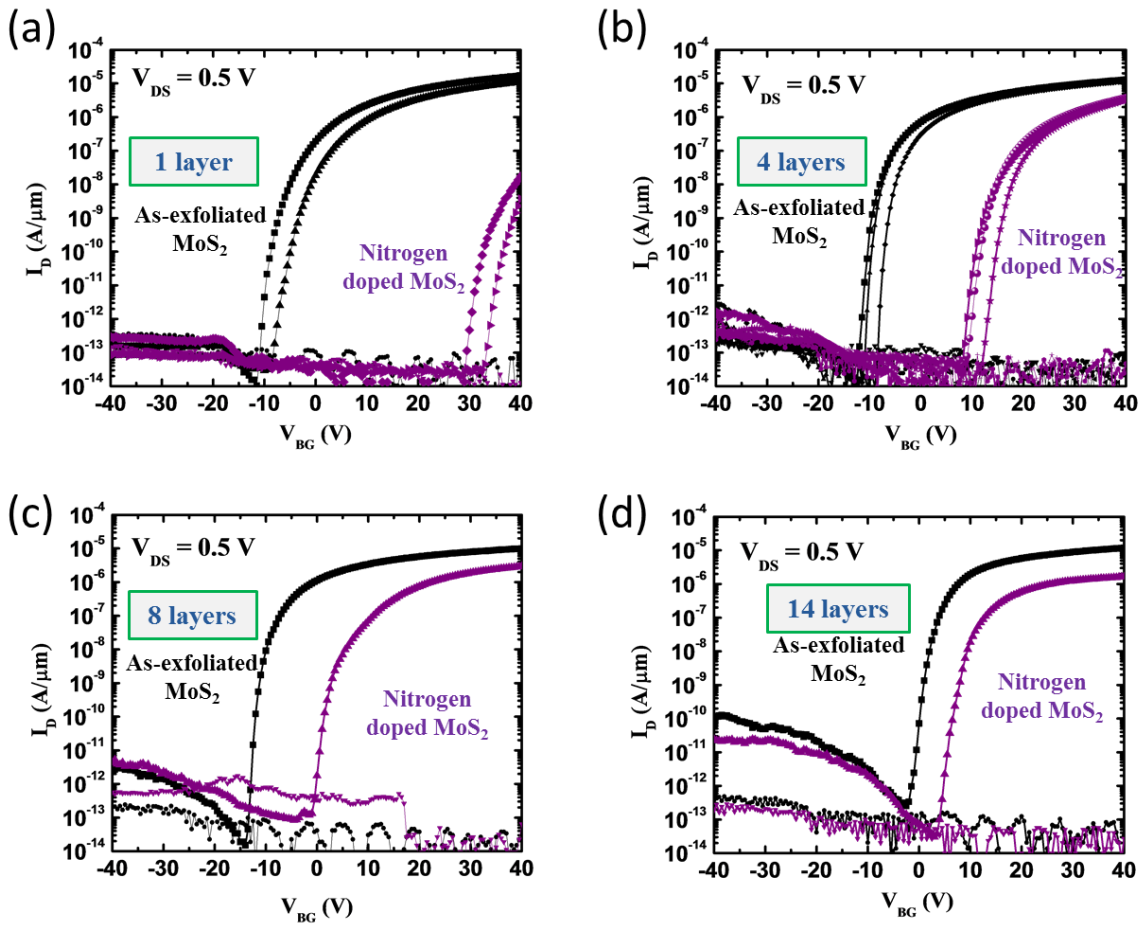

Figure 6.9. I_{DS}-V_{GS} characteristics from MoS_2-based FETs, where the channel thickness corresponds to (a) monolayer, (b) 4 layers, (c) 8 layers, and (d) 14 layers. The curves for as-exfoliated MoS_2 are in black and those for nitrogen doped MoS_2 are presented in purple.

This approach produces device characteristics that are almost identical to what is otherwise only obtained through a pulsed measurement[165] which is known to give rise to almost hysteresis free characteristics. The positive shift of the threshold voltage V_{th} is consistent with the expected p-type dopant behavior of nitrogen in MoS_2.[166] Yet, a p-type branch in the characteristics was not observed, probably due to well-known Fermi level pinning of the metal contacts the near the MoS_2 conduction band.[167]

Interestingly, and in contrast to Nb[54] or NO_2[48] doping, no degenerate doping was observed after N_2 plasma exposure, which highlights the advantage of this process as the control of the device current with the applied voltage was preserved. Furthermore, when correcting for the aforementioned threshold voltage shift, device characteristics in the device ON-state above threshold voltage reached almost identical on-current levels I_{ON}, which suggests that the presence of nitrogen did not enhance scattering so as to reduce the I_{ON} of the transistors.

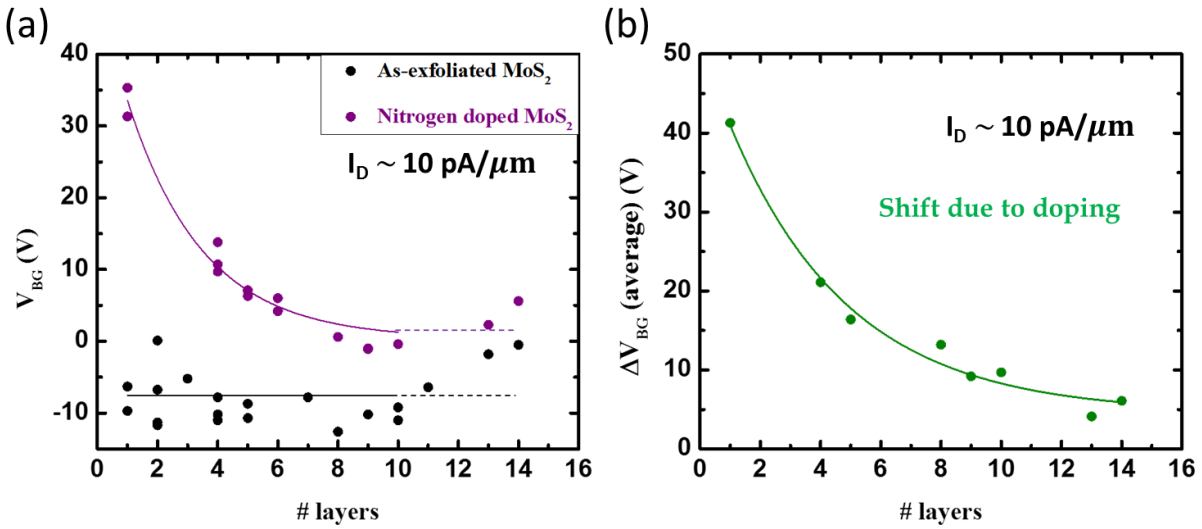

Figure 6.10. Dependence of (a) V_{th} and (b) average V_{th} shift on the layer thickness of as-exfoliated and nitrogen doped MoS_2 at I_D~10 pA/μm. Lines are drawn to guide the eye.

A dependence of the V_{th} shift with layer thickness was also found, as shown in Figure 6.10, where V_{th} increased with decreasing MoS_2 layer thickness. The higher V_{th} shift for mono and few-layer MoS_2 is consistent with an expected higher relative atomic concentration of nitrogen, as compared with thick MoS_2. For thicker MoS_2 (>6 layers), the underlying MoS_2, which is expected to be nitrogen free based on the XPS analysis, will produce the more dominant electrical response. From the V_{th} shift, the p-type doping level (N_A) calculated for the nitrogen

doped MoS_2 ranges from 2.5×10^{18} cm^{-3} to 1.5×10^{19} cm^{-3}, based on a reference value of $N_A \sim 1.5 \times 10^{18}$ cm^{-3} for the as-exfoliated MoS_2.[166] Here, it is worth noting that the XPS measurements indicate that the initial bulk MoS_2 was unintentionally n-type doped, of which the outermost layer was then counter-doped upon N_2 plasma exposure, as shown in Figure 6.7. In the case of the exfoliated MoS_2 used for the electrical characterization presented here, such flakes exhibit an initial p-type doping possibly due to water intercalation,[166] and after nitrogen doping, an increase in the acceptor doping level was generated. Therefore, both measurements support the claim that nitrogen acts as a p-type dopant for MoS_2, which is consistent with the theoretical predictions.[148]

6.4 Implication of Nitrogen Doping in the MoS_2 Structure

The chemical characterization indicates that the N_2 plasma treatment is an effective method for nitrogen doping of MoS_2. However, the use of plasma exposures on the MoS_2 can result in side-effects such as layer etching[141,142] or roughening of the surface.[89,168] To evaluate the effect of the N_2 plasma treatment on the MoS_2 surface topography, atomic force microscopy (AFM) imaging was employed. The initial surface of a MoS_2 flake exfoliated on SiO_2/Si is shown in Figure 6.11, where a step height of ~6 nm was observed for this flake. After 15 min of N_2 plasma exposure, no evidence of layer etching was detected as the height of the step in the flake remained constant, and no additional features which indicate physical damage were present, such as cluster-like particles or etched areas. Instead, the MoS_2 surface remained smooth with a root mean square (RMS) roughness of 0.74 nm. Interestingly, increasing the N_2 plasma exposure time to 60 min causes the development of cracks across the sample surface primarily at the grain boundaries of the MoS_2 surface. The depth of the cracks was ~0.7 nm consistently, suggesting that the crack

formation occurred just within the topmost, N-doped MoS_2 monolayer. The majority of the cracks were connected at an angle of ~120°, where the crack propagation reflected a hexagonal-like symmetry. Interestingly, there was a minimal effect on the surface roughness, indicating that a longer plasma exposure did not cause disruption of the underlying MoS_2 layered structure. Further evidence of the preservation of the layered structure in N_2 plasma treated MoS_2 is provided by cross-section STEM images, shown in Figure 6.11b.

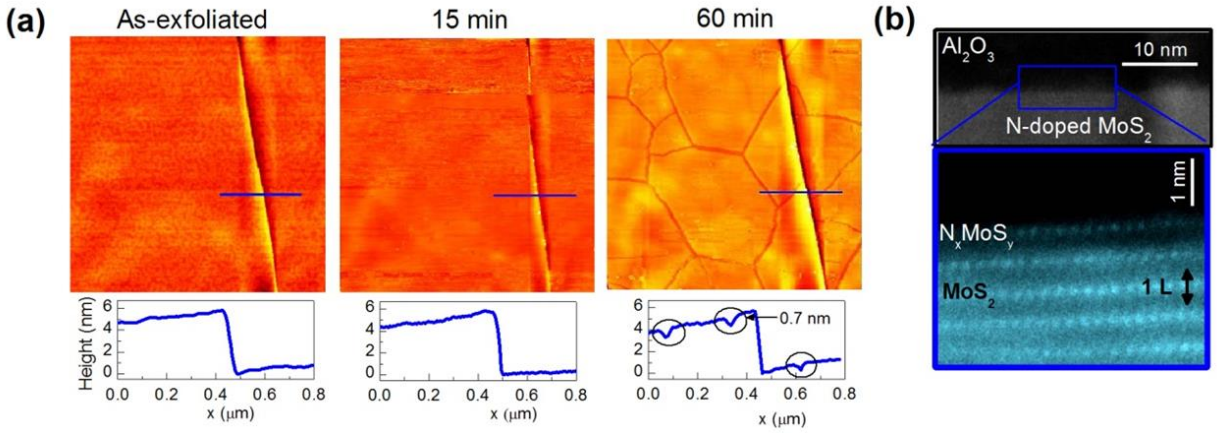

Figure 6.11. (a) AFM images of the surface topography of a MoS_2 flake deposited on a SiO_2/Si substrate, as-exfoliated and after 15 min and 60 min of N_2 plasma exposure. The line profile in blue extends across a MoS_2 step, which height is shown in the bottom graphs. (b) Cross-section STEM images of an N_2 plasma treated MoS_2 samples with an exposure time of 60 min.

The contrast change observed, due to the presence of nitrogen in MoS_2, indicates that the sulfur substitution occurred predominantly within the outermost MoS_2 layer, in agreement with the XPS analysis. Since nitrogen has a smaller atomic radius in comparison to sulfur, its introduction to the MoS_2 lattice and subsequent formation of Mo-N bonds could potentially generate compressive strain, resulting in the development of cracks for a high nitrogen concentration at the surface. To investigate this hypothesis, Raman Spectroscopy on few-layer, exfoliated MoS_2 flakes were carried out. Figure 6.12 shows that the Raman spectra for an exfoliated MoS_2 flake

on SiO_2/Si substrate. The peak separation between the A_{1g} and E^1_{2g} vibrational modes is 21.5 cm^{-1}, which according to the literature corresponds to exfoliated, bilayer MoS_2.[69] After 15 min of the N_2 plasma treatment, the E^1_{2g} peak corresponding to an in-plane vibrational mode blue shifted and split into two peaks, labeled as E^{1+}_{2g} as E^{1-}_{2g}. The E^1_{2g} peak splitting has been correlated to symmetry breaking of this vibrational mode generated due to the presence of strain in the MoS_2 layered structure.[169] The blue shift of the E^1_{2g} mode with respect to the initial exfoliated MoS_2 suggests that that the type of strain generated due to the presence of Mo-N bonding is compressive,[170] which suggests the contraction of the MoS_2 lattice due to the introduction of nitrogen as a dopant.

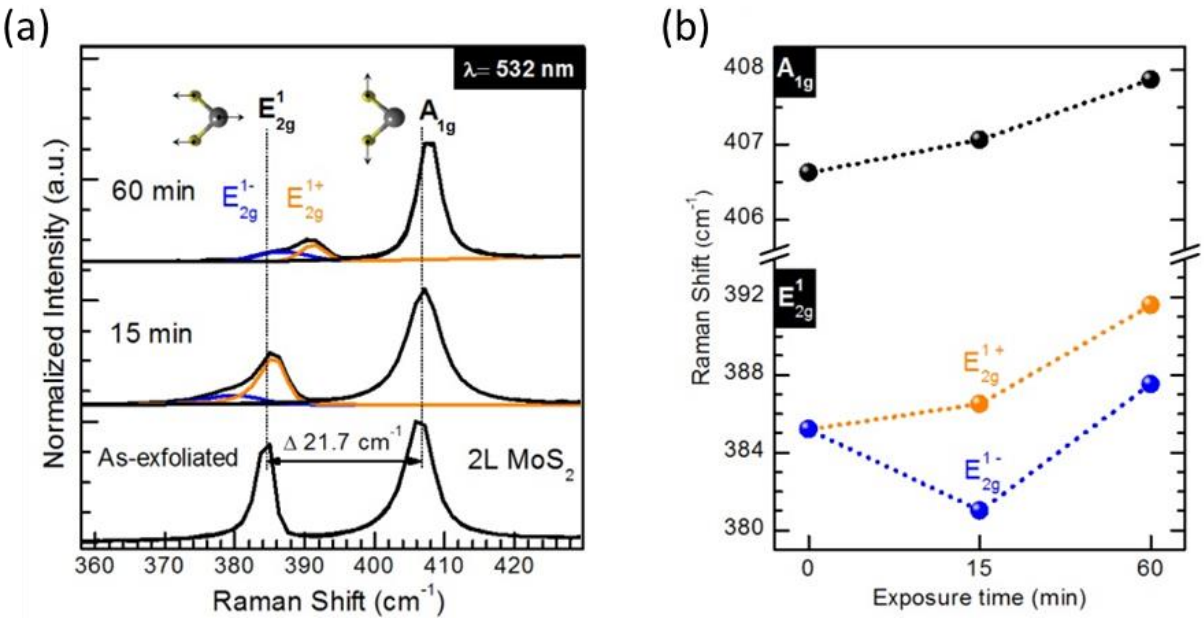

Figure 6.12. Raman spectra from a bilayer MoS_2 flake deposited on a SiO_2/Si substrate, as-exfoliated and after a sequential N_2 plasma exposure of 15 min and 60 min. Raman shift *vs* N_2 exposure time obtained from the measurements shown in (a).

In fact, this situation is analogous to the case of silicon, where local compressive strain is generated due to doping with boron or carbon atoms.[171,172] In addition to the effect of compressive strain for the N-doped MoS_2 system, charge doping effects are likely to contribute to the measured Raman signal, which is translated as a shift of the out-of-plane vibrational mode A_{1g}.[173] Consistent with the p-type doping of MoS_2 given by substitutional nitrogen, the A_{1g} peak blue shifted by 0.43 ± 0.07 cm^{-1} after 15 min of N_2 plasma exposure.

Increasing the N_2 plasma exposure time to 60 min caused a blue shift up to 6.4 cm^{-1} for E_{2g}^{1+} and 1.2 cm^{-1} for A_{1g} with respect to the initial peak positions, as shown in Figure 3c. Additionally, the E_{2g}^{1} peak intensity was significantly reduced, where the E_{2g}^{1} to A_{1g} ratio of the respective integrated intensities decreased by 47% with respect to as-exfoliated MoS_2. The decrease in the E_{2g}^{1}/A_{1g} ratio is an indication of suppression of the in-plane movement related to the E_{2g}^{1} mode, which results from the compressive strain in the MoS_2 structure according to studies on MoS_2 subjected to externally applied pressure.[174] Interestingly, there was a decrease in the FWHM of the A_{1g} feature from 4.5 cm^{-1} for exfoliated MoS_2 to 3.7 cm^{-1} after the 60-minute exposure. According to the dependence of A_{1g} FWHM on the MoS_2 thickness,[69] this decrease in FWHM is an indication of thinning down the effective MoS_2 thickness, from bilayer to monolayer due to a complete sulfur substitution by nitrogen in the top most MoS_2 layer. At this stage, the effect of strain is still present in the remaining bottom MoS_2 layer, which is evidenced by the fact that the A_{1g} and E_{2g}^{1} peaks are blue shifted with respect to the peak positions reported for unstrained monolayer MoS_2.[168] Estimation of compressive strain from the E_{2g}^{1} shift based on models developed for biaxial strain induced by external forces[170] is not feasible for this N-doped bilayer

MoS_2 system since the shifts in the Raman spectra are the convolution of compressive strain and charge doping effects due to sulfur substitution by nitrogen.

In an attempt to estimate the magnitude of strain at different nitrogen concentrations in MoS_2, first principles calculations were performed for the N-doped bilayer MoS_2 system. For these calculations, a 4×4 supercell (12.65 Å × 12.65 Å) of bilayer MoS_2 was used. When a sulfur atom is substituted by a nitrogen atom in MoS_2, the resulting bond length for the covalent Mo-N bond is 2.01 Å whereas that of Mo-S in pristine MoS_2 is 2.41 Å. Therefore, the presence of Mo-N generates a contraction of the MoS_2 lattice, which is in agreement with Raman Spectroscopy measurements. Figure 6.13 shows the percentage of strain for different nitrogen coverages.

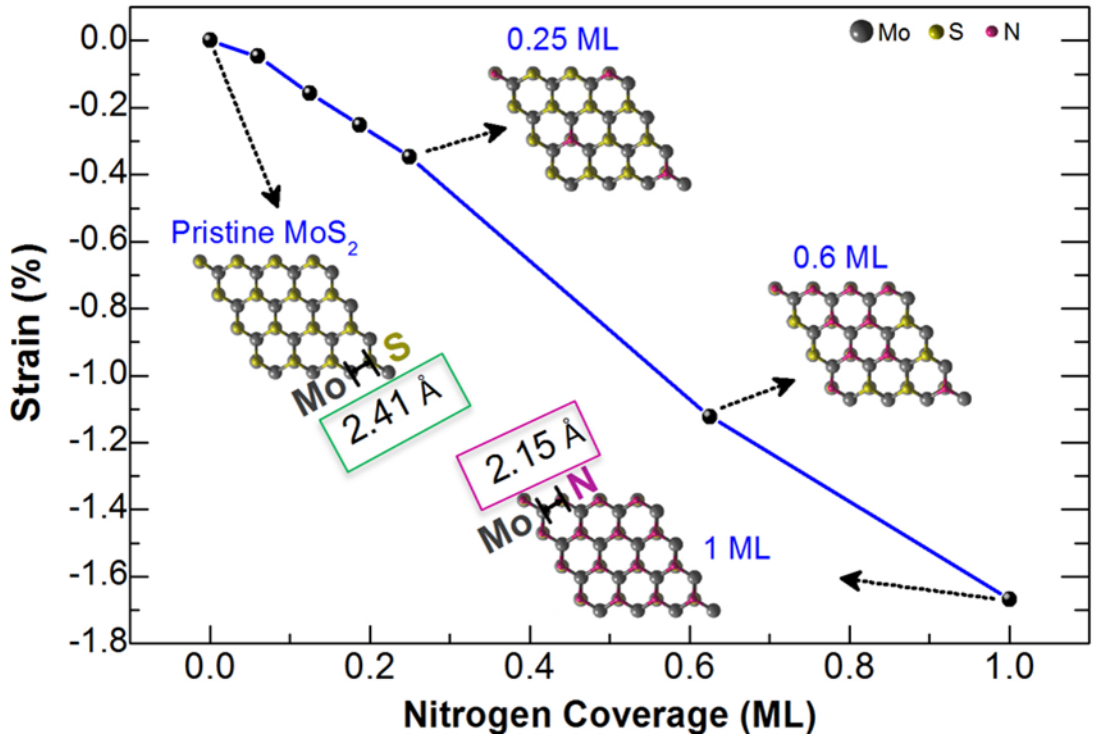

Figure 6.13. Dependence of the compressive strain on the N coverage for bilayer MoS_2 obtained from DFT calculations, where nitrogen is set as a substitutional dopant. The top view of the optimized pristine and nitrogen doped MoS_2 structures are also presented.

The magnitude of strain was calculated as:

$$\varepsilon = (a_N - a_p)/a_p \quad (6.2)$$

Where a_N and a_p (=3.16 Å) are the lattice constant of N-doped MoS_2 and pristine MoS_2, respectively. By correlation of the calculated dependence of compressive strain with N coverage with the experimental XPS data shown earlier, the estimated compressive strain for the different N coverages would correspond to: *t1*= 0.1%, *t2*= 0.5%, *t3*= 1.3%, *t4*= 1.5% and *t5*= 1.7%. According to these calculations, the magnitude of the strain when nitrogen is present as a dopant in MoS_2 is comparable to that obtained from a mechanically induced strain.[175] Based on the DFT calculations, the percentage of compressive strain given by one monolayer coverage of nitrogen in MoS_2 is 1.7%. Experimentally, this amount of strain would correspond to a 60 min N_2 plasma exposure, after which cracking of MoS_2 occurred. It has been reported that the strain required to cause breaking of the MoS_2 structure by mechanical forces is in the range of ~6-11%.[176] Therefore, the estimation of strain given by the presence of Mo-N bonds suggests that the cracking process observed in the outermost MoS_2 layers is not only related to the compressive strain, but also to other factors that can promote crack formation. Recent theoretical calculations have shown that the amount of strain needed to cause cracking of MoS_2 can be reduced by chemical absorption of molecules on the MoS_2 surface since the generation of crack lines results energetically favorable at the adsorption sites during chemisorption.[177] Therefore, the chemical adsorption of nitrogen possibly promotes the cracking process by reducing the amount of strain needed to generate crack lines. Importantly, the experimental evidence of strain induced by single atom doping presented here opens the possibility to identify the window at which doping

concentration and strain can be used to modify the electronic properties of two-dimensional TMDs.

Finally, it should be noted that given the evidence of compressive strain generated in MoS_2 due to nitrogen doping, a band gap change of MoS_2 is not excluded. If the MoS_2 band gap was modified due to strain, that change is expected to have a minimal contribution in the electrical characteristics presented here. The percentage of strain for the nitrogen doped MoS_2-based FET measurements is estimated to be of the order of ~1.3%. According to previous reports, such levels of strain, generated mechanically, can induce a band gap change on the order of ~100 meV or less depending on the MoS_2 layer thickness.[170] While in general a change in bandgap can be extracted from changes in the device characteristics,[178] the absence of clear ambipolar behavior in the case of MoS_2 prevents such an analysis here. However, using the inverse subthreshold slope from the I-V characteristics shown in Figure 6.8 to translate the gate voltage axis into an energy scale, we conclude that a hypothetical increase in the MoS_2 band gap of 100 meV would only explain a change in the threshold voltage of up to 2 V, much smaller than the observed threshold voltage shifts. Therefore the V_{th} shift shown in this work is expected to be dominated by charge doping given by nitrogen. Further studies will be needed to determine possible strain induced band gap tuning of MoS_2 upon nitrogen doping, in a controllable manner.

6.5 Conclusions

In summary, the use of N_2 plasma as a strategy for nitrogen doping of MoS_2 was evaluated in this work. The surface chemistry of MoS_2 upon N_2 plasma treatment indicated that nitrogen forms a covalent bond with molybdenum through chalcogen substitution of S. It was found that the nitrogen concentration in MoS_2 can be controlled with N_2 plasma exposure time. The

electrical characterization shows that nitrogen acts as a substitutional p-type dopant in MoS_2, consistent with theoretical predictions and XPS analysis, while the electrical performance of the nitrogen doped MoS_2 based FETs was preserved in reference to the as-exfoliated MoS_2 based FETs. It was also demonstrated that the doping process through the use of remote N_2 plasma induced compressive strain in MoS_2, and while the layered structure of MoS_2 was not damaged, cracking did occur with significant concentrations of N incorporated. It was shown that nitrogen concentration can be applied to tune the level of compressive strain in MoS_2. This work paves the way for the realization of substitutional covalent doping in two-dimensional materials.

CHAPTER 7

CONCLUSIONS AND FUTURE WORK

In this work, different approaches for the surface modification of layered TMDs were investigated. As presented in Chapter 3, it was found that the UV-O_3 treatment is a practical and non-disruptive route for surface functionalization of MoS_2 while preserving its structural and electronic properties. Additionally, it was demonstrated that the S-O bonds formed upon UV-O_3 treatment on MoS_2 enhance the nucleation of dielectrics during thermal ALD processes. By optimization of the ALD growth on the oxygen functionalized MoS_2 surface, uniform, and thin dielectric films were obtained. The electrical characterization of the HfO_2 film grown by the processes developed here shows promising results when implemented in MoS_2-based FETs, such as low leakage current and good I_{ON}/I_{OFF} ratio. As future work, the effect of thermal annealing under different environments is still to be studied to possibly enhance the dielectric properties of the gate oxide and to reduce D_{it}.

In Chapter 4, significant differences in the reactivity of transition metal diselenides in comparison to MoS_2 were identified upon UV-O_3 treatment. It was found that the surface oxides formed on after UV-O_3 on $MoSe_2$ and WSe_2. Importantly, these surface oxides could be removed from the surface after deposition of HfO_2 by ALD due to a clean-up effect, where the removal was more effective for $MoSe_2$ in comparison to WSe_2. The surface chemistry has an impact on the HfO_2 deposition by ALD, where films were uniform on $MoSe_2$ while triangular islands were obtained on WSe_2. Yet, as shown in Chapter 5, by using an alternative ozone-based ALD

process, the nucleation of Al_2O_3 was enhanced on WSe_2. By the optimization of the deposition temperature, oxidation of WSe_2 during ALD was prevented. The electrical properties of the dielectrics deposited by ozone-based ALD on WSe_2 are to be determined.

Doping of MoS_2 was also an area of study in this work, as presented in Chapter 6. It was found that nitrogen can be introduced in the MoS_2 lattice by remote N_2 plasma exposure, where a substitutional doping mechanism was identified in this process. Furthermore, the remote N_2 plasma did not generate disruption of the layered structure of MoS_2. The electrical characterization provided evidence of the p-type behavior of the nitrogen dopant in MoS_2. Interestingly, the presence of nitrogen induced compressive strain in MoS_2, which was dependent on the atomic nitrogen concentration. This study contributes to the understanding of the chemical and structural implications of substitutional doping in TMD materials. The following steps in this work are the understanding of the effect of nitrogen doping on the MoS_2 bandgap by systematic photoluminescence and scanning tunneling spectroscopy studies since it has been shown that strain can induce bandgap changes in TMDs. Additionally, the use of a high workfunction contact such as MoO_x to enhance the carrier injection in p-type MoS_2 is another proposed work to be carried. Furthermore, this technique for covalent nitrogen doping can also be extended to WSe_2, according to preliminary results, where the electrical results showed a similar p-type doping effect for WSe_2. The future work will be to investigate possible changes in the WSe_2 bandgap due to nitrogen doping, and with a proper design, to implement n-type/p-type heterostructures. Ultimately, it is expected that the processes for dielectric integration and p-type covalent doping of TMDs can be applied in the fabrication of tunneling field effect transistors.

APPENDIX I

UV-O_3 TREATMENT

The UV-O_3 treatment employed in this work for the surface functionalization of TMDs is based on the procedure described by J. R. Vig.[82] The specific set-up and process to perform this surface treatment in the UV-O_3 chamber, which is connected to the UHV cluster tool, is described below.

A. UV-O_3 Chamber Set-Up

The UV-O_3 treatment is performed in the UV-O_3 chamber equipped with a mercury grid lamp (MHK Inc.) for UV radiation, a leak valve that allows the introduction gas into the chamber, and a carousel to place sample plates, as shown in Figure I-1. The power source of the UV-lamp is located next to the UV-O_3 chamber.

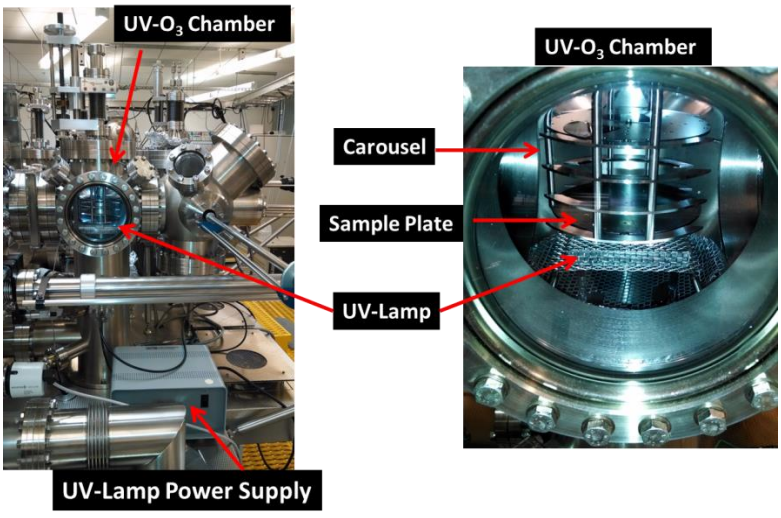

Figure I-1. Front-side configuration of the UV-O_3 chamber.

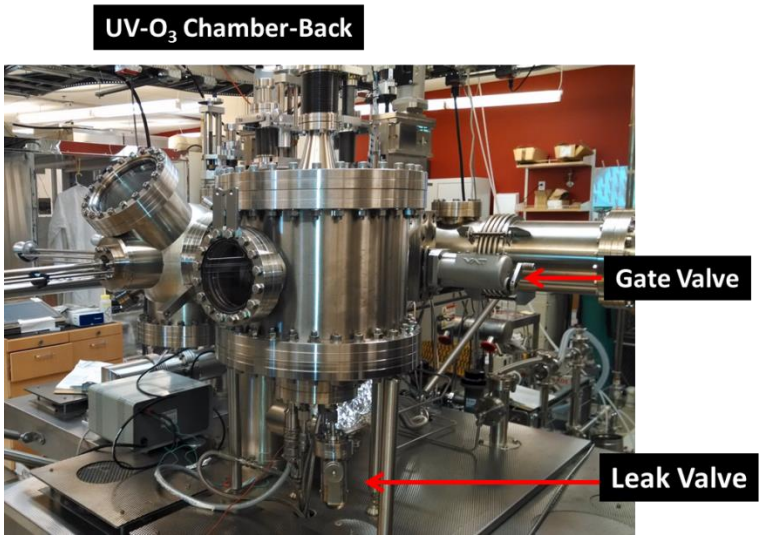

Figure I-2. Back-side configuration of the UV-O_3 chamber.

B. Process

I) Sample Loading and Chamber Preparation

1. Load the sample to be exposed to UV-O_3 on a 4" plate
2. Transfer the sample plate to the UV-O_3 chamber and place the plate facing down on the bottom slot of the carousel.
3. Take out other plates (if any) from the UV-O_3 chamber to avoid the ozone exposure on those samples.
4. Lower down the carousel so that it is within ~0.5 cm close to the grid that contains the UV lamp. The sample should not touch the grid.
5. **CLOSE GATE VALVE BETWEEN THE UV-O_3 CHAMBER AND THE BUFFER CHAMBER**. Check that the fork used to load the samples is all the way out of the chamber before closing this gate valve.

6. **CLOSE TURBO PUMP GATE VALVE**. This allows us to perform the UV-O_3 treatment in a static mode.
7. Check that the power supply is off, and plug in the UV lamp power supply to the adequate voltage source.
8. Pump down the gas line connected to the leak valve.
    a. Connect the turbo pump controller and monitor the rotation speed of the turbo pump.
    b. Open the gas valve that is connected to the turbo pump slowly to pump any residual gas that could be trapped in the gas line. At this point, the gate of the turbo pump should be close, which avoids the background gas to leak into the chamber.
    c. Pump the gas line for about 5 min.
    d. Close the turbo pump gas valve

II) UV-O_3 exposure

9. Open the oxygen gas valve located in the lower left-hand side of the gas manifold
10. Open the main gas valve of the UV-O_3 chamber that connects to the leak valve
11. Leak oxygen in using the leak valve and watch closely the pressure in the gauge.
12. Leak oxygen into the chamber until the pressure reaches a value of 900 mbar. Once such pressure is read, close the leak valve.
13. Close the oxygen gas and the main UV-O_3 chamber gas valve.
14. Set the timer. A 15 minutes exposure is the standard time needed for an oxygen coverage of ~1 ML on MoS_2

15. Turn on the UV lamp and start the timer.

16. Once the treatment time is finished, turn off the UV lamp

II) Pumping down UV-O_3 chamber:

17. To pump down the UV-O_3 chamber:

    a. Isolate the turbo pump from the roughing pump by closing the gate between these two (located next to the turbo pump)

    b. Open the valve that connects to the roughing pump and watch the pressure of the chamber which should start to drop

    c. Once the pressure reaches ~$2x10^{-2}$ mbar, close the roughing pump valve.

    d. Open the gate between the turbo and roughing pump.

    e. Open the gate valve of the turbo pump

18. Wait for the pressure to reach 1.0 $x10^{-7}$ mbar or lower, and then open the gate of the UV-O_3 chamber to transfer the sample out.

APPENDIX II

REMOTE N_2 PLASMA EXPOSURE

In this appendix, the detailed description of the surface treatment for nitrogen doping of MoS_2 is presented. All the remote N_2 plasma exposures were performed using the remote RF-plasma source of the sputtering chamber in the UHV cluster tool.

A. Sputtering Chamber Set-Up

The sputtering chamber set-up is shown in Figure II-1.

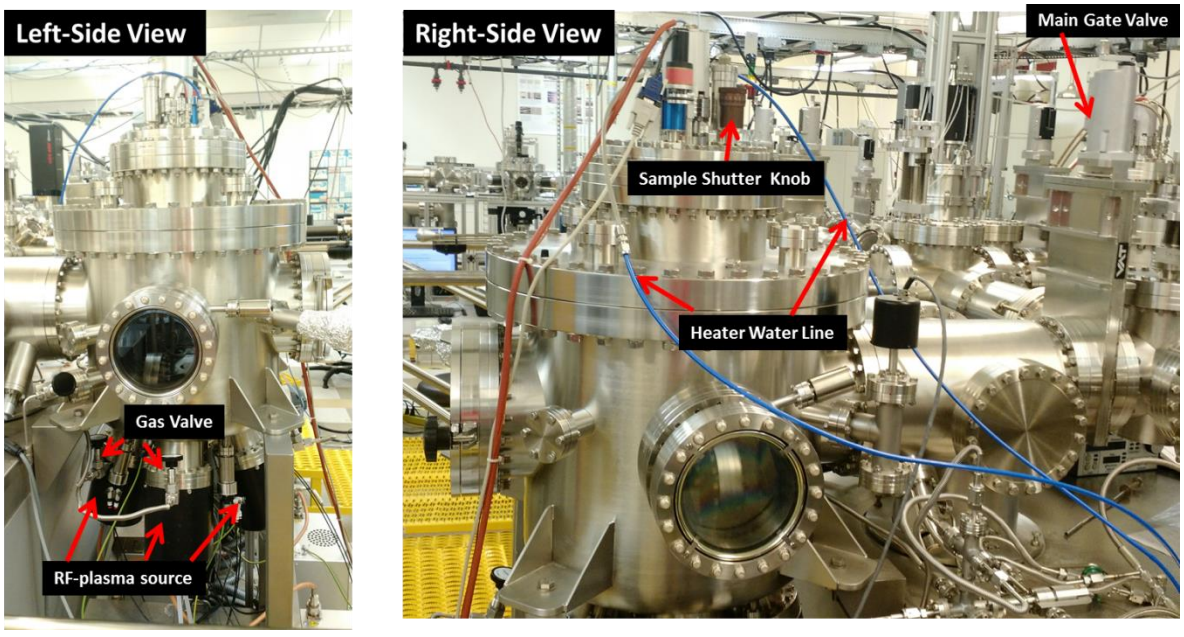

Figure II-1. Sputtering chamber interconnected to the UHV cluster system.

The sputtering chamber contains four RF-plasma sources for sputtering deposition of metals. In this study, the N_2 plasma exposures were performed at relatively low power (100 W) and having all shutters closed, the metal targets shutters and the sample shutter so that the metal deposition was prevented. The gas lines to RF-plasma source is connected to mass flow controllers and water lines are also connected to the RF-plasma system for cooling purposes. Additionally, the sputtering chamber is equipped with a Pt-heater for annealing purposes through heat transfer. The temperature set in the heater controller was calibrated using a Si wafer-thermocouple that is placed in direct contact to the heater.

SAFETY NOTE: Be aware of all gas connections to the chamber. Do NOT enable explosive mixtures of gasses to be admitted into the chamber, such as forming gas and O_2!

B. Process

I) Sample Loading and Pre-Annealing

1. Load into the UHV system the sample to be treated on a 4" Ti plate using Mo screws
2. Transfer the sample plate (facing down) to the sputtering chamber
3. Check that the water line to the heater is open
4. Ramp up the temperature in the heater controller up to 330 °C for an actual temperature of 300 °C. Monitor the current applied to the heater so that this does not exceed 10 A. Ramp up the temperature in stepwise so that the pressure in the chamber does not exceed 2×10^{-7} mbar.
5. Anneal for two hours at the set temperature of 330 °C
6. Before the annealing duration time is complete, prepare for the N_2 plasma exposure.
    a. Open the N_2 and Ar valves in the gas manifold

b. Open the water line to the RF-plasma source

II) N_2 Plasma Exposure

1. After the two-hour anneal, keep the heater temperature at 300 °C (controller T: 330 °C)
2. Set the turbo pump to stand-by mode (it takes ~3-5 minutes to reach 345 Hz)
3. Turn the ion gauge emission control OFF
4. Open the gas valve of the selected RF-plasma source [typically source 412 (Hf)] and pump the gas line, while monitoring the pirani gauge. Keep the gas valve open after pumping it.
5. Close the adaptive pressure gate valve ("butterfly gate") by pressing first "ZERO" and then "CLOSE".

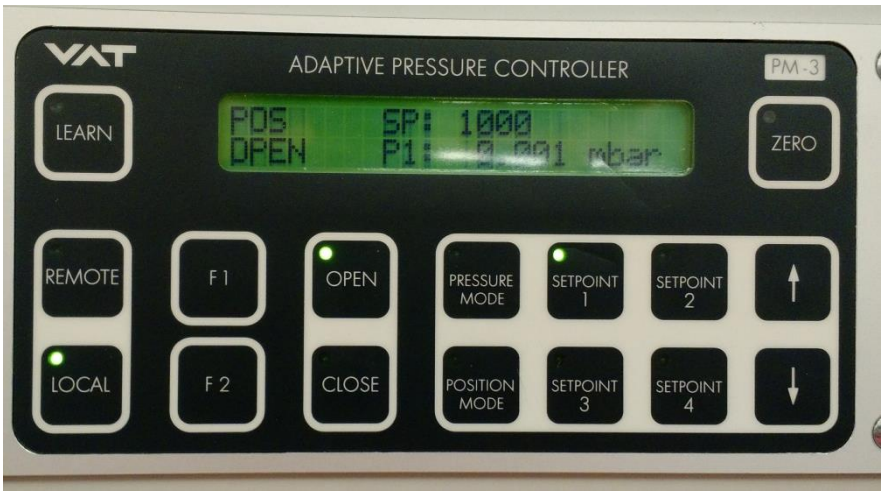

Figure II-2. Adaptive pressure controller of the sputtering chamber.

6. Check that the sample shutter is closed, and all the shutters of the metal targets in the sputter sources are closed. Also, CLOSE the shutters of the chamber windows.

7. Switch the RF-power generator knob ON. If no water is flowing, the screen will show an interlock error. Then, set the RF power to 200 W. (See Fig II-3(b)).
8. In the mass flow controller screen, set Channel 1 (Ar) to 60 sccm and Channel 3 (N_2) to 45 sccm. Verify that the flow set for Channel 2 (O_2) and Channel 4 (N_2/H_2) is 0 sccm. (See Fig. II-3(a) below).
9. Leak the gas into the chamber by setting the "status" of Channels 1 and Channel 3 to "ON". Then, press "ON" and "ALL".
10. At this point the lower message should read "FLOW ON GAS ON", and the pressure should rise up to ~4×10^{-2} mbar in the adaptive pressure controller.
11. Press the "ON" pad of the RF-plasma generator, and wait until the reflected power goes down to 0 W. At this point the plasma should be on. If the error message "overload" appears, increase the Ar flow to 80 sccm or alternatively, increase the power to 220 W, and wait for the reflected power to reach zero.
12. Immediately after the reflected power reaches zero, reduce RF-power to 100 W, and turn off the flow of Channel 1 (Ar).
13. Set the desired exposure time; see plot of nitrogen concentration in MoS_2 *vs* time in Figure 6.3 (Chapter 6).
14. During the N_2 plasma exposure, the mass-flow controller screen and RF-power generation should read as Figure II-3. Also, the color of the N_2 plasma in the sputtering chamber should look as in figure II-4, consistent with N_2 ionization.

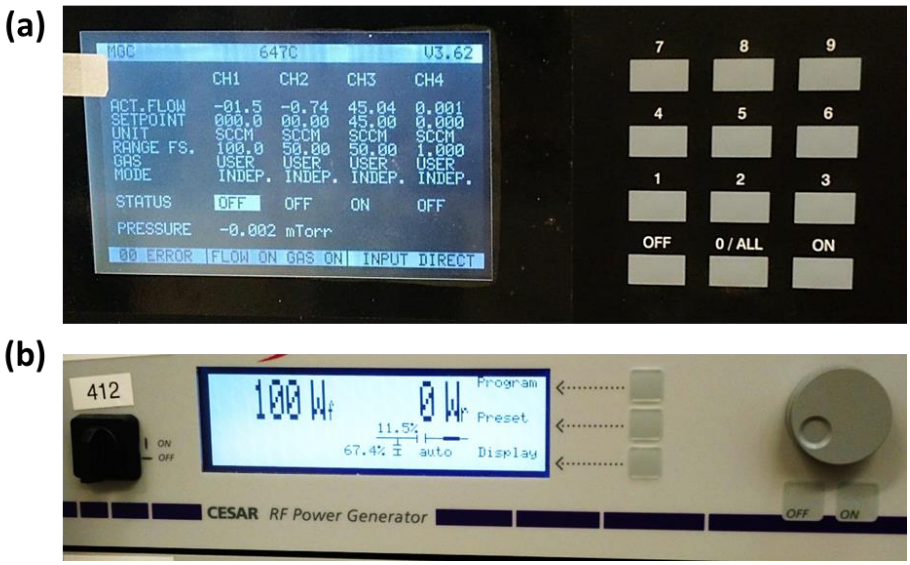

Figure II-3. (a) Mass-flow controller screen and (b) RF-power supply showing the parameters during the N_2 plasma exposure.

15. Press "pressure mode" in the adaptive pressure controller. After this step, the pressure should be regulated to ~7×10^{-3} mbar.
16. Once the plasma exposure time is up, press the OFF pad on in the RF-power generator and switch the knob of this generator OFF.
17. Close the N_2 gas by pressing "OFF" and "ALL" in the gas flow controller screen.

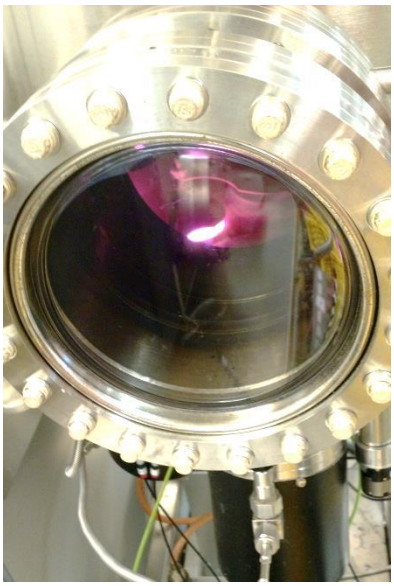

Figure II-4. Afterglow plasma color during a typical N_2 plasma exposure.

III) Pumping Down the Sputtering Chamber:

1. Press “OPEN” in the adaptive pressure controller to open the butterfly gate valve.
2. Close the gas valve connected to the RF-plasma source.
3. Set the turbo pump to 100 % rotation by pressing the stand-by button. The rotation should be recovered to 660 Hz.
4. Close the gas valves in the gas manifold.
5. Close the water line to the RF-plasma source.
6. Once the rotation reached 660 Hz, turn on the ion gauge to read the pressure.
7. Reduce the temperature to room temperature stepwise in steps of 50 °C every 10 min.
8. Wait until the pressure recovers to ~1×10^{-8} mbar to take the sample plate out.

REFERENCES

(1) Novoselov, K. S. Electric Field Effect in Atomically Thin Carbon Films. *Science* **2004**, *306*, 666–669.

(2) Mayorov, A. S.; Gorbachev, R. V; Morozov, S. V; Britnell, L.; Jalil, R.; Ponomarenko, L. A; Blake, P.; Novoselov, K. S.; Watanabe, K.; Taniguchi, T.; *et al.* Micrometer-Scale Ballistic Transport in Encapsulated Graphene at Room Temperature. *Nano Lett.* **2011**, *11*, 2396–2399.

(3) Radisavljevic, B.; Radenovic, A.; Brivio, J.; Giacometti, V.; Kis, A.. Single-Layer MoS_2 Transistors. *Nat. Nanotechnol.* **2011**, *6*, 147–150.

(4) Yun, W. S.; Han, S. W.; Hong, S. C.; Kim, I. G.; Lee, J. D. Thickness and Strain Effects on Electronic Structures of Transition Metal Dichalcogenides: 2H-MX_2 Semiconductors (M = Mo, W; X = S, Se, Te). *Phys. Rev. B* **2012**, *85*, 33305.

(5) Chhowalla, M.; Shin, H. S.; Eda, G.; Li, L.-J.; Loh, K. P.; Zhang, H. The Chemistry of Two-Dimensional Layered Transition Metal Dichalcogenide Nanosheets. *Nat. Chem.* **2013**, *5*, 263–275.

(6) Han, S. A.; Bhatia, R.; Kim, S.-W. Synthesis, Properties and Potential Applications of Two-Dimensional Transition Metal Dichalcogenides. *Nano Converg.* **2015**, *2*, 17.

(7) Wang, Q. H.; Kalantar-Zadeh, K.; Kis, A.; Coleman, J. N.; Strano, M. S. Electronics and Optoelectronics of Two-Dimensional Transition Metal Dichalcogenides. *Nat. Nanotechnol.* **2012**, *7*, 699–712.

(8) KC, S.; Longo, R. C.; Wallace, R. M.; Cho, K. Surface Oxidation Energetics and Kinetics on MoS_2 Monolayer. *J. Appl. Phys.* **2015**, *117*, 135301.

(9) Kumar, A.; Ahluwalia, P. K. Electronic Structure of Transition Metal Dichalcogenides Monolayers 1H-MX_2 (M = Mo, W; X = S, Se, Te) from Ab-Initio Theory: New Direct Band Gap Semiconductors. *Eur. Phys. J. B* **2012**, *85*, 186.

(10) Mak, K. F.; Lee, C.; Hone, J.; Shan, J.; Heinz, T. F. Atomically Thin MoS_2 : A New Direct-Gap Semiconductor. *Phys. Rev. Lett.* **2010**, *105*, 136805.

(11) McDonnell, S.; Brennan, B.; Azcatl, A.; Lu, N.; Dong, H.; Buie, C.; Kim, J.; Hinkle, C. L.; Kim, M. J.; Wallace, R. M. HfO_2 on MoS_2 by Atomic Layer Deposition: Adsorption

Mechanisms and Thickness Scalability. *ACS Nano* **2013**, *7*, 10354–10361.

(12) Tongay, S.; Zhou, J.; Ataca, C.; Lo, K.; Matthews, T. S.; Li, J.; Grossman, C.; Wu, J. Thermally Driven Crossover from Indirect toward Direct Bandgap in 2D Semiconductors: $MoSe_2$ versus MoS_2. *Nano Lett.* **2012**, 12, 5576–5580.

(13) El-Mahalawy, S. H.; Evans, B. L. Temperature Dependence of the Electrical Conductivity and Hall Coefficient in 2H-MoS_2, $MoSe_2$, WSe_2, and $MoTe_2$. *Phys. Status Solidi* **1977**, *79*, 713–722.

(14) Boeker, T.; Severin, R.; Mueller, A.; Janowitz, C.; Manzke, R.; Voss, D.; Krueger, P.; Mazur, A.; Pollmann, J. Band Structure of MoS_2, $MoSe_2$, and Alpha-$MoTe_2$: Angle-Resolved Photoelectron Spectroscopy and Ab-Initio Calculations. *Phys. Rev. Lett.* **2001**, *64*, 235305.

(15) Gutiérrez, H. R.; Perea-López, N.; Elías, A. L.; Berkdemir, A.; Wang, B.; Lv, R.; López-Urías, F.; Crespi, V. H.; Terrones, H.; Terrones, M. Extraordinary Room-Temperature Photoluminescence in Triangular WS_2 Monolayers. *Nano Lett.* **2013**, *13*, 3447–3454.

(16) Yousefi, G. H. Optical Properties of Mixed Transition Metal Dichalcogenide Crystals. *Mater. Lett.* **1989**, *9*, 38–40.

(17) Nicolosi, V.; Chhowalla, M.; Kanatzidis, M. G.; Strano, M. S.; Coleman, J. N. Liquid Exfoliation of Layered Materials. *Science* **2013**, *340*, 1226419–1226419.

(18) Lin, Y.-C.; Lu, N.; Perea-Lopez, N.; Li, J.; Lin, Z.; Peng, X.; Lee, C. H.; Sun, C.; Calderin, L.; Browning, P. N.; *et al.* Direct Synthesis of van Der Waals Solids. *ACS Nano* **2014**, *8*, 3715–3723.

(19) Yue, R.; Barton, A. T.; Zhu, H.; Azcatl, A.; Pena, L. F.; Wang, J.; Peng, X.; Lu, N.; Cheng, L.; Addou, R.; *et al.* $HfSe_2$ Thin Films: 2D Transition Metal Dichalcogenides Grown by Molecular Beam Epitaxy. *ACS Nano* **2015**, *9*, 474–480.

(20) Vishwanath, S.; Liu, X.; Rouvimov, S.; Mende, P. C.; Azcatl, A.; McDonnell, S.; Wallace, R. M.; Feenstra, R. M.; Furdyna, J. K.; Jena, D.; *et al.* Comprehensive Structural and Optical Characterization of MBE Grown $MoSe_2$ on Graphite, CaF_2 and Graphene. *2D Mater.* **2015**, *2*, 24007.

(21) Lin, Y.-C.; Zhang, W.; Huang, J.-K.; Liu, K.-K.; Lee, Y.-H.; Liang, C.-T.; Chu, C.-W.; Li, L.-J.; Novoselov, K.; Jiang, D.; *et al.* Wafer-Scale MoS_2 Thin Layers Prepared by MoO_3 Sulfurization. *Nanoscale* **2012**, *4*, 6637.

(22) Latorre-Sánchez, M.; Esteve-Adell, I.; Primo, A.; García, H. Innovative Preparation of MoS_2-Graphene Heterostructures Based on Alginate Containing $(NH_4)_2MoS_4$ and Their Photocatalytic Activity for H_2 Generation. *Carbon N. Y.* **2015**, *81*, 587–596.

(23) Serna, M. I.; Yoo, S. H.; Moreno, S.; Xi, Y.; Oviedo, J. P.; Choi, H.; Alshareef, H. N.; Kim, M. J.; Minary-Jolandan, M.; Quevedo-Lopez, M. A. Large-Area Deposition of MoS_2 by Pulsed Laser Deposition with in Situ Thickness Control. *ACS Nano* **2016**, *10*, 6054–6061.

(24) Jang, Y.; Yeo, S.; Lee, H. B. R.; Kim, H.; Kim, S. H. Wafer-Scale, Conformal and Direct Growth of MoS_2 Thin Films by Atomic Layer Deposition. *Appl. Surf. Sci.* **2016**, *365*, 160–165.

(25) Iwai, H. Roadmap for 22nm and beyond. *Microelectron. Eng.* **2009**, *86*, 1520–1528.

(26) Schroder, D. K. *Semiconductor Material And Device Characterization*; 3rd Edition; Wiley-IEEE Press: New York, 2006.

(27) Ionescu, A. M.; Riel, H. Tunnel Field-Effect Transistors as Energy-Efficient Electronic Switches. *Nature* **2011**, *479*, 329–337.

(28) Avci, U. E.; Morris, D. H.; Young, I. A. Tunnel Field-Effect Transistors: Prospects and Challenges. *IEEE J. Electron Devices Soc.* **2015**, *3*, 88–95.

(29) Seabaugh, A. C.; Zhang, Q. Low-Voltage Tunnel Transistors for Beyond CMOS Logic. *Proc. IEEE* **2010**, *98*, 2095–2110.

(30) Jena, D. Tunneling Transistors Based on Graphene and 2-D Crystals. *Proc. IEEE* **2013**, *101*, 1585–1602.

(31) Chhowalla, M.; Jena, D.; Zhang, H. Two-Dimensional Semiconductors for Transistors. *Nat. Rev. Mater.* **2016**, *1*, 16052.

(32) Addou, R.; Colombo, L.; Wallace, R. M. Surface Defects on Natural MoS_2. *ACS Appl. Mater. Interfaces* **2015**, *7*, 11921–11929.

(33) Li, M. O.; Esseni, D.; Nahas, J. J.; Jena, D.; Xing, H. G. Two-Dimensional Heterojunction Interlayer Tunneling Field Effect Transistors (Thin-TFETs). *IEEE J. Electron Devices Soc.* **2015**, *3*, 200–207.

(34) Sarkar, D.; Xie, X.; Liu, W.; Cao, W.; Kang, J.; Gong, Y.; Kraemer, S.; Ajayan, P. M.; Banerjee, K. A Subthermionic Tunnel Field-Effect Transistor with an Atomically Thin Channel. *Nature* **2015**, *526*, 91–95.

(35) McDonnell, S.; Addou, R.; Buie, C.; Wallace, R. M.; Hinkle, C. L. Defect-Dominated Doping and Contact Resistance in MoS_2. *ACS Nano* **2014**, *8*, 2880–2888.

(36) Masel, R. I. *Principles of Adsorption and Reaction on Solid Surfaces*; John Wiley & Sons, Inc.: New York, 1996.

(37) Gilman, J. J. Direct Measurements of the Surface Energies of Crystals. *J. Appl. Phys.* **1960**, *31*, 2208–2218.

(38) Kissinger, G.; Kissinger, W. Hydrophilicity of Silicon Wafers for Direct Bonding. *Phys. Status Solidi* **1991**, *123*, 185–192.

(39) Xu, M.; Liang, T.; Shi, M.; Chen, H. Graphene-like Two-Dimensional Materials. *Chem. Rev.* **2013**, *113*, 3766–3798.

(40) Kozbial, A.; Gong, X.; Liu, H.; Li, L. Understanding the Intrinsic Water Wettability of Molybdenum Disulfide MoS_2. *Langmuir* **2015**, *31*, 8429–8435.

(41) Gaur, A. P. S.; Sahoo, S.; Ahmadi, M.; Dash, S. P.; Guinel, M. J.-F.; Katiyar, R. S. Surface Energy Engineering for Tunable Wettability through Controlled Synthesis of MoS_2. *Nano Lett.* **2014**, *14*, 4314–4321.

(42) Yang, J.; Kim, S.; Choi, W.; Park, S. H.; Jung, Y.; Cho, M.-H.; Kim, H. Improved Growth Behavior of Atomic-Layer-Deposited High-k Dielectrics on Multilayer MoS_2 by Oxygen Plasma Pretreatment. *ACS Appl. Mater. Interfaces* **2013**, *5*, 4739–4744.

(43) Cheng, L.; Qin, X.; Lucero, A. T.; Azcatl, A.; Wallace, R. M.; Cho, K.; Kim, J. Atomic Layer Deposition of a High-k Dielectric on MoS_2 Using Trimethylaluminum and Ozone. *ACS Appl. Mater. Interfaces* **2014**, 6, 11834–11838.

(44) McIntyre, N. S.; Spevack, P. A.; Beamson, G.; Briggs, D. Effects of Argon Ion Bombardment on Basal Plane and Polycrystalline MoS_2. *Surf. Sci.* **1990**, *237*.

(45) Liu, Y.; Nan, H.; Wu, X.; Pan, W.; Wang, W.; Bai, J.; Zhao, W.; Sun, L. Layer-by-Layer Thinning of MoS_2 by Plasma. **2013**, 4202–4209.

(46) Zhu, H.; Qin, X.; Cheng, L.; Azcatl, A.; Kim, J.; Wallace, R. M. Remote Plasma Oxidation and Atomic Layer Etching of MoS_2. *ACS Appl. Mater. Interfaces* **2016**, *8*, 19119–19126.

(47) Ilatikhameneh, H.; Tan, Y.; Novakovic, B.; Klimeck, G.; Rahman, R.; Appenzeller, J. Tunnel Field-Effect Transistors in 2-D Transition Metal Dichalcogenide Materials. *IEEE J. Explor. Solid-State Comput. Devices Circuits* **2015**, *1*, 12–18.

(48) Fang, H.; Chuang, S.; Chang, T. C.; Takei, K.; Takahashi, T.; Javey, A. High-Performance Single Layered WSe_2 p-FETs with Chemically Doped Contacts. *Nano Lett.* **2012**, *12*, 3788–3792.

(49) Du, Y.; Liu, H.; Neal, A. T.; Si, M.; Ye, P. D. Molecular Doping of Multilayer MoS_2 Field-Effect Transistors: Reduction in Sheet and Contact Resistances. *IEEE Electron Device Lett.* **2013**, *34*, 1328–1330.

(50) Kiriya, D.; Tosun, M.; Zhao, P.; Kang, J. S.; Javey, A. Air-Stable Surface Charge Transfer Doping of MoS_2 by Benzyl Viologen. *J. Am. Chem. Soc.* **2014**, *136*, 7853–7856.

(51) Xu, H.; Fathipour, S.; Kinder, E. W.; Seabaugh, A. C.; Fullerton-Shirey, S. K. Reconfigurable Ion Gating of 2H-$MoTe_2$ Field-Effect Transistors Using Poly(ethylene Oxide)-$CsClO_4$ Solid Polymer Electrolyte. *ACS Nano* **2015**, *9*, 4900–4910.

(52) Zhang, Y. J.; Ye, J. T.; Yomogida, Y.; Takenobu, T.; Iwasa, Y. Formation of a Stable P – N Junction in a Liquid-Gated MoS_2 Ambipolar Transistor. *Nano Lett.* **2013**, *13*, 3023–3028.

(53) Allain, A.; Kis, A. Electron and Hole Mobilities in Single-Layer WSe_2. *ACS Nano* **2014**, *8*, 7180–7185.

(54) Suh, J.; Park, T.-E.; Lin, D.; Fu, D.; Park, J.; Jung, H. J.; Chen, Y.; Ko, C.; Jang, C.; Sun, Y.; *et al.* Doping against the Native Propensity of MoS_2: Degenerate Hole Doping by Cation Substitution. *Nano Lett.* **2014**, *14*, 6976–6982.

(55) Laskar, M. R.; Nath, D. N.; Ma, L.; Lee, E. W.; Lee, C. H.; Kent, T.; Yang, Z.; Mishra, R.; Roldan, M. A.; Idrobo, J.-C.; *et al.* P-Type Doping of MoS_2 Thin Films Using Nb. *Appl. Phys. Lett.* **2014**, *104*, 92104.

(56) Gong, Y.; Liu, Z.; Lupini, A. R.; Shi, G.; Lin, J.; Najmaei, S.; Lin, Z.; Elías, A. L.; Berkdemir, A.; You, G.; *et al.* Band Gap Engineering and Layer-by-Layer Mapping of Selenium-Doped Molybdenum Disulfide. *Nano Lett.* **2014**, *14*, 442–449.

(57) Zhang, K.; Feng, S.; Wang, J.; Azcatl, A.; Lu, N.; Addou, R.; Wang, N.; Zhou, C.; Lerach, J.; Bojan, V.; *et al.* Manganese Doping of Monolayer MoS_2 : The Substrate Is Critical. *Nano Lett.* **2015**, *15*, 6586–6591.

(58) Briggs D. and Seah M. P. *Practical Surface Analysis in Auger and X-Ray Photoelectron Spectroscopy*; John Wiley & Sons: New York; 1983; pp. 397–427.

(59) Alford, T. L.; Feldman, L. C.; Mayer, J. W. *Fundamentals of Nanoscale Film Analysis*; Springer US: Boston, MA, 2007.

(60) Gilmore, J. C. V. and I. S. *Surface Analysis– The Principal Techniques*; Vickerman, J. C.; Gilmore, I. S., Eds.; John Wiley & Sons, Ltd: Chichester, UK, 2009.

(61) Scofield, J. H. Hartree-Slater Subshell Photoionization Cross-Sections at 1254 and 1487 eV. *J. Electron Spectros. Relat. Phenomena* **1976**, *8*, 129–137.

(62) Reilman, R. F.; Msezane, A.; Manson, S. T. Relative Intensities in Photoelectron Spectroscopy of Atoms and Molecules. *J. Electron Spectros. Relat. Phenomena* **1976**, *8*, 389–394.

(63) Moulder, J. F.; Stickle, W. F.; Sobol, P. E.; Bomben, K. D. Handbook of X-Ray Photoelectron Spectroscopy. *Surface And Interface Analysis*, 1979, *3*.

(64) Sardela, M. *Practical Materials Characterization*; Ed.; Springer New York: New York, NY, 2014.

(65) E2108-10, A. Standard Practice for Calibration of the Electron Binding-Energy Scale of an X-Ray Photoelectron Spectrometer. In; ASTM International: West Conshohocken, PA, 2010.

(66) Herrera-Gómez, A.; Hegedus, A.; Meissner, P. L. Chemical Depth Profile of Ultrathin Nitrided SiO_2 Films. *Appl. Phys. Lett.* **2002**, *81*, 1014.

(67) Leng, Y. *Materials Characterization: Introduction to Microscopic and Spectroscopic Methods*; John Wiley & Sons, Ltd: Chichester, UK, 2008.

(68) Li, H.; Zhang, Q.; Yap, C. C. R.; Tay, B. K.; Edwin, T. H. T.; Olivier, A.; Baillargeat, D. From Bulk to Monolayer MoS_2: Evolution of Raman Scattering. *Adv. Funct. Mater.* **2012**, *22*, 1385–1390.

(69) Lee, C.; Yan, H.; Brus, L. E.; Heinz, T. F.; Hone, J.; Ryu, S. Anomalous Lattice Vibrations of Single- and Few-Layer MoS_2. *ACS Nano* **2010**, *4*, 2695–2700.

(70) Giannuzzi, L. A.; Stevie, F. A. A Review of Focused Ion Beam Milling Techniques for TEM Specimen Preparation. *Micron* **1999**, *30*, 197–204.

(71) Parr, R. G.; Weitao, Y. *Density-Functional Theory of Atoms and Molecules*; Oxford University Press: New York, Oxford, 1989.

(72) Griffiths, D. J. *Introduction to Quantum Mechanics*; 2nd edition.; Pearson Prentice Hall: New Jersey, 2005.

(73) Kresse, G.; Furthmüller, J. Efficiency of Ab-Initio Total Energy Calculations for Metals and Semiconductors Using a Plane-Wave Basis Set. *Comput. Mater. Sci.* **1996**, *6*, 15–50.

(74) George, S. M. Atomic Layer Deposition: An Overview. *Chem. Rev.* **2010**, *110*, 111–131.

(75) Leskelä, M.; Ritala, M. Atomic Layer Deposition (ALD): From Precursors to Thin Film Structures. *Thin Solid Films* **2002**, *409*, 138–146.

(76) Bao, W.; Cai, X.; Kim, D.; Sridhara, K.; Fuhrer, M. S. High Mobility Ambipolar MoS_2 Field-Effect Transistors: Substrate and Dielectric Effects. *Appl. Phys. Lett.* **2013**, *102*, 42104.

(77) Kim, S.; Konar, A.; Hwang, W.-S.; Lee, J. H.; Lee, J.; Yang, J.; Jung, C.; Kim, H.; Yoo, J.-B.; Choi, J.-Y.; *et al.* High-Mobility and Low-Power Thin-Film Transistors Based on

Multilayer MoS_2 Crystals. *Nat. Commun.* **2012**, *3*, 1011.

(78) Liu, H.; Ye, P. D. MoS_2 Dual-Gate MOSFET with Atomic-Layer-Deposited Al_2O_3 as Top-Gate Dielectric. *IEEE Electron Device Lett.* **2012**, *33*, 546–548.

(79) Das, S.; Chen, H.-Y.; Penumatcha, A. V.; Appenzeller, J. High Performance Multilayer MoS_2 Transistors with Scandium Contacts. *Nano Lett.* **2013**, *13*, 100–105.

(80) Jena, D.; Konar, A. Enhancement of Carrier Mobility in Semiconductor Nanostructures by Dielectric Engineering. *Phys. Rev. Lett.* **2007**, *98*, 136805.

(81) Liu, H.; Xu, K.; Zhang, X.; Ye, P. D. The Integration of High-k Dielectric on Two-Dimensional Crystals by Atomic Layer Deposition. *Appl. Phys. Lett.* **2012**, *100*, 152115.

(82) Vig, J. R. UV/ozone Cleaning of Surfaces. *J. Vac. Sci. Technol. A Vacuum, Surfaces, Film.* **1985**, *3*, 1027.

(83) Brown, N. M. .; Cui, N.; McKinley, A. An XPS Study of the Surface Modification of Natural MoS_2 Following Treatment in an RF-Oxygen Plasma. *Appl. Surf. Sci.* **1998**, *134*, 11–21.

(84) Fleischauer, P. D.; Lince, J. R.; Bertrand, P. A.; Bauer, R. Electronic Structure and Lubrication Properties of Molybdenum Disulfide: A Qualitative Molecular Orbital Approach. *Langmuir* **1989**, *5*, 1009–1015.

(85) Lu, Z. H. Ultraviolet-Ozone Oxidation of GaAs(100) and InP(100). *J. Vac. Sci. Technol. B Microelectron. Nanom. Struct.* **1993**, *11*, 2033.

(86) Zhao, S.; Surwade, S. P.; Li, Z.; Liu, H. Photochemical Oxidation of CVD-Grown Single Layer Graphene. *Nanotechnology* **2012**, *23*, 355703.

(87) Zhou, W.; Zou, X.; Najmaei, S.; Liu, Z.; Shi, Y.; Kong, J.; Lou, J.; Ajayan, P. M.; Yakobson, B. I.; Idrobo, J.-C. Intrinsic Structural Defects in Monolayer Molybdenum Disulfide. *Nano Lett.* **2013**, *13*, 2615–2622.

(88) Günther, C.; Karl, N.; Pflaum, J.; Strohmaier, R.; Gompf, B.; Eisenmenger, W.; Müller, M.; Müllen, K. LEED, STM, and TDS Studies of Ordered Thin Films of the Rhombus-Shaped Polycondensed Aromatic Hydrocarbon $C_{54}H_{22}$, on MoS_2, GeS, and Graphite. *Langmuir* **2005**, *21*, 656–665.

(89) Cui, N.-Y.; Brown, N. M. .; McKinley, A. An AFM Study of a Laboratory-Grown Single-Crystal MoS2 Surface Following Radio-Frequency Oxygen Plasma Treatment. *Appl. Surf. Sci.* **2000**, *158*, 104–111.

(90) Abrams, B. L.; Wilcoxon, J. P. Nanosize Semiconductors for Photooxidation. *Crit. Rev. Solid State Mater. Sci.* **2005**, *30*, 153–182.

(91) Thurston, T. R.; Wilcoxon, J. P. Photooxidation of Organic Chemicals Catalyzed by Nanoscale MoS_2. *J. Phys. Chem. B* **1999**, *103*, 11–17.

(92) Hinkle, C. L.; Sonnet, A. M.; Vogel, E. M.; McDonnell, S.; Hughes, G. J.; Milojevic, M.; Lee, B.; Aguirre-Tostado, F. S.; Choi, K. J.; Kim, H. C.; *et al.* GaAs Interfacial Self-Cleaning by Atomic Layer Deposition. *Appl. Phys. Lett.* **2008**, *92*, 71901.

(93) Rafí, J. M.; Zabala, M.; Beldarrain, O.; Campabadal, F. Deposition Temperature and Thermal Annealing Effects on the Electrical Characteristics of Atomic Layer Deposited Al_2O_3 Films on Silicon. *J. Electrochem. Soc.* **2011**, *158*, G108.

(94) Park, S.; Kim, S. Y.; Choi, Y.; Kim, M.; Shin, H.; Kim, J.; Choi, W. Interface Properties of Atomic-Layer-Deposited Al_2O_3 Thin Films on Ultraviolet/Ozone-Treated Multilayer MoS_2 Crystals. *ACS Appl. Mater. Interfaces* **2016**, *8*, 11189–11193.

(95) Podzorov, V.; Gershenson, M. E.; Kloc, C.; Zeis, R.; Bucher, E. High-Mobility Field-Effect Transistors Based on Transition Metal Dichalcogenides. *Appl. Phys. Lett.* **2004**, *84*, 3301.

(96) Das, S.; Prakash, A.; Salazar, R.; Appenzeller, J. Toward Low-Power Electronics: Tunneling Phenomena in Transition Metal Dichalcogenides. *ACS Nano* **2014**, *8*, 1681–1689.

(97) Thurston, T. R.; Wilcoxon, J. P. Photooxidation of Organic Chemicals Catalyzed by Nanoscale MoS_2. *J. Phys. Chem. B* **1999**, *103*, 11–17.

(98) Chamlagain, B.; Li, Q.; Ghimire, N. J.; Chuang, H.; Perera, M. M.; Tu, H.; Xu, Y.; Pan, M.; Xaio, D.; Yan, J.; *et al.* Mobility Improvement and Temperature Dependence in $MoSe_2$ Field-Effect Transistors on Parylene-C Substrate. *ACS Nano* **2014**, *8*, 5079–5088.

(99) Fang, H.; Chuang, S.; Chang, T. C.; Takei, K.; Takahashi, T.; Javey, A. High-Performance Single Layered WSe_2 P-FETs with Chemically Doped Contacts. *Nano Lett.* **2012**, *12*, 3788–3792.

(100) Cheng, L.; Qin, X.; Lucero, A. T.; Azcatl, A.; Huang, J.; Wallace, R. M.; Cho, K.; Kim, J. Atomic Layer Deposition of a High- K Dielectric on MoS_2 Using Trimethylaluminum and Ozone. *ACS Appl. Mater. Interfaces* **2014**, *6*, 11834–11838.

(101) Zou, X.; Wang, J.; Chiu, C.-H.; Wu, Y.; Xiao, X.; Jiang, C.; Wu, W.-W.; Mai, L.; Chen, T.; Li, J.; *et al.* Interface Engineering for High-Performance Top-Gated MoS_2 Field-Effect Transistors. *Adv. Mater.* **2014**, *26*, 6255–6261.

(102) Park, J. H.; Fathipour, S.; Kwak, I.; Sardashti, K.; Ahles, C. F.; Wolf, S. F.; Edmonds, M.; Vishwanath, S.; Xing, H. G.; Fullerton-Shirey, S. K.; *et al.* Atomic Layer Deposition of Al_2O_3 on WSe_2 Functionalized by Titanyl Phthalocyanine. *ACS Nano* **2016**, *10*, 6888–

6896.

(103) Kohn, W.; Sham, L. J. Self-Consistent Equations Including Exchange and Correlation Effects. *Phys. Rev.* **1965**, *140*, A1133–A1138.

(104) Blöchl, P. E. Projector Augmented-Wave Method. *Phys. Rev. B* **1994**, *50*, 17953–17979.

(105) Kresse, G. From Ultrasoft Pseudopotentials to the Projector Augmented-Wave Method. *Phys. Rev. B* **1999**, *59*, 1758–1775.

(106) Kresse, G.; Hafner, J. Ab Initio Molecular Dynamics for Liquid Metals. *Phys. Rev. B* **1993**, *47*, 558–561.

(107) Qin, P.; Fang, G.; Ke, W.; Cheng, F.; Zheng, Q.; Wan, J.; Lei, H.; Zhao, X. In Situ Growth of Double-Layer MoO_3/MoS_2 Film from MoS_2 for Hole-Transport Layers in Organic Solar Cell. *J. Mater. Chem. A* **2014**, *2*, 2742.

(108) Brewer, L.; Lamoreaux, R. H. The Mo-O System (Molybdenum-Oxygen). *Bull. Alloy Phase Diagrams* **1980**, *1*, 85–89.

(109) Smith, R. L.; Rohrer, G. S. Scanning Probe Microscopy of Cleaved Molybdates: α-MoO_3(010), $Mo_{18}O_{52}$(100), Mo_8O_{23}(010), and η-Mo_4O_{11}(100). *J. Solid State Chem.* **1996**, *124*, 104–115.

(110) Benoist, L.; Gonbeau, D.; Pfister-Guillouzo, G.; Schmidt, E.; Meunier, G.; Levasseur, A. X-Ray Photoelectron Spectroscopy Characterization of Amorphous Molybdenum Oxysulfide Thin Films. *Thin Solid Films* **1995**, *258*, 110–114.

(111) Bichsel, R.; Lévy, F.; Mathieu, H. J. Study of R.f. Magnetron-Sputtered $MoSe_2$ Films by Electron Spectroscopy for Chemical Analysis. *Thin Solid Films* **1985**, *131*, 87–94.

(112) Bernède, J. . About the Preferential Sputtering of Chalcogen from Transition Metal Dichalcogenide Compounds and the Determination of Compound Stoichiometry from XPS Peak Positions. *Appl. Surf. Sci.* **2001**, *171*, 15–20.

(113) Simchi, H.; McCandless, B. E.; Meng, T.; Boyle, J. H.; Shafarman, W. N. Characterization of Reactively Sputtered Molybdenum Oxide Films for Solar Cell Application. *J. Appl. Phys.* **2013**, *114*, 13503.

(114) Jaegermann, W.; Schmeisser, D. Reactivity of Layer Type Transition Metal Chalcogenides towards Oxidation. *Surf. Sci.* **1986**, *165*, 143–160.

(115) Aguirre-Tostado, F. S.; Layton, D.; Herrera-Gomez, A.; Wallace, R. M.; Zhu, J.; Larrieu, G.; Maldonado, E.; Kirk, W. P.; Tao, M. X-Ray Photoelectron Spectroscopy Study of the Oxidation of Se Passivated Si(001). *J. Appl. Phys.* **2007**, *102*.

(116) Greiner, M. T.; Chai, L.; Helander, M. G.; Tang, W.-M.; Lu, Z.-H. Metal/Metal-Oxide Interfaces: How Metal Contacts Affect the Work Function and Band Structure of MoO_3. *Adv. Funct. Mater.* **2013**, *23*, 215–226.

(117) Chang, C.-H.; Chiou, Y.-K.; Chang, Y.-C.; Lee, K.-Y.; Lin, T.-D.; Wu, T.-B.; Hong, M.; Kwo, J. Interfacial Self-Cleaning in Atomic Layer Deposition of HfO_2 Gate Dielectric on $In_{0.15}Ga_{0.85}As$. *Appl. Phys. Lett.* **2006**, *89*, 242911.

(118) Humphrey, G. L. Heats of Formation of Hafnium Oxide and Hafnium Nitride. *J. Am. Chem. Soc.* **1953**, *75*, 2806–2807.

(119) Bard, A. J., Parsons, R., Jordan, J. *Standard Potentials in Aqueous Solution*; CRC Press: Boca Raton, FL, 1985.

(120) Lavik, M. T.; Medved, T. M.; Moore, G. D. Oxidation Characteristics of MoS_2 and Other Solid Lubricants. *A S L E Trans.* **1968**, *11*, 44–55.

(121) Luo, Y. R. *Comprehensive Handbook of Chemical Bond Energies*; CRC Press: Boca Raton, FL, 2007.

(122) Li, Z.; Fang, Z.; Kelley, M. S.; Kay, B. D.; Rousseau, R.; Dohnalek, Z.; Dixon, D. a. Ethanol Conversion on Cyclic $(MO_3)_3$ (M = Mo, W) Clusters. *J. Phys. Chem. C* **2014**, *118*, 4869–4877.

(123) Klein, A.; Dolatzoglou, P.; Lux-Steiner, M.; Bucher, E. Influence of Material Synthesis and Doping on the Transport Properties of WSe_2 Single Crystals Grown by Selenium Transport. *Sol. Energy Mater. Sol. Cells* **1997**, *46*, 175–186.

(124) Tenne, R.; Eherman, K.; Mahalu, D.; Peisach, M.; Kautek, W.; Wold, A.; Matson, R.; Waldeck, D. H. The WSe_2/Tungsten-Oxide Interface: Structure and Photoluminescence. *Berichte der Bunsengesellschaft für Phys. Chemie* **1993**, *97*, 702–708.

(125) Böhmisch, M.; Burmeister, F.; Boneberg, J.; Leiderer, P. Nanostructuring on WSe_2 with the Atomic Force Microscope by a Potential Controlled Electrochemical Reaction. *Appl. Phys. Lett.* **1996**, *69*, 1882.

(126) Jaeckel, B.; Gassenbauer, Y.; Jaegermann, W.; Tomm, Y. AFM Tip Induced Formation of Nanometer Scale Structures on WSe_2 under Defined Conditions. *Surf. Sci.* **2005**, *597*, 65–79.

(127) Boneberg, J.; Lohrmann, M.; Böhmisch, M.; Burmeister, F.; Lux-Steiner, M.; Leiderer, P. Electrical Field Induced Growth of Triangular Nanometer Structures on WSe_2. *Zeitschrift für Phys. B Condens. Matter* **1995**, *99*, 567–570.

(128) Azcatl, A.; KC, S.; Peng, X.; Lu, N.; McDonnell, S.; Qin, X.; de Dios, F.; Addou, R.;

Kim, J.; Kim, M. J.; *et al.* HfO_2 on UV–O_3 Exposed Transition Metal Dichalcogenides: Interfacial Reactions Study. *2D Mater.* **2015**, *2*, 14004.

(129) Jandhyala, S.; Mordi, G.; Lee, B.; Lee, G.; Floresca, C.; Cha, P.-R.; Ahn, J.; Wallace, R. M.; Chabal, Y. J.; Kim, M. J.; *et al.* Atomic Layer Deposition of Dielectrics on Graphene Using Reversibly Physisorbed Ozone. *ACS Nano* **2012**, *6*, 2722–2730.

(130) Warren, A.; Nylund, A.; Olefjord, I. Oxidation of Tungsten and Tungsten Carbide in Dry and Humid Atmospheres. *Int. J. Refract. Met. Hard Mater.* **1996**, *14*, 345–353.

(131) Kwon, J.; Dai, M.; Halls, M. D.; Chabal, Y. J. Detection of a Formate Surface Intermediate in the Atomic Layer Deposition of High-k Dielectrics Using Ozone. *Chem. Mater.* **2008**, *20*, 3248–3250.

(132) GRUNERT, W. Reduction Behavior and Metathesis Activity of WO_3/Al_2O_3 Catalysts I. An XPS Investigation of WO_3/Al_2O_3 Catalysts. *J. Catal.* **1987**, *107*, 522–534.

(133) Salvati, L.; Makovsky, L. E.; Stencel, J. M.; Brown, F. R.; Hercules, D. M. Surface Spectroscopic Study of Tungsten-Alumina Catalysts Using X-Ray Photoelectron, Ion Scattering, and Raman Spectroscopies. *J. Phys. Chem.* **1981**, *85*, 3700–3707.

(134) Liu, X.; Ramanathan, S.; Longdergan, A.; Srivastava, A.; Lee, E.; Seidel, T. E.; Barton, J. T.; Pang, D.; Gordon, R. G. ALD of Hafnium Oxide Thin Films from Tetrakis(ethylmethylamino)hafnium and Ozone. *J. Electrochem. Soc.* **2005**, *152*, G213.

(135) Vitchev, R. G.; Pireaux, J. J.; Conard, T.; Bender, H.; Wolstenholme, J.; Defranoux, C. X-Ray Photoelectron Spectroscopy Characterisation of High-k Dielectric Al_2O_3 and HfO_2 Layers Deposited on SiO_2/Si Surface. *Appl. Surf. Sci.* **2004**, *235*, 21–25.

(136) Kraut, E. A.; Grant, R. W.; Waldrop, J. R.; Kowalczyk, S. P. Precise Determination of the Valence-Band Edge in X-Ray Photoemission Spectra: Application to Measurement of Semiconductor Interface Potentials. *Phys. Rev. Lett.* **1980**, *44*, 1620–1623.

(137) Miyazaki, S. Characterization of High-k Gate Dielectric/silicon Interfaces. *Appl. Surf. Sci.* **2002**, *190*, 66–74.

(138) Ohta, A.; Murakami, H.; Higashi, S.; Miyazaki, S. Determination of Energy Band Alignment in Ultrathin Hf-Based Oxide/Pt System. *J. Phys. Conf. Ser.* **2013**, *417*, 12012.

(139) Yeh, P.-C.; Jin, W.; Zaki, N.; Zhang, D.; Liou, J. T.; Sadowski, J. T.; Al-Mahboob, A.; Dadap, J. I.; Herman, I. P.; Sutter, P.; *et al.* Layer-Dependent Electronic Structure of an Atomically Heavy Two-Dimensional Dichalcogenide. *Phys. Rev. B* **2015**, *91*, 41407.

(140) Liu, X.; He, J.; Liu, Q.; Tang, D.; Jia, F.; Wen, J.; Lu, Y.; Yu, W.; Zhu, D.; Liu, W.; *et al.* Band Alignment of HfO_2/multilayer MoS_2 Interface Determined by X-Ray Photoelectron

Spectroscopy: Effect of CHF3 Treatment. *Appl. Phys. Lett.* **2015**, *107*, 101601.

(141) Chen, M.; Nam, H.; Wi, S.; Ji, L.; Ren, X.; Bian, L.; Lu, S.; Liang, X. Stable Few-Layer MoS_2 Rectifying Diodes Formed by Plasma-Assisted Doping. *Appl. Phys. Lett.* **2013**, *103*, 142110.

(142) Nipane, A.; Karmakar, D.; Kaushik, N.; Karande, S.; Lodha, S. Few-Layer MoS_2 p-Type Devices Enabled by Selective Doping Using Low Energy Phosphorus Implantation. *ACS Nano* **2016**, *10*, 2128–2137.

(143) Modic, A.; Sharma, Y.; Xu, Y.; Liu, G.; Ahyi, A.; Williams, J. R.; Feldman, L. C.; Dhar, S. Nitrogen Plasma Processing of SiO_2/4H-SiC Interfaces. *J. Electron. Mater.* **2014**, *43*, 857–862.

(144) Talbi, A.; Benamara, Z.; Akkal, B.; Gruzza, B.; Bideux, L.; Robert, C.; Varenne, C.; Chami, N. Nitridation of InP(100) Substrates Studied by XPS Spectroscopy and Electrical Analysis. *Mater. Sci. Eng. A* **2006**, *437*, 254–258.

(145) Gicquel, A.; Laidani, N.; Saillard, P. Plasma and Nitrides: Application to the Nitriding of Titanium. *Pure Appl. Chem.* **1990**, *62*, 1743–1750.

(146) Patel, P.; Nadesalingam, M.; Wallace, R. M.; Buchanan, D. A. Physical and Optoelectronic Characterization of Reactively Sputtered Molybdenum-Silicon-Nitride Alloy Metal Gate Electrodes. *J. Appl. Phys.* **2009**, *105*, 24517.

(147) Akada, K.; Terasawa, T.; Imamura, G.; Obata, S.; Saiki, K. Control of Work Function of Graphene by Plasma Assisted Nitrogen Doping. *Appl. Phys. Lett.* **2014**, *104*, 131602.

(148) Dolui, K.; Rungger, I.; Das Pemmaraju, C.; Sanvito, S. Possible Doping Strategies for MoS_2 Monolayers: An *Ab Initio* Study. *Phys. Rev. B* **2013**, *88*, 75420.

(149) Yue, Q.; Chang, S.; Qin, S.; Li, J. Functionalization of Monolayer MoS_2 by Substitutional Doping: A First-Principles Study. *Phys. Lett. A* **2013**, *377*, 1362–1367.

(150) Hartel, P.; Rose, H.; Dinges, C. Conditions and Reasons for Incoherent Imaging in STEM. *Ultramicroscopy* **1996**, *63*, 93–114.

(151) Perdew, J. P.; Burke, K.; Ernzerhof, M. Generalized Gradient Approximation Made Simple. *Phys. Rev. Lett.* **1996**, *77*, 3865–3868.

(152) Monkhorst, H. J.; Pack, J. D. Special Points for Brillouin-Zone Integrations. *Phys. Rev. B* **1976**, *13*, 5188–5192.

(153) Tabbal, M.; Mérel, P.; Moisa, S.; Chaker, M.; Gat, E.; Ricard, A.; Moisan, M.; Gujrathi, S. XPS and FTIR Analysis of Nitrogen Incorporation in CN_x Thin Films. *Surf. Coatings Technol.* **1998**, *98*, 1092–1096.

(154) Bécue, T.; Manoli, J.-M.; Potvin, C.; Djéga-Mariadassou, G. Preparation, Characterization, and Catalytic Behavior of Molybdenum Oxynitrides Supported on EMT Zeolite (NaEMT and HEMT) Catalysts. *J. Catal.* **1997**, *170*, 123–131.

(155) Wei, Z. B. Z.; Grange, P.; Delmon, B. XPS and XRD Studies of Fresh and Sulfided Mo_2N. *Appl. Surf. Sci.* **1998**, *135*, 107–114.

(156) Sharma, J.; Downs, D. S.; Iqbal, Z.; Owens, F. J. X-Ray Photoelectron Spectroscopy of S_2N_2 and the Solid State Polymerization of S_2N_2 to Metallic $(SN)_x$. *J. Chem. Phys.* **1977**, *67*, 3045.

(157) Qin, X.; Dong, H.; Brennan, B.; Azacatl, A.; Kim, J.; Wallace, R. M. Impact of N_2 and Forming Gas Plasma Exposure on the Growth and Interfacial Characteristics of Al_2O_3 on AlGaN. *Appl. Phys. Lett.* **2013**, *103*, 221604.

(158) Bermudez, V. M. Study of Oxygen Chemisorption on the GaN(0001)-(1×1) Surface. *J. Appl. Phys.* **1996**, *80*, 1190–1200.

(159) Moulder, J. F., Stickle, W. F., Sobol, P. E. & Bomben, K. D. *Handbook of X-Ray Photoelectron Spectroscopy*; Physical Electronics, Inc.: Minnesota, 1995.

(160) Qin, S.; Lei, W.; Liu, D.; Chen, Y. In-Situ and Tunable Nitrogen-Doping of MoS_2 Nanosheets. *Sci. Rep.* **2014**, *4*, 7582.

(161) Jauberteau, I.; Bessaudou, A.; Mayet, R.; Cornette, J.; Jauberteau, J.; Carles, P.; Merle-Méjean, T. Molybdenum Nitride Films: Crystal Structures, Synthesis, Mechanical, Electrical and Some Other Properties. *Coatings* **2015**, *5*, 656–687.

(162) Kanoun, M. B.; Goumri-Said, S.; Jaouen, M. Structure and Mechanical Stability of Molybdenum Nitrides: A First-Principles Study. *Phys. Rev. B* **2007**, *76*, 134109.

(163) Ma, Q.; Odenthal, P. M.; Mann, J.; Le, D.; Wang, C. S.; Zhu, Y.; Chen, T.; Sun, D.; Yamaguchi, K.; Tran, T.; *et al.* Controlled Argon Beam-Induced Desulfurization of Monolayer Molybdenum Disulfide. *J. Phys. Condens. Matter* **2013**, *25*, 252201.

(164) Hunger, R.; Fritsche, R.; Jaeckel, B.; Jaegermann, W.; Webb, L. J.; Lewis, N. S. Chemical and Electronic Characterization of Methyl-Terminated Si(111) Surfaces by High-Resolution Synchrotron Photoelectron Spectroscopy. *Phys. Rev. B* **2005**, *72*, 45317.

(165) Estrada, D.; Dutta, S.; Liao, A.; Pop, E. Reduction of Hysteresis for Carbon Nanotube Mobility Measurements Using Pulsed Characterization. *Nanotechnology* **2010**, *21*, 85702.

(166) Zhang, F.; Appenzeller, J. Tunability of Short-Channel Effects in MoS_2 Field-Effect Devices. *Nano Lett.* **2015**, *15*, 301–306.

(167) Gong, C.; Colombo, L.; Wallace, R. M.; Cho, K. The Unusual Mechanism of Partial

Fermi Level Pinning at Metal–MoS_2 Interfaces. *Nano Lett.* **2014**, *14*, 1714–1720.

(168) Huang, Y.; Wu, J.; Xu, X.; Ho, Y.; Ni, G.; Zou, Q.; Koon, G. K. W.; Zhao, W.; Castro Neto, a. H.; Eda, G.; *et al.* An Innovative Way of Etching MoS_2: Characterization and Mechanistic Investigation. *Nano Res.* **2013**, *6*, 200–207.

(169) Conley, H. J.; Wang, B.; Ziegler, J. I.; Haglund, R. F.; Pantelides, S. T.; Bolotin, K. I. Bandgap Engineering of Strained Monolayer and Bilayer MoS_2. *Nano Lett.* **2013**, *13*, 3626–3630.

(170) Hui, Y. Y.; Liu, X.; Jie, W.; Chan, N. Y.; Hao, J.; Hsu, Y.-T.; Li, L.-J.; Guo, W.; Lau, S. P. Exceptional Tunability of Band Energy in a Compressively Strained Trilayer MoS_2 Sheet. *ACS Nano* **2013**, *7*, 7126–7131.

(171) Tillack, B.; Zaumseil, P.; Morgenstern, G.; Krüger, D.; Dietrich, B.; Ritter, G. Strain Compensation in Ternary $Si_{1-X-y}Ge_xB_y$ Films. *J. Cryst. Growth* **1995**, *157*, 181–184.

(172) Canham, L. T.; Dyball, M. R.; Barraclough, K. G. A Study of Carbon-Implanted Silicon for Light-Emitting Diode Fabrication. *Mater. Sci. Eng. B* **1989**, *4*, 95–99.

(173) Chakraborty, B.; Bera, A.; Muthu, D. V. S.; Bhowmick, S.; Waghmare, U. V.; Sood, a. K. Symmetry-Dependent Phonon Renormalization in Monolayer MoS_2 Transistor. *Phys. Rev. B* **2012**, *85*, 161403.

(174) Nayak, A. P.; Bhattacharyya, S.; Zhu, J.; Liu, J.; Wu, X.; Pandey, T.; Jin, C.; Singh, A. K.; Akinwande, D.; Lin, J.-F. Pressure-Induced Semiconducting to Metallic Transition in Multilayered Molybdenum Disulphide. *Nat. Commun.* **2014**, *5*, 1–9.

(175) Manzeli, S.; Allain, A.; Ghadimi, A.; Kis, A. Piezoresistivity and Strain-Induced Band Gap Tuning in Atomically Thin MoS_2. *Nano Lett.* **2015**, *15*, 5330–5335.

(176) Bertolazzi, S.; Brivio, J.; Kis, A. Stretching and Breaking of Ultrathin MoS_2. *ACS Nano* **2011**, *5*, 9703–9709.

(177) Kou, L.; Du, A.; Chen, C.; Frauenheim, T. Strain Engineering of Selective Chemical Adsorption on Monolayer MoS_2. *Nanoscale* **2014**, 5156–5161.

(178) Shen, T.; Penumatcha, A. V.; Appenzeller, J. Strain Engineering for Transition Metal Dichalcogenides Based Field Effect Transistors. *ACS Nano* **2016**, *10*, 4712–4718.

VITA

Angelica Azcatl Zacatzi was born on November 2nd, 1988 in San Andres Cholula, Puebla, Mexico. In 2006, she was awarded with a full-tuition scholarship to pursue her undergraduate studies at The University of the Americas, Puebla, receiving the bachelor's degree in Nanotechnology in 2011. In 2012, she enrolled in the Ph.D. program in Materials Science and Engineering, at The University of Texas at Dallas. In the same year, she was recipient of the CONACYT-Mexico scholarship to pursue her doctorate studies. Her research is focused on the application of surface science and materials characterization for two-dimensional electronic device applications. During the doctorate program, she participated as representative in the MRS-UTD Student Chapter and in the DFW-Metroplex AVS Student Chapter. She is expected to obtain her doctoral degree in December 2016.

List of publications from the graduate program at UT Dallas:

(1) Azcatl, A.; Qin, X.; Prakash, A.; Zhang, C.; Cheng, L.; Wang, Q.; Lu, N.; Kim, M. J.; Kim, J.; Cho, K.; *et al.* Covalent Nitrogen Doping and Compressive Strain in MoS_2 by Remote N_2 Plasma Exposure. *Nano Lett.* **2016**, *16*, 5437–5443.

(2) Bjaalie, L.; Azcatl, A.; McDonnell, S.; Freeze, C. R.; Stemmer, S.; Wallace, R. M.; Van de Walle, C. G. Band Alignments between $SmTiO_3$, $GdTiO_3$, and $SrTiO_3$. *J. Vac. Sci. Technol. A Vacuum, Surfaces, Film.* **2016**, *34*, 61102.

(3) Bullock, J.; Kiriya, D.; Grant, N.; Azcatl, A.; Hettick, M.; Kho, T.; Phang, P.; Sio, H. C.; Yan, D.; Macdonald, D.; *et al.* Superacid Passivation of Crystalline Silicon Surfaces. *ACS Appl. Mater. Interfaces* **2016**, *8*, 24205–24211.

(4) Cheng, L.; Jandhyala, S.; Mordi, G.; Lucero, A. T.; Huang, J.; Azcatl, A.; Addou, R.; Wallace, R. M.; Colombo, L.; Kim, J. Partially Fluorinated Graphene: Structural and Electrical Characterization. *ACS Appl. Mater. Interfaces* **2016**, *8*, 5002–5008.

(5) Vishwanath, S.; Liu, X.; Rouvimov, S.; Basile, L.; Lu, N.; Azcatl, A.; Magno, K.; Wallace, R. M.; Kim, M.; Idrobo, J.-C.; *et al.* Controllable Growth of Layered Selenide

and Telluride Heterostructures and Superlattices Using Molecular Beam Epitaxy. *J. Mater. Res.* **2016**, 1–11.

(6) Zhao, P.; Azcatl, A**.;** Bolshakov-Barrett, P.; Wallace, R. M.; Young, C. D.; Hurley, P. K. Top-Gated MoS_2 Capacitors and Transistors with High-K Dielectrics for Interface Study. In *2016 International Conference on Microelectronic Test Structures (ICMTS)*; IEEE, 2016–May, 172–175.

(7) Zhu, H.; Qin, X.; Cheng, L.; Azcatl, A.; Kim, J.; Wallace, R. M. Remote Plasma Oxidation and Atomic Layer Etching of MoS_2. *ACS Appl. Mater. Interfaces* **2016**, *8*, 19119–19126.

(8) Addou, R.; McDonnell, S.; Barrera, D.; Guo, Z.; Azcatl, A.; Wang, J.; Zhu, H.; Hinkle, C. L.; Quevedo-Lopez, M.; Alshareef, H. N.; *et al.* Impurities and Electronic Property Variations of Natural MoS_2 Crystal Surfaces. *ACS Nano* **2015**, *9*, 9124–9133.

(9) Amani, M.; Lien, D.-H.; Kiriya, D.; Xiao, J.; Azcatl, A.; Noh, J.; Madhvapathy, S. R.; Addou, R.; Kc, S.; Dubey, M.; *et al.* Near-Unity Photoluminescence Quantum Yield in MoS_2. *Science*, **2015**, *350*, 1065–1068.

(10) Azcatl, A.; KC, S.; Peng, X.; Lu, N.; McDonnell, S.; Qin, X.; de Dios, F.; Addou, R.; Kim, J.; Kim, M. J.; *et al.* HfO_2 on UV–O_3 Exposed Transition Metal Dichalcogenides: Interfacial Reactions Study. *2D Mater.* **2015**, *2*, 14004.

(11) Dahal, A.; Addou, R.; Azcatl, A.; Coy-Diaz, H.; Lu, N.; Peng, X.; De Dios, F.; Kim, J.; Kim, M. J.; Wallace, R. M.; *et al.* Seeding Atomic Layer Deposition of Alumina on Graphene with Yttria. *ACS Appl. Mater. Interfaces* **2015**, *7*, 2082–2087.

(12) Eichfeld, S. M.; Hossain, L.; Lin, Y.; Piasecki, A. F.; Kupp, B.; Birdwell, A. G.; Burke, R. A.; Lu, N.; Peng, X.; Li, J.; *et al.* Highly Scalable, Atomically Thin WSe_2 Grown via Metal–Organic Chemical Vapor Deposition. *ACS Nano* **2015**, *9*, 2080–2087.

(13) Vishwanath, S.; Liu, X.; Rouvimov, S.; Mende, P. C.; Azcatl, A.; McDonnell, S.; Wallace, R. M.; Feenstra, R. M.; Furdyna, J. K.; Jena, D.; *et al.* Comprehensive Structural and Optical Characterization of MBE Grown $MoSe_2$ on Graphite, CaF_2 and Graphene. *2D Mater.* **2015**, *2*, 24007.

(14) Yue, R. Y.; Barton, A. T.; Zhu, H.; Azcatl, A.; Pena, L. F.; Wang, J.; Peng, X.; Lu, N.; Cheng, L. X.; Addou, R.; *et al.* $HfSe_2$ Thin Films: 2D Transition Metal Dichalcogenides Grown by Molecular Beam Epitaxy. *ACS Nano* **2015**, *9*, 474–480.

(15) Zhang, K.; Feng, S.; Wang, J.; Azcatl, A.; Lu, N.; Addou, R.; Wang, N.; Zhou, C.; Lerach, J.; Bojan, V.; *et al.* Manganese Doping of Monolayer MoS_2 : The Substrate Is Critical. *Nano Lett.* **2015**, *15*, 6586–6591.

(16) Zhu, H.; McDonnell, S.; Qin, X.; Azcatl, A.; Cheng, L.; Addou, R.; Kim, J.; Ye, P. D.; Wallace, R. M. Al_2O_3 on Black Phosphorus by Atomic Layer Deposition: An in Situ Interface Study. *ACS Appl. Mater. Interfaces* **2015**, *7*, 13038–13043.

(17) Qin, X.; Cheng, L.; McDonnell, S.; Azcatl, A.; Zhu, H.; Kim, J.; Wallace, R. M. A Comparative Study of Atomic Layer Deposition of Al_2O_3 and HfO_2 on AlGaN/GaN. *J. Mater. Sci. Mater. Electron.* **2015**, 1–6.

(18) Azcatl, A**.;** McDonnell, S.; K. C., S.; Peng, X.; Dong, H.; Qin, X.; Addou, R.; Mordi, G. I.; Lu, N.; Kim, J.; *et al.* MoS_2 Functionalization for Ultra-Thin Atomic Layer Deposited Dielectrics. *Appl. Phys. Lett.* **2014**, *104*, 111601.

(19) Battaglia, C.; Yin, X.; Zheng, M.; Sharp, I. D.; Chen, T.; McDonnell, S.; Azcatl, A.; Carraro, C.; Ma, B.; Maboudian, R.; *et al*. Hole Selective MoO_x Contact for Silicon Solar Cells. Nano Lett. 2014, 14, 967–971.

(20) Cheng, L.; Qin, X.; Lucero, A. T.; Azcatl, A.; Huang, J.; Wallace, R. M.; Cho, K.; Kim, J. Atomic Layer Deposition of a High- K Dielectric on MoS_2 Using Trimethylaluminum and Ozone. *ACS Appl. Mater. Interfaces* **2014**, *6*, 11834–11838.

(21) Chuang, S.; Battaglia, C.; Azcatl, A**.;** McDonnell, S.; Kang, J. S.; Yin, X.; Tosun, M.; Kapadia, R.; Fang, H.; Wallace, R. M.; *et al.* MoS_2 P-Type Transistors and Diodes Enabled by High Work Function MoO_xContacts. *Nano Lett.* **2014**, *14*, 1337–1342.

(22) Zhao, P.; Kiriya, D.; Azcatl, A.; Zhang, C.; Tosun, M.; Liu, Y.; Hettick, M.; Kang, J. S.; McDonnell, S.; KC, S.; *et al.* Air Stable P-Doping of WSe_2 by Covalent Functionalization. *ACS Nano* **2014**, *8*, 10808–10814.

(23) Gong, C.; McDonnell, S.; Qin, X.; Azcatl, A**.;** Dong, H.; Chabal, Y. J.; Cho, K.; Wallace, R. M. Realistic Metal–Graphene Contact Structures. *ACS Nano* **2014**, *8*, 642–649.

(24) McDonnell, S.; Azcatl, A.; Mordi, G.; Floresca, C.; Pirkle, a.; Colombo, L.; Kim, J.; Kim, M.; Wallace, R. M. Scaling of HfO_2 Dielectric on CVD Graphene. *Appl. Surf. Sci.* **2014**, *294*, 95–99.

(25) McDonnell, S.; Azcatl, A.; Addou, R.; Gong, C.; Battaglia, C.; Chuang, S.; Cho, K.; Javey, A.; Wallace, R. M. Hole Contacts on Transition Metal Dichalcogenides: Interface Chemistry and Band Alignments. *ACS Nano* **2014**, *8*, 6265–6272.

(26) Qin, X.; Lucero, A.; Azcatl, A.; Kim, J.; Wallace, R. M. In Situ X-Ray Photoelectron Spectroscopy and Capacitance Voltage Characterization of Plasma Treatments for Al_2O_3/AlGaN/GaN Stacks. *Appl. Phys. Lett.* **2014**, *105*, 11602.

(27) Dong, H.; KC, S.; Azcatl, A.; Cabrera, W.; Qin, X.; Brennan, B.; Zhernokletov, D.; Cho, K.; Wallace, R. M. In Situ Study of E-Beam Al and Hf Metal Deposition on Native Oxide InP (100). *J. Appl. Phys.* **2013**, *114*, 1–7.

(28) McDonnell, S.; Brennan, B.; Azcatl, A.; Lu, N.; Dong, H.; Buie, C.; Kim, J.; Hinkle, C. L.; Kim, M. J.; Wallace, R. M. HfO_2 on MoS_2 by Atomic Layer Deposition: Adsorption Mechanisms and Thickness Scalability. *ACS Nano* **2013**, *7*, 10354–10361.